



Water Dynamics in Biological Systems investigated using Neutron Scattering Techniques

Irina Piazza

► To cite this version:

Irina Piazza. Water Dynamics in Biological Systems investigated using Neutron Scattering Techniques. Biophysics. Institut Laue-Langevin, Grenoble, France; Università degli Studi di Palermo, 2018. English. NNT: . tel-01933949

HAL Id: tel-01933949

<https://theses.hal.science/tel-01933949>

Submitted on 4 Mar 2019

HAL is a multi-disciplinary open access archive for the deposit and dissemination of scientific research documents, whether they are published or not. The documents may come from teaching and research institutions in France or abroad, or from public or private research centers.

L'archive ouverte pluridisciplinaire **HAL**, est destinée au dépôt et à la diffusion de documents scientifiques de niveau recherche, publiés ou non, émanant des établissements d'enseignement et de recherche français ou étrangers, des laboratoires publics ou privés.



UNIVERSITÀ DEGLI STUDI DI PALERMO

Dottorato di Ricerca in Medicina Molecolare e Biotecnologie

Curriculum in Biofisica e Bioimaging

Dipartimento di Fisica e Chimica di Palermo (DiFC)

Fisica Applicata

Water Dynamics in Biological Systems investigated using Neutron Scattering Techniques

IL DOTTORE
Irina Piazza

IL COORDINATORE
Ch.mo Prof. Calogero Caruso

IL TUTOR
Ch.mo Prof. Antonio Cupane

CO TUTOR
Ch.ma Dr.ssa Francesca Natali

Examination Board:

President Prof. Annibale Alessandro Puca
Prof. Ciriaco Carru
Prof. Giuseppina Candore

Dissertation day:

march 28th 2018

PhD project carried out at the Institut Laue-Langevin (ILL),
Grenoble
between January 5th 2015 and January 4th 2018

Acknowledgment

This three years passed at ILL are now finished. This project was a challenge for me. However, each research topic represents a challenge. In fact, we always look to improve our work because there is always a margin for it.

First of all, I would like to thank my scientific supervisor Dr. Francesca Natali. I am grateful to her that since from the first moment she supported, encouraged and guided me and she always was present for discussion on biophysical and mathematical problem connected to the project. I wish to thank her also for allowing me to work on some data from previous experiments.

I wish to thank my academic supervisor Prof. Antonio Cupane, that although he was in Palermo, he was always actively followed the progress of the project. I wish to thank both of my supervisors for giving me the chance to work on this project.

I would like to thank of Prof. Emmanuel Barbier and his team, Dr. Nora Collomb and Dr. Claire Rome for collaborating with us and making the investigation in cellular systems possible. In particular, Dr. Nora Collomb and Dr. Claire Rome were in charged of growing cultures of different kind of cells. I wish to thank them also for allowing us to use cryotome to cut brain tissues at the Neuroscience Institute in Grenoble.

I wish to thank Dr. Miguel A. Gonzalez for introducing me to STRfit tools. Moreover, he helped me to compute the confidence limit investigation. I would like to thank him also for the discussion concerning multi fit problems.

I wish to thank Jacques Ollivier for the hours spent in discussion on Quasi Elastic Neutron Scattering data correction, on theory and instrumental problems.

I wish to thank Giorgio Shirò for the time spent to talk about the project and the precious advices he gave me.

I wish to thank Prof. Jusith Peters, that was my supervisors in my first experience with neutron scattering techniques, for spending time with me on biophysical discussion also during this project.

I wish to thank EMBL for letting us use the fluorescence microscope.

I wish to thank Dr. David Hess (Laboratory Responsibly) and Dr. Sandrine VERDON (Laboratory Assistant) of the ILL Chemistry Laboratories for being always kind and for helping me anytime I needed it.

I wish to thank Dr. Nicolas Martinez for spending time on biophysical and numerical

discussion. I wish to thank Dr. Rosanna Ignazzi for supporting me during the project as colleagues and as a friend.

A special thank is addressed to friends and my relatives which supported me anytime. Last but not least, I would like to thank Dario, that I met at the beginning of my PhD in Grenoble. Thank to him this period was really special, light-hearted and I dedicate this work to him that is now my husband.

Abstract

Living systems can not survive in absence of the water environments which play a fundamental role in living functions. Thus in the scientific community many studies were and are addressed to characterize water and its dynamics properties in biological systems. However, a clear description of water in such systems has been not reached yet. In fact, the investigations performed with different techniques - those based on Nuclear Magnetic Resonance or those based on Neutron Scattering - look at different diffusive motions and interactions water-biomolecules, leading controversial results and hence generating many debates between scientists.

In this thesis we support the idea that two water populations are present in systems such as “phantoms”, cells and tissues, suggesting that this is a general property for biological systems. Such populations are defined as the “fast water” and the “slow water” components which are characterized by dynamics properties similar to bulk water and by slower dynamics, respectively. The samples are investigated mainly using Quasi Elastic Neutron Scattering (QENS) technique which has access to atomic scale and looks at tens of picosecond/nanosecond diffusive processes. A theoretical model previously tested is used to analyze the QENS data. The strategy to analyze the data is improved in the project by using data sets from two energy resolutions - idea existing, but effectively implemented in this work - and introducing the confidence limit investigation to check the true minima. The investigated samples are (1) sucrose in aqueous solution at 10, 20 and 30% of mass fraction percentage at 300 K; (2) *E. coli* samples at 300, 310, and 320 K, yeast and Glioma-9L at 300 K; (3) right and left cerebral hemispheres and right and left cerebellum from bovine brain tissues at 300 K.

Successfully, the results confirm the existence of the two predicted fast and slow water populations in biological systems. Moreover, results from phantom systems and *E. coli* fully validate, as expected, the theoretical approach used. Interestingly, results from Glioma-9L (tumoral cells) show faster diffusion properties for slow water component with respect to the other cells here investigated. On the other hand, results from bovine brain tissues highlight that cerebral hemispheres seem less dynamic with respect to the cerebellum. Moreover, left-right asymmetry is found in slow water component in cerebral hemispheres, while asymmetry in cerebellum is not, if any, evident.

Contents

1	Introduction	1
1.1	Overview of water dynamics in complex systems	1
1.2	Aim of the project	4
1.3	Thesis organization	5
2	Neutron scattering theory	7
2.1	Neutrons	7
2.2	Scattering event	8
2.2.1	AutoCorrelation Function	10
2.3	Scattering law	10
2.4	Neutron scattering signal	16
2.4.1	Quasi Elastic Neutron Scattering	16
2.5	Neutron sources	20
2.5.1	Nuclear reactor	21
2.6	Instruments	23
2.6.1	Time-of-flight spectrometer: IN5	23
2.6.2	Time-of-flight spectrometer: TOFTOF	24
2.6.3	Time-of-flight spectrometer: IN6	25
3	NS experiment and data analysis	28
3.1	Typical NS experiment	28
3.2	NS data treatment	29
3.2.1	QENS data correction	30
3.3	QENS data analysis	32
3.3.1	A theoretical model to analyse QENS data from biological samples .	32
3.3.2	QENS data fitting procedure	34
3.3.3	Confidence limit investigation	36
4	Water in phantom systems	39
4.1	Introduction	39
4.2	Results	40

4.2.1	Pure water	40
4.2.2	Water dynamics in aqueous solution of sucrose	41
4.3	Conclusions	48
5	Water in cellular systems	49
5.1	Introduction	49
5.2	Sample preparation	49
5.3	Results	50
5.4	Conclusions	58
6	Water in bovine brain tissues	60
6.1	Introduction	60
6.2	Brain	60
6.2.1	Cerebrum	61
6.2.2	Cerebellum	61
6.2.3	Lateralization	62
6.3	Sample preparation	62
6.4	Results	64
6.4.1	Results from right side of cerebral hemisphere and cerebellum	64
6.4.2	Left-Right asymmetry in cerebral hemispheres and cerebellum	66
6.5	Conclusions	67
7	Conclusions	72
A	Mathematical and physical tools	75
A.1	Maxwell distribution	75
A.2	Density of state in the scattering event	76
A.3	Pair correlation function	77
A.4	Fourier Transform	77
A.4.1	Summary of relation between $S(\vec{Q}, \omega)$, $I(\vec{Q}, t)$ and $G(\vec{r}, t)$	78
A.5	Convolution theorem	78
A.6	Instrumental resolution in backscattering geometry	79
B	Analysis method tools	80
B.1	Unit conversions	80
B.2	Mpfit versus Coolfit engine	81
C	Elastic neutron scattering technique	82
C.0.1	Elastic Neutron Scattering model	82
C.0.2	Backscattering spectrometer: IN13	82
C.0.3	ENS data correction	85
C.1	Elastic Neutron Scattering experiment on cellular systems	86

Fundamental Physical Constants

Quantity	Symbol	Value	Unit
Neutron mass	m_n	1.67×10^{-27}	kg
Magnetic momentum	μ_n	$-1.91 \mu_B$	J T ⁻¹
Bohr magneton	μ_B	9.2	J T ⁻¹
Plank constant	h	$6.626\,070\,04 \times 10^{-34}$	J s
Reduced Plank constant	\hbar	1.05×10^{-34}	J s
Electron mass	m_e	9.1×10^{-31}	kg
Light velocity	c	3×10^8	m s ⁻¹
Boltzmann constant	k_B	1.38×10^{-23}	m ² kg s ⁻² K ⁻¹
Avogadro constant	N_A	$6.022\,140\,857 \times 10^{23}$	mol ⁻¹

Nomenclature

Symbol	Name
\vec{k}_i	Initial vector
\vec{k}_f	Final vector
E_i	Initial energy
E_f	Final energy
\vec{Q}	Momentum transfer vector
θ	Scattering angle
λ_i	Initial wavelength
$E_f - E_i$	Energy transfer
N	Number of particles
ν	Degree of freedom
A	Stochastic variable
H	Hamiltonian
H_0	Unperturbed Hamiltonian
H'	Weak perturbation
$\rho_n(\vec{r}')$	Nuclear density
b_l	Scattering length
V	Fermi pseudo-potential
I	Intensity signal
$d\Omega$	Differential solid angle
$J(r, \theta, \phi, t)$	Flux of the scattered particles
J_0	Initial neutron flux
$\partial\sigma/\partial\Omega$	Differential cross section
$\partial^2\sigma/\partial\Omega\partial E_f$	Double differential cross section
$\partial^2 n/\partial\Omega\partial E_f$	Double differential density of state
$ \vec{k}_i\rangle$	Neutron initial state
$ \vec{k}_f\rangle$	Neutron final state
$P(\vec{k}_i\rangle \rightarrow \vec{k}_f\rangle)$	Probability transition
$ \psi_{k_i}\rangle$	Neutron initial state for wave plane

Symbol	Name
$ \psi_{k_f}\rangle$	Neutron final state for wave plane
ψ_{k_i}	Wave function of neutron initial state
ψ_{k_f}	Wave function of neutron final state
$ i\rangle$	Target initial state
$ f\rangle$	Target final state
χ_i	Wave function of target initial state
χ_f	Wave function of target final state
σ_{inc}	Incoherent cross section
σ_{coh}	Coherent cross section
$S_{inc}(\vec{Q}, \omega)$	Incoherent scattering functions
$S_{coh}(\vec{Q}, \omega)$	Coherent scattering functions
$I(\vec{Q}, t)$	Intermediary scattering function
$G_{\text{self correlation}}(\vec{r}, t)$	Self correlation function
τ_J	Jump-time
l_J	Jump-lengths
τ_r	Residence time
D_T	Translational diffusion coefficient
D_R	Rotational diffusion coefficient
$\langle \vec{u}^2 \rangle$	Mean Square Displacement
θ_B	Scattering Bragg angle
y_i	Data points
σ_i	Data points errors
M	Number of parameters
$\vec{a} = (a_1, \dots, a_M)$	Set of parameters
$\chi^2(\vec{a})$	χ^2 function
χ_{red}^2	reduced χ^2
χ_{min}^2	minimum χ^2
$\mathcal{D}_{(0)}$	Data set
F_{fast}	Fraction of fast water over total water
F_{slow}	Fraction of slow water over total water
R_{tral}	Translational Retardation Factor
R_{rot}	Rotational Retardation Factor

List of Acronyms

ACF	AutoCorrelation Function
NS	Neutron Scattering
ENS	Elastic Neutron Scattering
QENS	Quasi Elastic Neutron Scattering
EISF	Elastic Incoherent Structure Factor
MSD	Mean Square Displacement
SNS	Spallation Neutron Source
ILL	Insitute Laue-Langevin
FRM II	Forschungs-Neutronenquelle Heinz Maier-Leibnitz
ToF	Time-of-Flight
HFR	High Flux Reactor
PSD	Position Sensitive Detectors
P	Pulsing Choppers
CO	Contaminant Order Chopper
FO	Frame Overlap Chopper
M	Monochromator Choppers
LAMP	Large Array Manipulation Program
IDL	Interactive Data Language
HDF	Hierarchical Data Format
FWHM	Full Width at Half Maximum
ECS	ExtraCellular Space
ICS	IntraCellular Space
NaCl	Sodium Chloride
KCl	Potassium Chloride

RBC Red Blood Cells

E. coli Escherichia coli

Hmm Haloarcula marismortui

MD Molecular Dynamics

ADC Apparent Diffusion Coefficient

MRI Magnetic Resonance Imaging

fMRI Functional Magnetic Resonance Imaging

dMRI diffusion Magnetic Resonance Imaging

DW-MRI Diffusion-Weighted Magnetic Resonance Imaging

RCH Right Cerebral Hemisphere

LCH Left Cerebral Hemisphere

RC Right Cerebellum

LC Left Cerebellum

NMR Nuclear Magnetic Resonance

GM grey matter

WM white matter

Chapter 1

Introduction

Water has been seen as a “matrix of life” by Paracelsus [1] and Szent-Györgyi [2], perhaps with different meaning from biophysical point of view, but with the common sentiment to emphasize the concept that water plays a role in sustaining alive the cells, hence to allow life. Which kind of life? At least the life known on earth, far from extreme condition of either heat or cold. Water seems the unique organic molecule that can perform this task. On this evidence, many works have been done in order to understand the role played by water molecules in living systems.

1.1 Overview of water dynamics in complex systems

Major abundance of water on the earth is in the bulk phases. Bulk water is characterized by free-like diffusion. From *Fick's law diffusion* [3], water molecules translate and rotate with translational and rotational diffusion coefficients of $2.3\text{-}2.6 \times 10^{-5} \text{ cm}^2 \text{ s}^{-1}$ and of $0.2\text{-}0.3 \text{ ps}^{-1}$ at about 300 K, respectively. Such water properties change when water molecules interact with molecules, macromolecules or complex systems such as cells or tissues. Indeed, cells consists in a shell of molecular membrane containing organelles in a cytoplasmic environment. Such constituents are made of macromolecules, proteins, lipids, enzymes, etc. organized to perform important living functions. In particular, the cytoplasm typically contains up to 400 g/L of macromolecules, occupying a percentage between 5 to 40 of the total volume accessible within the cell [4].

On the other hand, tissues are made of different kinds of cells, fibers and others biological constituents, assuming ordered and disordered structures depending on the kind of cells.

Thus, the aim of different studies in the scientific community was to characterize water in such crowded systems. However no consensus has been reached concerning water dynamics properties as argued by *Ball* [5, 6].

Essentially, there are two lines of thinking. The first one suggests that water molecules

show reduced diffusion properties. In fact, some works from Nuclear Magnetic Resonance (NMR), as those of Tsukahara et al. [7] show that diffusion rates of water is 3-8 times reduced in mitochondrion and endoplasmic reticulum. Also, *Pollack* suggests that cytoplasm is like a “gel” in which water has property of a “sluggish fluid” [8]. On the other hand, the second line of thinking suggests that living systems are “tamed” by bulk water, with the property to be “more structured” [9, 10, 11]. It means that water molecules have more tendency to assume tetrahedral conformation creating a three-dimensional network such to keep however an high degree of disorder [12, 13].

Recent studies introduce a new interpretation of water in biological systems in which two kinds of water populations coexist. A majority percentage assumes property similar to the bulk one and a minority percentage shows reduced dynamics properties. The latter is the population that interacts with macromolecules, membranes, proteins, barriers and other constituents. For example, Persson et al. [14] by NMR experiment (time window of millisecond) found two water populations on *Haloarcula marismortui* (*Hmm*), an organism that lives under extreme conditions. A majority percentage of water cells has a bulk-like dynamics and the remaining shows slow dynamics with a reduced translational diffusion coefficient of a factor 15. The authors interpret such minority component as a hydrations shell of water molecules around biomolecules, macromolecules, etc. that interact with each others. As a consequence of these interactions water molecules exhibit a slow down in dynamics. Another work based on QENS experiment, with observation time window of 800 ps, comes from *Tehei et al.* [15]. They distinguish two water populations in *Haloarcula marismortui*, one is similar to the bulk one, while the second is a hydration water with a slow down in dynamics with a reduced translational diffusion coefficient of a factor 250. However, due to the different observation time windows, it does not seem to be the same kind of water found by Persson et al. [14]. Others controversial results come from Jasnin et al. [16], that using QENS technique (time window between 7 and 40 ps) did not find such two water components in deuterated *Escherichia coli* (*E. coli*).

In Table 1.1 are listed some of translational and rotational diffusion coefficients, residence and rotational times obtained in literature for bulk water in different systems. The parameters are sorted from low to high temperatures in a range between 263 and 301 K. Bulk water parameters values come from pure water, water in presence of salts as Sodium Chloride (NaCl) or Potassium Chloride (KCl) and water in biophysical systems as deuterated *E. coli*, Red Blood Cells (RBC) and *Hmm*. The techniques used in order to extract values of physical parameters are QENS with observed time window between 0.1 and 40 ps, isotopic, NMR and Molecular Dynamics (MD).

Concerning pure water at ~ 300 K translational diffusion coefficient ($D_{R,\text{bulk water}}$) assumes value between 2.2 and $2.6 \times 10^{-5} \text{ cm}^2 \text{ s}^{-1}$, the residence time ($\tau_{r,\text{bulk water}}$) exhibits values between 0.9 and 1.2 ps and the rotational diffusion coefficient ($D_{R,\text{bulk water}}$) assumes value between 0.25 and 0.5 ps^{-1} , which correspond to a rotational time ($\tau_{R,\text{bulk water}}$) between 2 and 4 ps.

T [K]	Water type	Sample [ref]	D_T [$10^{-5} \text{ cm}^2 \text{ s}^{-1}$]		τ_0 [ps]		D_R [ps^{-1}]		τ_R [ps]		Tech.	fwhm [μeV]	Δt [ps]		
			value	err	value	err	value	err	value	err					
263	ICS	pure water [17]	0.7		6.47						QENS	IN6	100	10	
273		pure water [18]	1.1		3						QENS				
278		pure water [17]	1.3		2.33						QENS	IN6	100	10	
281		D E. coli [16]	1.53	0.05	2.63	0.11					QENS	IRIS	17	40	
281	ICS	D E. coli [16]	1.78	0.08	2.95	0.11	0.51	0.04	1.96	0.07	QENS	IN6	90	7	
281	ICS	D E. coli buffer [16]	1.68	0.04	1.48	0.07	0.53	0.04	1.89	0.07	QENS	IRIS-IN6	17-90	7	
283		pure water [19]	1.67								Isotopic				
283		3.5 M NaCl [20]	1.26								Isotopic				
283		3 M KCl [20]	1.76								Isotopic				
285		Pure water [17]	1.6		1.66						QENS	IN6	100	10	
285		Hmm cells [21]	1.3								QENS	IN6-IN16	70-0.9	10-0.1	
285		Hmm cells[15]	1.29		6.12		0.18		1.83		QENS	IN6	70	10	
285		4 M NaCl [U.D]	1.5								QENS				
285		3 M KCl [U.D.]	>2								QENS				
288		pure water [22]							3.68		NMR				
290		ICS	RBC [23]	1.52		2.53	0.06					QENS	IRIS	17	40
290			pure water [23]	~ 2.2		0.57	0.03					QENS	IRIS	17	40
290		ICS	RBC [23]	1.52		1.12	0.05					QENS	FOCUS	50	13
290			pure water [23]	~ 2.2		1.02	0.09					QENS	FOCUS	50	13
290		ICS	RBC [23]	1.52		1.68	0.03					QENS	TOFTOF	100	10
290		pure water [23]	~ 2.2		0.68	0.03					QENS	TOFTOF	100	10	
294.4		pure water [24]							3.3		QENS				
298		pure water [19]	2.57								Isotopic				
298		pure water [25]	2.229								Isotopic				
298		pure water [26]	2.3		1.1		0.30		3.3		QENS	MIBEMOL	29-96	7-24	
room		pure water [27]	2.4				0.25		4		NMR				
300		pure water [28]	2.441				0.29		3.46		MD				
300		pure water [29]	2.43	0.03			0.50	0.03	2.00	0.05	MD				
301	ICS	D E. coli [16]	2.39	0.05	2.16	0.05					QENS	IRIS	17	40	
301	ICS	D E. coli [16]	2.94	0.4	2.28	0.27	0.65	0.05	1.54	0.08	QENS	IN6	90	7	
301		D E. coli buffer [16]	2.72	0.17	1.04	0.15	0.68	0.05	1.47	0.08	QENS	IRIS-IN6	17-90	40-7	

Table 1.1: Translational and rotational parameters of bulk water in pure state, in cells pellet, in concentrated solutions collected in literature. D E. Coli is deuterated E. Coli cells, Red Blood Cells (RBC), IntraCellular Space (ICS), Haloarcula marismortui (Hmm) and Molecular Dynamics (MD) by simulations.

Water dynamics is extensively studied as probe of even complex biological systems: brain tissues from humans, rats, bovines, monkeys, etc. Thus, many techniques as Func-

tional Magnetic Resonance Imaging (fMRI), diffusion Magnetic Resonance Imaging (dMRI) and Diffusion-Weighted Magnetic Resonance Imaging (DW-MRI) are used to investigate water dynamics in order to characterize ill and normal brain tissues. Different modelling approaches, as for example mono-exponential model [30], bi-exponential model [31, 32, 33] and kurtosis model [34, 35, 36, 37], lead to significant discrepancies in the results. In particular, the mono-exponential model describes only one type of water [38]. While, bi-exponential and kurtosis model suggest the description of two water pools, which were conjectured in some works - wrongly - to be respectively in IntraCellular Space (ICS) and in ExtraCellular Space (ECS). In fact, these works suggest that ECS water is characterized by a diffusion coefficient similar to bulk water with a contribution to the total signal of $\sim 80\%$, while ICS water is characterized by a diffusion coefficient smaller with respect the ECS one, and with a contribution to the total signal of $\sim 20\%$. On the other hand, others studies [39, 40, 41] disproved this conjecture. In fact, they found evidence that ICS and ECS consist in $\sim 80\%$ and $\sim 20\%$ of the total volume accessible to water molecules, respectively.

Recently Sehy et al., studying ICS of *Xenopus* oocyte using MRI, argued that “It could be assumed that brain intracellular water is made up of both fast and slow fractions. Further, brain extracellular water may include either the fast component alone or both components. In either case, the diffusion component(s) of the extracellular compartment could be indistinguishable from those of the intracellular compartment. This model of tissue water diffusion could explain the discrepancies between the fast and slow total water diffusion components typically shown in brain ($\sim 70:30$), and the volume fractions of the extra- and intra- cellular spaces ($\sim 20:80$)” [42]. Similarly Ronen *et al.* [43], Mulkern *et al.* [44] and Pyatigorskaya *et al.* [45] argued that is not straightforward to associate fast and slow populations to extra and IntraCellular Space, respectively. It should also be noted that Magnetic Resonance Imaging (MRI) techniques are intrinsically limited to the millimeter/millisecond space/time scales. First QENS experiments on animal post-mortem brain tissues were performed by Natali et al. [46] in 2012. They proposed a theoretical model to describe water diffusion in brain tissues where slow and fast populations are associated two water components with different dynamics properties without distinguish between ICS and ECS compartments. Moreover, experimental parameters such as stability in time of the proton dynamics, data reproducibility and changes in the tissues dynamics upon the conservation protocol, cryogenic towards formalin addition, have been carefully investigated guarantying the feasibility of such kind of experiments.

1.2 Aim of the project

As discussed in the previous section, there are controversial results concerning water dynamics in complex systems as cells and tissues. The discrepancy in these results are probably connected with the different techniques that work on different time windows and

with the different theoretical approaches.

This thesis is done in the context of a project that aims to contribute in clarifying water dynamics in complex systems. In the specific, we support the thesis that the presence of two water populations is a general property of systems where water is the solvent of macromolecules, cells and tissues. For this purpose, a theoretical model that aims to describe two different water populations as a general property of the biophysical systems is proposed [46, 47]. According to our model, when water interacts with macromolecules, proteins, membranes etc. a fraction of the total water changes its dynamics. Thus “fast water” and “slow water” populations coexist with different dynamics properties. Fast water population consists in a major fraction of the total water and it has still dynamics properties similar to the bulk one. On the other hand, slow water population is the remaining fraction that shows a slow down in dynamics properties due to the mutual interactions of water and macromolecules, proteins, membranes etc.

In this thesis we propose to study biophysical systems of different degree of complexity (from sucrose solutions to cells and brain tissues) using Neutron Scattering (NS) technique, analyzing the results using the above mentioned model. Quasi Elastic Neutron Scattering (QENS) technique is sensible to detect hydrogens dynamics and has access to atomic scale (nanometer/nanosecond or angstrom/picosecond - depending on instrumental resolution - space/time scales). In our investigations we will quantify the fractions of such two components for our samples and the slow down in dynamics of slow water component with respect to the fast one by translational and rotational retardation factors.

1.3 Thesis organization

In Chapter 2 we will present a brief introduction on basic knowledge of neutron scattering theory, where we will see how from microscopic interactions can be extracted information on macroscopic physical quantity. Then we will present a short introduction on the fission neutron source used in the experiments and the description of the instruments used to perform the experiments presented in Chapters 4, 5 and 6.

In Chapter 3 we will present the data treatment, the proposed theoretical model to describe hydrogens motions and the strategy used to analyze QENS spectra. In fact, we propose a global fit method applied on two combined sets of QENS spectra coming from experiments performed at two different energy resolutions. Such strategy was previously used by Gerelly *et al.* [48] on QENS experiment on lipid. Afterwards, the theoretical model expressed in Eq. 3.1 was first time used to analyze brain tissues QENS data at only high energy resolution ($FWHM \sim 10 \mu\text{eV}$) by Natali *et al.* [46] in order to perform the experimental and analysis protocol. First successful evidences of such a strategy were reported in 2015 by Martínez *et al.* [49] on *E. coli* investigation and very recently by our group [50] on water dynamics versus cells biodiversity. We will also show the confidence limit investigation on the global parameters which are defined with a confidence interval

of 99%.

In Chapter 4 we will present QENS experiments on bulk water carried out on IN6 at energy resolution of 70 μeV . The bulk water data were analyzed with the method presented in Chapter 3 to be used as a reference. We will also present QENS experiments on sucrose in aqueous solutions with concentration of 10, 20 and 30% on the total weight using IN5 at high and low energy resolutions (FWHM \sim 10 and 70 μeV) at 300 K. We will see that due to the mutual interaction between water and sucrose molecules fast and slow water components appears already at low 10% sucrose concentration.

In Chapter 5, increasing the complexity of the investigated systems, we will present QENS experiments for *Escherichia coli* (E. coli), Glioma-9L and yeast cells carried out using IN5 at high and low energy resolutions (FWHM \sim 10 and 70 μeV) at 300 K. We will see that the theoretical model can describe the two water populations in cells of different shapes and sizes. *Escherichia coli*, being a reference in literature, was investigated also at 310 and 320 K in order to evaluate the readability of the theoretical model. In the Appendix C.1 Elastic Neutron Scattering experiment, performed on the same cell samples using IN13, will be presented as complementary information.

In Chapter 6, we will further increase the complexity of the analyzed samples by presenting QENS experiments on right and left sides of hemisphere and cerebellum from bovine brain tissues carried out on TOFTOF instrument at high and low energy resolutions (FWHM \sim 10 and 70 μeV) at 300 K. In particular, we will focus the attention on the lateralization effect. QENS experiments confirm the existence of two water populations giving more details on diffusion properties of water molecules in brain tissues.

In Chapter 7 we will present our final remarks, summarizing how our results seem to confirm the existence of fast and slow water populations as general properties of systems where water is the solvent. We will also mention analysis in progress on other phantom systems, brain tissues from bovine and rat.

Chapter 2

Neutron scattering theory

2.1 Neutrons

In the 1931, Ettore Majorana was the first to assume the existence of uncharged particle with a mass similar to the one of the proton to explain some experimental results in the scientific community. The following year James Chadwick proved the existence of such particle winning the Nobel Prize in the 1935 [51][52]. The neutron is defined as a subatomic particle with mass $m_n = 1.67 \times 10^{-27}$ kg, with spin $1/2$. It is a fermion with a magnetic moment $\mu_n = -1.91\mu_B$, where μ_B is Bohr magneton $\frac{e\hbar}{2m_e}$, \hbar is the reduced Planck constant and m_e is the electron mass. The atoms nucleus consists of protons and neutrons, the latter reduce the repulsion between protons and they are all together stable in the nucleus via the nuclear forces. On the other hand, a free neutron, separated from his nucleus, is unstable and it undergoes in a β decay with a mean lifetime of about 15 minutes. The long lifetime and the uncharged property make the neutrons suitable to probe the matter in deep and without any damage¹ to the sample.

Consider N neutrons in a diluted gas. They are treated as non-relativistic particles, since their velocity is much smaller than that of light ($c \sim 3 \times 10^8$ m s⁻¹). In fact, the classical associated kinetic energy is:

$$E_{kin} = \frac{1}{2}m_nv^2, \quad (2.1)$$

where the speed v is Maxwell distributed. The most probable speed [53] trough statistical calculation of the neutrons is

$$\bar{v} = \sqrt{\frac{2k_BT}{m_n}}, \quad (2.2)$$

where k_B is the Boltzmann constant 1.38×10^{-23} m² kg s⁻² K⁻¹. For example, neutrons at room temperature 300 K exhibit an internal energy of 25 meV and a \bar{v} of 2.2×10^4 m s⁻¹

¹By “any damage to the sample” we assume that during the experiment the neutron beam does not change properties and characteristics of the investigated sample. This is not always true.

that is much smaller than c . More details in the Appendix A.1. The internal energy of thermal neutrons is the same found in interatomic or intermolecular interactions. Due to the double nature of the particles, a de Broglie wavelength is related to the neutron:

$$\lambda = \frac{h}{m\bar{v}}, \quad (2.3)$$

replacing Equation 2.2 in Equation 2.3 we obtain the follow relation:

$$\lambda = \frac{h}{\sqrt{2m_n k_B T}}. \quad (2.4)$$

The de Broglie wavelength of 1.8 \AA is associated to thermal neutrons. This physical quantity is comparable in term of size with interatomic lattice distance or bond length into molecules. Therefore a neutron scattering experiment between a neutron beam and a target gives information about dynamics and structural properties without destroying the sample².

2.2 Scattering event

Two process occur when a neutron passes close enough to a nucleus to feel nuclear forces:

- absorbing process: the neutron is captured by the nucleus that undergoes in an excited state; thus a *compound nucleus*³ is formed. Such compound nucleus decays in the ground state through capture reaction where γ rays are emitted or throughout fission reaction where the nucleus is split into two or more lighter parts.
- scattered process that will be extensively discussed.

In the scattering event we treat the collision between a neutron with a nucleus as a weak perturbation that moves the system from a initial state to a final excited state. The response of the system to such weak perturbation can be related to the *AutoCorrelation Function (ACF)* of the system in the thermodynamic equilibrium. In the scattering event we distinguish three cases:

- elastic case: only quantum momentum is transferred during the process. The neutron with a initial vector \vec{k}_i is scattered with a final vector \vec{k}_f which has same module, but different orientation. Elastic Neutron Scattering (ENS) experiment gives information on nuclei thermal vibrations.

²See note 1

³A compound nucleus is created when incident particle and the target nucleus become indistinguishable after the collision and together constitute the particular excited state of nucleus

- inelastic case: energy and momentum are transferred during the process. The neutron with a initial vector \vec{k}_i and initial energy E_i is scattered with a final vector \vec{k}_f and final energy E_f . The neutron loss energy if $E_f - E_i < 0$ while it gains energy if $E_f - E_i > 0$. Inelastic neutron scattering (INS) experiment gives information on lattice vibrations (phonons propagation).
- quasi elastic case is a particular case of the inelastic one: the energy transfer is about ± 2 meV. QENS experiment gives information on translation and rotational diffusive motion of nuclei.

We define the *momentum transfer vector* as:

$$\vec{Q} = \vec{k}_f - \vec{k}_i. \quad (2.5)$$

Through some trigonometric observation the momentum transfer is related to the wavelength of the incident neutron beam by:

$$Q = \frac{4\pi \sin(\theta/2)}{\lambda_i}. \quad (2.6)$$

where λ_i is the initial wavelength. While, the *energy transfer* is expressed as follows:

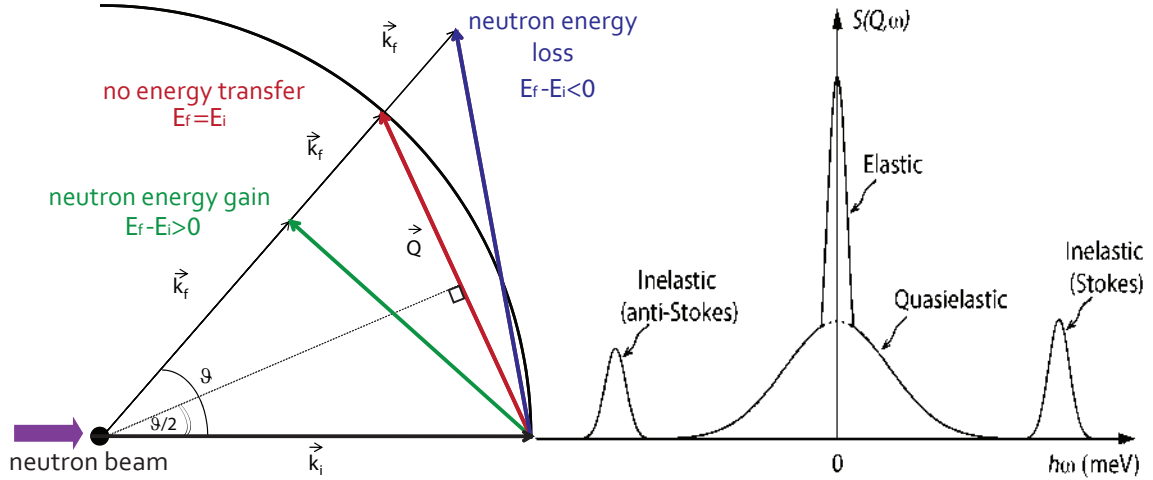


Figure 2.1: Left side: schematic representation of the scattering event between an incoming neutron beam with a target. Right side: Schematic illustration of a neutron scattering spectrum, containing elastic, inelastic, and quasielastic components [54].

$$E_f - E_i = \frac{\hbar^2}{2m} (\vec{k}_f^2 - \vec{k}_i^2). \quad (2.7)$$

2.2.1 AutoCorrelation Function

Given a system of N particles having ν degrees of freedom each, a stochastic variable A with νN coordinates q_i and νN momentum p_i is defined:

$$A(t) = A(q_i(t), p_i(t)) \quad (2.8)$$

The ACF is expressed as follows:

$$\text{ACF}(t', t'') = \langle A(t') A(t'') \rangle \quad (2.9)$$

where the angular brackets mean an ensemble average over initial condition or the average over time. Under the hypothesis of stationarity, the mean value of the stochastic variable does not depend from the time, i.e. it is independent from the time origin, $\text{ACF}(t', t'')$ is invariant under time translation. Therefore, $t' \rightarrow t = t' - t''$ and $t'' \rightarrow t_0 = t'' - t'' = 0$; Equation 2.8 becomes:

$$\text{ACF}(t, 0) = \langle A(t) A(0) \rangle. \quad (2.10)$$

Ergodic hypothesis is required to assure that the average over time converge to the ensemble average, thus $A(t, 0)$ for $t \rightarrow \infty$ explore all accessible microstates in the phase space. Such hypothesis is fundamental in statistic, where system of $N \sim N_A$ (Avogadro constant) is under study. For instance, if we are interested in investigating random variable as the velocity, during a certain time window, we need to look at the mean value of the velocity over the time window of each particle. In order to evaluate the mean value velocity of each particle has to be known at any time. In the ergodic case, the problem is reduced since such mean value corresponds to the mean value of one particle over the explored time. The importance of ACF is due to the property to connect microscopic quantities with the macroscopic ones. For example, studying a Brownian particle in a solution, the velocity ACF, which is a microscopic quantity, is directly connected with the macroscopic translation diffusion coefficient [55].

2.3 Scattering law

From quantum mechanics point of view, the Hamiltonian of the system neutron-scatter in presence of an external field is:

$$H = H_0 + H', \quad (2.11)$$

where H_0 is the unperturbed system and H' is the weak perturbation which can be expressed as follows:

$$H' = \int_0^\infty V(\vec{r} - \vec{r}') \rho_n(\vec{r}') d^3 r'. \quad (2.12)$$

The particle scattered and the scatters are in \vec{r} and \vec{r}' position, respectively. Through the scattering event, the neutron probe the nuclear density $\rho_n(\vec{r}')$ in the volume $d^3 r'$. Let us

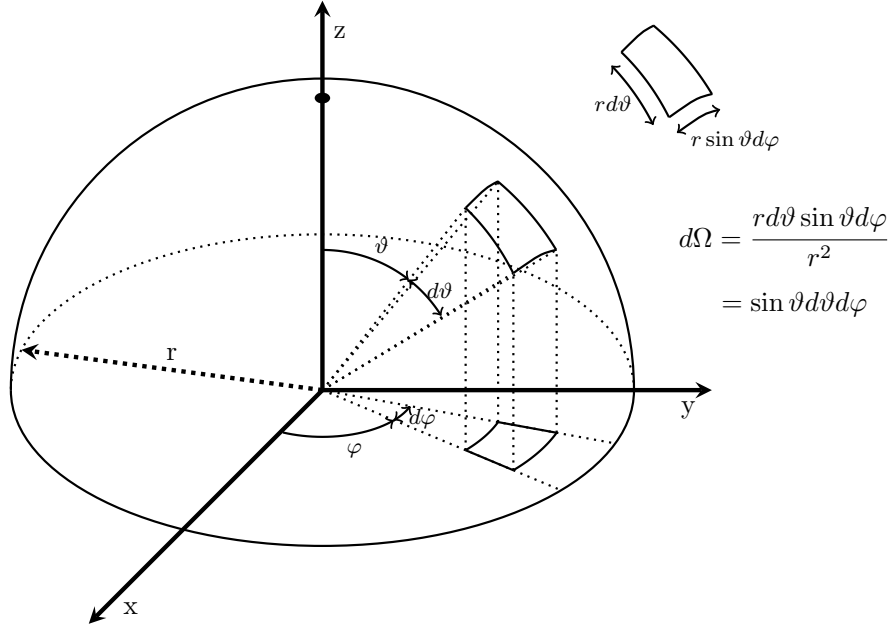


Figure 2.2: Schematic representation of the differential solid angle.

consider an incident monochromatic beam of neutrons represented by plane wave and a target with N identical scatters. The neutron-nuclear interaction occurs in a very short range, i.e an order of magnitude of nuclear size (10×10^{-15} m), which allows to described the perturbation by *Fermi pseudo-potential* [56]:

$$H' = V(\vec{r}, \vec{r}_i, t) = 4\pi \frac{\hbar^2}{2m_n} \sum_{i=1}^N b_i \delta(\vec{r} - \vec{r}_i), \quad (2.13)$$

where b_i is so-called *scattering length* and it is directly connected with the nuclei cross section, which is a quantity specific for each atom in the nature.

The probability transition of the neutron to pass from the initial state $|\vec{k}_i\rangle$ to the final state $|\vec{k}_f\rangle$ is the response of the system and we aim to determine it. On the other hand, in a neutron scattering experiment the intensity signal is measured. Such signal is proportional to the flux of the scattered particles and the detector area [57].

$$I(t) = J(r, \theta, \phi, t) dA. \quad (2.14)$$

From the Figure 2.2 $dA = r^2 \sin(\theta) d\theta d\phi = r^2 d\Omega$, where the *differential solid angle* $d\Omega = \sin(\theta) d\theta d\phi$. Therefore the intensity can be express as:

$$I(t) = J(r, \theta, \phi, t) r^2 d\Omega. \quad (2.15)$$

Dividing Equation 2.15 to the initial scattered flux J_0 we obtain:

$$d\sigma = \frac{J(r, \theta, \phi, t)}{J_0} r^2 d\Omega. \quad (2.16)$$

Thus, experimentally, is defined the *differential cross section* $\partial\sigma/\partial\Omega$ that measure the neutrons scattered in the solid angle $d\Omega$ over the initial neutrons flux. Analogously, we can defined the *double differential cross section* $\partial^2\sigma/\partial\Omega\partial E_f$ as the neutrons scattered in the solid angle between Ω and $\Omega + d\Omega$ and with a final energy between E_f and $E_f + dE_f$. The double differential cross section in the mathematical formalism is related to the probability transition that the scattering event occurs.

$$\frac{\partial^2\sigma}{\partial\Omega\partial E_f} = \frac{P(|\vec{k}_i\rangle \rightarrow |\vec{k}_f\rangle)}{J_0} \frac{\partial^2 n}{\partial\Omega\partial E_f}, \quad (2.17)$$

where $\partial^2 n/\partial\Omega\partial E_f$ represents the density of state in the solid angle between Ω and $\Omega + d\Omega$ and with a final energy between E_f and $E_f + dE_f$ and it is expressed as:

$$\frac{\partial^2 n}{\partial\Omega\partial E_f} = \frac{V}{(2\pi)^3} \frac{m_n k_f}{\hbar^2}. \quad (2.18)$$

For more details see Appendix A.2. The initial neutrons flux J_0 can be written as follows:

$$J_0 = \frac{1}{V} \frac{\hbar}{m_n} k_i. \quad (2.19)$$

In the Born approximation [58] the density of the scatters is low enough to assure that the scattering event occurs only between one neutron and one nucleus without any interaction with the others nuclei. The probability transition can be calculated by Fermi's golden rule [59]:

$$P(|\vec{k}_i\rangle \rightarrow |\vec{k}_f\rangle) = \frac{2\pi}{\hbar} |\langle \psi_{k_i i} | V(\vec{r}, t) | \psi_{k_f f} \rangle|^2 \delta(\hbar\omega - (E_f - E_i)), \quad (2.20)$$

where $|\psi_{k_i i}\rangle$ and $|\psi_{k_f f}\rangle$ are the initial and finale state for the neutron and the target. The neutrons are represented as a wave plane therefore the general wave function is written as:

$$|\psi_k\rangle = \frac{1}{\sqrt{V}} |k\rangle, \quad |k\rangle = \exp(i\vec{k} \cdot \vec{r}). \quad (2.21)$$

Replacing Equation 2.18, 2.19 and 2.20 in Equation 2.17 we obtain:

$$\frac{\partial^2\sigma}{\partial\Omega\partial E_f} = \left(\frac{m_n}{2\pi\hbar^2} \right)^2 \frac{k_f}{k_i} |\langle \vec{k}_i i | V(\vec{r}, \vec{r}_i, t) | \vec{k}_f f \rangle|^2 \delta(\hbar\omega - (E_f - E_i)). \quad (2.22)$$

We focus our attention in the element of matrix that is:

$$\begin{aligned}
 \langle \vec{k}_i | V(\vec{r}, \vec{r}_l, t) | \vec{k}_f \rangle &= \int d\vec{r} d\vec{r}_l \exp(-i\vec{k}_i \cdot \vec{r}) \chi_i^* V(\vec{r}, \vec{r}_l, t) \exp(i\vec{k}_f \cdot \vec{r}) \chi_f \\
 &= \int d\vec{r}_l \chi_i^* \hat{V}(\vec{Q}, t) \chi_f \\
 &= \langle i | \hat{V}(\vec{Q}, t) | f \rangle,
 \end{aligned} \tag{2.23}$$

where $\hat{V}(\vec{Q}, t)$ is the Fourier Transform in the k-space of real space function $V(\vec{r}, \vec{r}_l, t)$. The δ -Dirac function for the energy is an integral function over time:

$$\delta(\hbar\omega - (E_f - E_i)) = \frac{1}{2\pi\hbar} \int_{-\infty}^{\infty} dt e^{-i\omega t} e^{\frac{i(E_f - E_i)t}{\hbar}} \tag{2.24}$$

Replacing Equation 2.23 and 2.24, the Equation 2.22 becomes

$$\frac{\partial^2 \sigma}{\partial \Omega \partial E_f} = \left(\frac{m_n}{2\pi\hbar^2} \right)^2 \frac{k_f}{k_i} \frac{1}{2\pi\hbar} \int_{-\infty}^{\infty} dt e^{-i\omega t} \langle i | \hat{V}(\vec{Q}, t) | f \rangle \langle f | e^{i\frac{E_f}{\hbar}t} \hat{V}(\vec{Q}, t) e^{-i\frac{E_i}{\hbar}t} | i \rangle; \tag{2.25}$$

in the Heisenberg representation:

- $\langle i | V(\vec{Q}, t) | = V(\vec{Q}, 0);$
- $|f\rangle\langle f| = 1;$
- $e^{i\frac{E_f}{\hbar}t} V(\vec{Q}, t) e^{-i\frac{E_i}{\hbar}t} = V(\vec{Q}, t).$

Therefore Equation 2.25 may be written

$$\frac{\partial^2 \sigma}{\partial \Omega \partial E_f} = \left(\frac{m_n}{2\pi\hbar^2} \right)^2 \frac{k_f}{k_i} \frac{1}{2\pi\hbar} \int_{-\infty}^{\infty} dt e^{-i\omega t} \langle \hat{V}(\vec{Q}, 0) \hat{V}(\vec{Q}, t) \rangle. \tag{2.26}$$

Equation 2.26 is called “master equation” and it shows the relation between the double differential scattering cross section and the AutoCorrelation Function. Remembering that Equation 2.13 expresses a weak perturbation with the Fermi pseudo-potential, the previous Equation 2.26 becomes

$$\frac{\partial^2 \sigma}{\partial \Omega \partial E_f} = \frac{k_f}{k_i} \frac{1}{2\pi\hbar} \sum_{l,m} \langle b_l b_m \rangle \int_{-\infty}^{\infty} dt e^{-i\omega t} \langle e^{-i\vec{Q} \cdot \vec{r}_l} e^{i\vec{Q} \cdot \vec{r}_m} \rangle, \tag{2.27}$$

where the sum is done over N scatters, $l = 1, \dots, N$ and $m = 1, \dots, N$. We focus our attention on such sum in order to distinguish two important contributions.

$$\sum_{l,m} \langle b_l b_m \rangle = \sum_l \langle b_l^2 \rangle + \sum_{l \neq m} \langle b_l b_m \rangle. \tag{2.28}$$

If we sum and subtract $\sum_l \langle b_l \rangle^2$, this expression can be rewritten as

$$\begin{aligned}
 \sum_{l,m} \langle b_l b_m \rangle &= \sum_l (\langle b_l^2 \rangle - \langle b_l \rangle^2) + \sum_{l \neq m} \langle b_l b_m \rangle + \sum_l \langle b_l \rangle^2 \\
 &= \sum_l \langle b_l^2 \rangle - \langle b_l \rangle^2 + \sum_{l,m} \langle b_l b_m \rangle \\
 &= \sum_l (b_l^{inc})^2 + \sum_{l,m} b_l^{coh} b_m^{coh},
 \end{aligned} \tag{2.29}$$

where $\langle b_l b_m \rangle = \langle b_l \rangle \langle b_m \rangle = b_l^{coh} b_m^{coh}$ because the sites l and m are independents. We can separate the expression into two contributions, one sums over $l = m$ and the other one sums over each l and m .

$$\begin{aligned}
 \frac{\partial^2 \sigma}{\partial \Omega \ E_f} &= \frac{k_f}{k_i} \frac{1}{2\pi\hbar} \sum_l \frac{(b_l^{inc})^2}{4\pi} \int_{-\infty}^{\infty} dt e^{-i\omega t} \langle e^{-i\vec{Q} \cdot \vec{r}'_l(0)} e^{i\vec{Q} \cdot \vec{r}'_l(t)} \rangle + \\
 &+ \frac{k_f}{k_i} \frac{1}{2\pi\hbar} \sum_{l \neq m} \frac{b_l^{coh} b_m^{coh}}{\pi} \int_{-\infty}^{\infty} dt e^{-i\omega t} \langle e^{-i\vec{Q} \cdot \vec{r}'_l(0)} e^{i\vec{Q} \cdot \vec{r}'_m(t)} \rangle,
 \end{aligned} \tag{2.30}$$

where the incoherent σ_{inc} and the coherent σ_{coh} cross sections can be introduced as follows

$$\sigma_{inc} = 4\pi (b_l^{inc})^2, \tag{2.31}$$

$$\sigma_{coh} = 4\pi b_l^{coh} b_m^{coh}. \tag{2.32}$$

The $S_{inc}(\vec{Q}, \omega)$ and $S_{coh}(\vec{Q}, \omega)$ are the incoherent and coherent part of the dynamic *scattering functions* defined by:

$$S_{inc}(\vec{Q}, \omega) = \frac{1}{N} \frac{1}{2\pi\hbar} \sum_l \int_{-\infty}^{\infty} dt e^{-i\omega t} \langle e^{-i\vec{Q} \cdot \vec{r}'_l(0)} e^{i\vec{Q} \cdot \vec{r}'_l(t)} \rangle, \tag{2.33}$$

$$S_{coh}(\vec{Q}, \omega) = \frac{1}{N} \frac{1}{2\pi\hbar} \sum_{l \neq m} \int_{-\infty}^{\infty} dt e^{-i\omega t} \langle e^{-i\vec{Q} \cdot \vec{r}'_l(0)} e^{i\vec{Q} \cdot \vec{r}'_m(t)} \rangle. \tag{2.34}$$

The double differential cross section in terms of scattering function can be written as

$$\frac{\partial^2 \sigma}{\partial \Omega \ E_f} = \frac{N}{4\pi} \frac{k_f}{k_i} (\sigma_{inc} S_{inc}(\vec{Q}, \omega) + \sigma_{coh} S_{coh}(\vec{Q}, \omega)). \tag{2.35}$$

Let us focus our attention in the incoherent term, each step is analogous for the coherent one. We observe that scattering function is the time-Fourier transform of the so-called *incoherent intermediary scattering function*

$$I_{inc}(\vec{Q}, t) = \frac{1}{N} \sum_l \langle e^{-i\vec{Q} \cdot \vec{r}'_l(0)} e^{i\vec{Q} \cdot \vec{r}'_l(t)} \rangle. \tag{2.36}$$

In fact, Equation 2.33 may be written as

$$S_{inc}(\vec{Q}, \omega) = \frac{1}{2\pi\hbar} \int_{-\infty}^{\infty} dt e^{-i\omega t} I_{inc}(\vec{Q}, t). \quad (2.37)$$

In order to have a physical meaning of this function we shall return in the physical space defining the *self correlation function* as the space-Fourier transform of the intermediary scattering function:

$$G_{\text{self correlation}}(\vec{r}, t) = \frac{1}{(2\pi)^3} \int_{-\infty}^{\infty} d\vec{Q} e^{-i\vec{Q}\vec{r}} I_{inc}(\vec{Q}, t). \quad (2.38)$$

Replacing the incoherent intermediary scattering function in the self correlation function one gets

$$G_{\text{self correlation}}(\vec{r}, t) = \frac{1}{N} \int d\vec{R} \sum_l \langle \rho(\vec{R} - \vec{r}, 0) \rho(\vec{R}, t) \rangle. \quad (2.39)$$

where $\rho(\vec{R}, t)$ is the nuclear density mentioned in Equation 2.12. The self correlation function is normalized to one

$$\int d\vec{r} G_{\text{self correlation}}(\vec{r}, t) = N. \quad (2.40)$$

The clear interpretation of Equation 2.39 is that $G_{\text{self correlation}}(\vec{r}, t)$ is the probability to find the particle l in the position \vec{r}'_l at the time t when at zero time was in \vec{r}_l position. While in the general case the $G_{\text{correlation}}(\vec{r}, t)$ is the probability to find the particle l in the position \vec{r}'_l at time t in presence of the particle m in \vec{r}'_m position at zero time. The relation between the scattering function and the self correlation function is the following

$$S_{inc}(\vec{Q}, \omega) = \frac{1}{2\pi\hbar} \int_{-\infty}^{\infty} dt d\vec{r} e^{i(\vec{Q}\cdot\vec{r} - \omega t)} G_{\text{self correlation}}(\vec{r}, t). \quad (2.41)$$

The coherent scattering function $S_{coh}(\vec{Q}, \omega)$ gives information on structure and collective motions. While the incoherent scattering function $S_{coh}(\vec{Q}, \omega)$ gives information on the average motion of the same particle in a certain time.

The samples under study are biological, therefore there are many kinds of scatters. Nevertheless, we can assume that the most significant contribution comes from hydrogens. In fact, the 80% of weight is water, while the rest consists of membranes, proteins and other biological component that contains hydrogen themselves. Incoherent scattering cross section of hydrogen is bigger than incoherent and coherent cross sections from others kinds of atoms, see Table 2.1.

Element	$\sigma_{coh}(barns)$	$\sigma_{inc}(barns)$
H	1.76	79.91
O	4.23	0.01
Si	2.16	0.02
D	5.60	2.04
C	5.55	0.00
N	11.01	0.49
F	4.02	0.00
Na	1.66	1.62
Al	1.49	0.01
P	3.31	0.01
Ge	8.42	0.18
V	0.02	5.19
Cu	7.49	0.55
Cd	3.30	0.00

Table 2.1: Incoherent and coherent cross section value of some elements. The cross section is given in units of barns, $1\text{ b}=10^{-24}\text{ cm}^2$.

2.4 Neutron scattering signal

2.4.1 Quasi Elastic Neutron Scattering

The energy resolution of the instrument for neutron scattering experiments defines the observable time window, that typically is in a range between order of ps to hundreds of ps. The chosen energy resolution defines which kinds of motions can be observed during an experiment.

In a QENS experiment, immediately before the scattering event the atom l at time $t = 0$ is in the equilibrium position $\vec{r}_l'(0)$, after such process at time t it will be in a final position $\vec{r}_l'(t)$. The scattering function describes how the atom l relax to the initial thermodynamic equilibrium. During the relaxation time we can distinguish typically three main motions:

- vibration motion: the atom makes translational vibrations that deform the bond length between atoms;
- translation motion: the atom translates in the accessible space;
- rotation motion: the atom re-orientate itself in the any accessible space orientation.

Therefore,

$$\vec{r}(t) = \vec{r}_V(t) + \vec{r}_T(t) + \vec{r}_R(t). \quad (2.42)$$

The total incoherent intermediary scattering function is directly connected with molecules motions, as previously mentioned. We assume that such kind of motions are independent and give the following contribution to the total intermediary scattering function

$$I_{inc}(\vec{Q}, t) = I_{inc,V}(\vec{Q}, t) \cdot I_{inc,T}(\vec{Q}, t) \cdot I_{inc,R}(\vec{Q}, t). \quad (2.43)$$

Thanks to the convolution theorem for Fourier transform, see Appendix A.5:

$$S_{inc}(\vec{Q}, \omega) = S_{inc,V}(\vec{Q}, \omega) \otimes S_{inc,T}(\vec{Q}, \omega) \otimes S_{inc,R}(\vec{Q}, \omega). \quad (2.44)$$

The vibrational contribution $S_{inc,V}(\vec{Q}, \omega)$ may be written [60]

$$S_{inc,V}(\vec{Q}, \omega) \propto e^{-2\langle u^2 \rangle Q^2} \delta(\omega). \quad (2.45)$$

The convolution between a Dirac- δ function and a given function F returns F itself, therefore

$$S_{inc}(\vec{Q}, \omega) \propto e^{-2\langle u^2 \rangle Q^2} [S_{inc,T}(\vec{Q}, \omega) \otimes S_{inc,R}(\vec{Q}, \omega)]. \quad (2.46)$$

In order to understand the mathematical model concerning the translational and rotational components we split the intermediary scattering function in two components:

- time-dependent component, $I(\vec{Q}, t)$;
- time-independent component, $I(\vec{Q}) = \sum |\exp(i\vec{Q} \cdot \vec{r}_l)|^2 / N = I_0$, where the atom does not change its dynamics. Therefore the AutoCorrelation Function disappears becoming a constant.

$$I_{inc}(\vec{Q}, t) = I_0 + I_{inc}(\vec{Q}, t). \quad (2.47)$$

In terms of scattering function we obtain

$$\begin{aligned} S_{inc,T}(\vec{Q}, \omega) &= I_{0,T} \delta(\omega) + S_{inc,T}^{qe}(\vec{Q}, \omega); \\ S_{inc,R}(\vec{Q}, \omega) &= I_{0,R} \delta(\omega) + S_{inc,R}^{qe}(\vec{Q}, \omega). \end{aligned} \quad (2.48)$$

The first contribution is elastic and is called Elastic Incoherent Structure Factor (EISF), while the second component is the quasi elastic contribution. In liquid systems, the elastic translation scattering function is null, $I_{0,T} \delta(\omega) = 0$. Replacing Equation 2.48 in the 2.46 the total scattering function is

$$S_{inc}(\vec{Q}, \omega) \propto e^{-2\langle u^2 \rangle Q^2} [S_{inc,T}^{qe}(\vec{Q}, \omega) \otimes (I_{0,R} \delta(\omega) + S_{inc,R}^{qe}(\vec{Q}, \omega))]. \quad (2.49)$$

In order to obtain the true scattering function, i.e. the measured scattering function, the theoretical one has to be convoluted with the instrumental energy resolution.

$$S_{inc}^{\text{measured}}(\vec{Q}, \omega) = S_{inc}(\vec{Q}, \omega) \otimes R(\vec{Q}, \omega). \quad (2.50)$$

The General approach to describe the quasi elastic incoherent scattering function uses sum of Lorentzian functions. Each Lorentzian function is normalized and weighted with a fraction proportional to their own contribution in order to easily evaluate the amount of each contribution. In the next subsection, we present the theoretical model used to describe translation and rotational scattering function that links stochastic and macroscopic physical quantity.

Jump diffusion model

The most simple diffusion motion is the Brawnian motion. N particles in a box as ideal gas in a thermal equilibrium diffuse interacting rarely between each other and having no preferred direction. After one collision, the particle diffuses following a straight line and it loses its memory history after the characteristic time τ . In the other words, the stochastic observables are uncorrelated. Fick's law [61] well describes Brownian motion and gives the relation between the mean square displacement in three-dimensional space with translation diffusion motion:

$$\langle \mathbf{r}^2 \rangle = 6D_T\tau. \quad (2.51)$$

In QENS experiment, the quasi elastic neutron scattering function is well described with the *continuous diffusion model* that consists in a single Lorentzian function with width $\Gamma = D_TQ^2$.

Translation motions in crowded systems show a deviation from Brawnian motions because the particles interact so frequently to be correlated. In such case, a model to describe translation dynamics is with *jump-diffusion model* by Sigwi and Sjölander [62]. In this model, the particle jumps between one site and a neighboring one in a jump-time τ_J and covering a jump-lengths l_J . It seems as the system is lattice-like with a high density of vacancies. During a jump, the particle has a random-walk diffusion. In the model, $G(\mathbf{r}, t)$ is obtained dividing the motion in $2N+1$ steps. In the zero step the particle vibrates around equilibrium position for a *residence time* τ_r with an oscillations amplitude $\langle R^2 \rangle$. After that, it takes place the step 1 where, the particle jumps in a time τ_J having a random-walk diffusion. In the step 2 again, the particle oscillates in the new equilibrium position and so on until $2N$ step, therefore the model describe N jumps.

$$G(\mathbf{r}, t) = \sum_{i=0}^{2N} F_i(\mathbf{r}, t), \quad (2.52)$$

where $F_i(\mathbf{r}, t)$ are the probability associated to each step processes. For the calculation of this $2N$ terms and generic expressions for $G_S(\mathbf{r}, t)$ and $S(Q, \omega)$ see [60]. Under the assumption that the residence time τ_r is much longer than jump-time, τ_J (the time spent to self-diffuse is much shorter than the spent to oscillate in equilibrium position) the

incoherent scattering function becomes:

$$S_{inc}(Q, \omega) = e^{-2\langle R^2 \rangle Q^2} \frac{1}{\pi} \frac{\Gamma}{\omega^2 + \Gamma^2}, \quad (2.53)$$

where $e^{-2\langle R^2 \rangle Q^2}$ is the incoherent scattering function of internal vibration and the lorentzian function expresses the quasi elastic translation function with Γ equal to

$$\Gamma = \left[1 - \frac{\exp(-\langle R^2 \rangle Q^2)}{1 + D_T \tau_r Q^2} \right] \frac{1}{\tau_r}. \quad (2.54)$$

In the case $\langle R^2 \rangle Q^2 \ll 1$ and $\langle R^2 \rangle \ll l_j^2$ the $S(Q, \omega)$ is simplified in a lorentzian function with a broadening that describes translational motion, therefore we introduce the apex Γ in the notation:

$$S_{inc,T}^{qe}(Q, \omega) = \frac{1}{\pi} \frac{\Gamma_T}{\omega^2 + (\Gamma_T)^2}, \quad (2.55)$$

where,

$$\Gamma_T = \frac{D_T Q^2}{1 + D_T \tau_r Q^2}; \quad (2.56)$$

where D_T is the translation diffusion coefficient that is in relation with the microscopical dynamics. In the limit case, $Q^2 D_T \tau_r \ll 1 \Rightarrow \Gamma_T = Q^2 D_T$, we turn back to continuous diffusion model. Γ as a function of Q^2 is well described in a large Q -range as from 0 to 2 \AA^{-1} . The inverse residence time is the asymptotic Γ value, therefore the bigger is the Q -range the easier will be define such time.

Continuous rotational on a circle model

In *continuous rotational on a circle model* [64] the particle rotates covering a surface of constant radius r . In water molecule case, the rotation occurs around oxygen atom and the radius r_B is the hydrogen-oxygen bond length, which is equal to 0.98 \AA . A rotational distribution function describes the probability to rotate of a certain angle in a interval of time t . The associated scattering function is:

$$S_{inc,R}(Q, \omega) = j_0^2(r_B Q) \delta(\omega) + \sum_{i=1}^{\infty} (2i+1) j_i^2(r_B Q) \frac{1}{\pi} \frac{\Gamma_{i,R}}{\omega^2 + (\Gamma_{i,R})^2}, \quad (2.57)$$

where,

$$\Gamma_{i,R} = t(i+1)D_R, \quad (2.58)$$

where $j_t(Qr)$ with $t=0, \dots, \infty$ are the spherical Bessel functions and D_R is the rotational diffusion coefficient. The broadening of lorentzian functions is independent in Q . The dependence in Q is contained in the spherical Bessel functions, which are the *quasi elastic structure factors* of the quasi elastic scattering function.

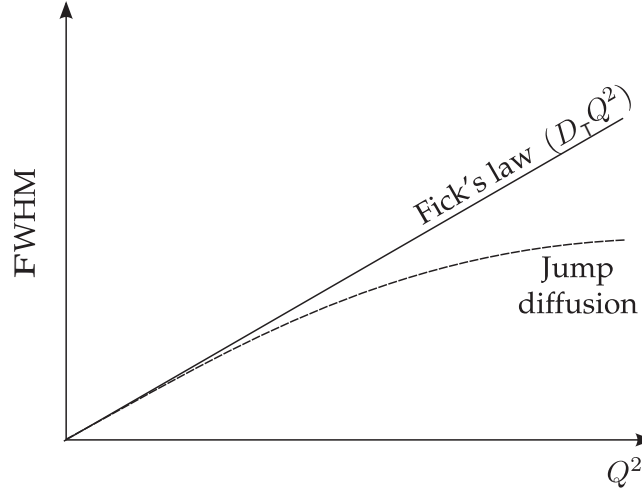


Figure 2.3: Broadening of the quasi elastic peak for a system where Fick's law is satisfied (continuous line) and for a system with jump diffusion (dashed line) [63].

2.5 Neutron sources

In neutron scattering research, the neutron beam is produced in a nuclear reactor or in a Spallation Neutron Source (SNS):

- In a nuclear reactor the neutron beam is produced by chain reaction of nuclear fissions. In a fission reaction, an initial element splits in two lighter elements producing γ rays and three neutrons. Those latter neutrons will hit others fuel elements and each of them will be split in two lighter part producing γ rays and three neutrons as well and so on. If the quantity of fuel is big enough a chain reaction that does not collapse will take place. In nature, different heavy elements undergo spontaneously in fission reaction. On the other hand, isotopic heavy elements have to be inducted in fission reaction by absorbing a neutron. They are called *fissionable* or *fissile* if they are struck by a free neutron or thermal slow neutron.
- In a spallation neutrons source the neutron beam is created by a spallation reaction. A light projectile, as a proton, with energy of an order of magnitude between 100 MeV and GeV, collides with an heavy element. After such impact the heavy metal emits isotropically a large number of neutrons or fragments by evaporation. The protons with high energy, used as projectile, are produced accelerating protons in a synchrotron.

The experiments presented in this thesis were performed at Insitute Laue-Langevin (ILL) in Grenoble (France) and at Forschungs-Neutronenquelle Heinz Maier-Leibnitz (FRM II)

in Garching (Germany). Both institutes produce neutrons sources by fission reaction. The reactor at ILL is an High Flux Reactor (HFR) with a flux of 1.5×10^{15} neutrons per second per cm^2 , with a thermal power of 58.3 MW. The nuclear reactor at ILL is classified as an high flux reactor since it has the highest power world-wide. The nuclear reactor at FRM II produces 10×10^{14} neutrons per second per cm^2 , with a thermal power of 20 MW.

2.5.1 Nuclear reactor

A general nuclear reactor consists in the follow main components:

- the *nuclear reactor core* is the tank that contains the nuclear fuel (typically it is ^{235}U). At ILL, The nuclear fuel consists in 8.57 kg enriched to 93 % of U^{235} .
- the *nuclear moderator* is a medium to cool down the neutron energy created, which are very fast neutrons (20 000 km). At ILL, the nuclear reactor core is surrounded by heavy water at 300 K, which exchanges heat with a water pool. Thermal neutrons are obtained with velocity of 2.2 km s^{-1} . Hot and cold neutrons are obtained using hot and cold source, which means a graphite block of 10 l in volume reaching a temperature of 2000 K and an aluminium sphere filled with 2.5 l of liquid deuterium at 25 K, respectively.
- the *nuclear reactor safety system* collects different safety measures to shut down the reactor and to prevent the production of spore radioactive materials;
- the *control of the fission rate* consists in control rods containing chemical elements, for instance indium, cadmium, etc. Such control rods absorb neutrons without undergoing in a fission reaction. They can be inserted into or removed from the nuclear fuel to monitor the reactor flux.
- *control room* is the key place where the nuclear reactor is monitored and controlled.

	T(K)	v(m/s)	E(meV)	$\lambda(\text{\AA})$	$k(\text{\AA}^{-1})$
hot neutrons	2000	5742	172	0.7	9.12
thermal neutrons	300	2224	26	1.8	3.53
cold neutrons	25	642	0.2	6.2	1.02

Table 2.2: Main physical quantities of the three types of neutrons in the HFR of ILL.

Usually, as at ILL, the instruments are displaced in the *reactor hall* surrounding the nuclear reactor and in *guide hall* next to the reactor. The neutrons produced in the nuclear reactor are then misted in hot, thermal, and cold into guide lines, where the

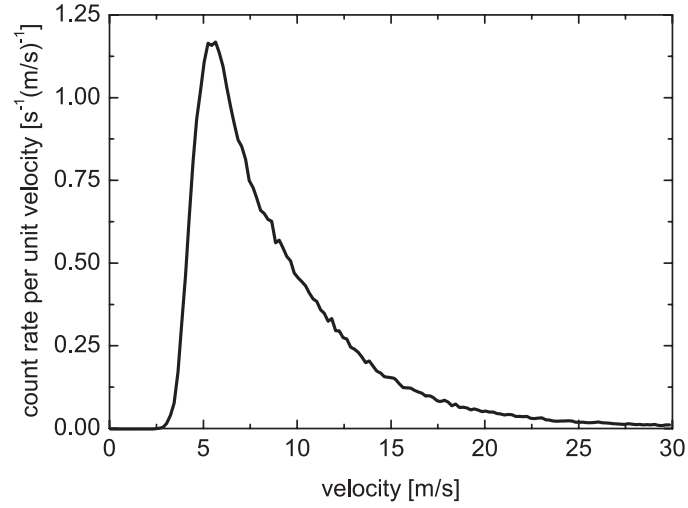


Figure 2.4: Typical neutron velocity distribution [65].

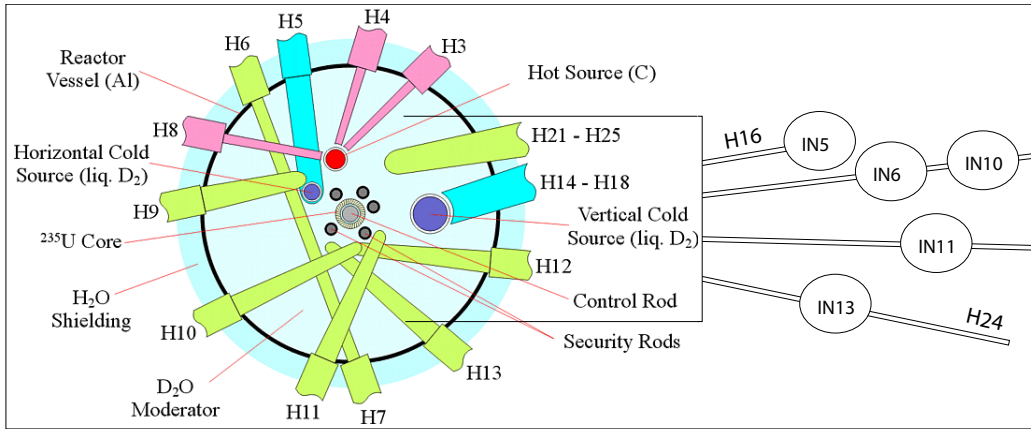


Figure 2.5: Scheme of the High Flux Reactor at ILL. The nuclear reactor produces hot neutrons (fuchsia guide lines), thermal neutrons (green guide lines) and cold neutrons (blue guide lines). The neutrons travel in these guide lines reaching each instruments.

different neutron beams travel and reach each instrument. The guides extend up to 100 meter from the reactor. In the center of Figure 2.5 a scheme of the HFR is represented, i.e. the reactor core with control rods surrounded by security rods (they are associated to nuclear reactor safety system) to shut down the reactor if necessary.

2.6 Instruments

Neutron scattering experiments are performed with a neutron spectrometer. As mentioned, the instrument should measure the double differential cross section defined by the initial and final kinetic energy and the initial and final k-vector associated to the incoming and scattering neutrons, respectively. Therefore, an instrument capable to define such quantities is required. The spectrometers are divided in three kinds, based on the final energy E_f determination:

- *backscattering spectrometer*, where the final energy of scattered neutrons is well defined by *analyser crystals* before to be detected, see Appendix C.0.2;
- *time-of-flight spectrometer*, in which the final energy of scattered neutrons is determined measuring their Time-of-Flight (ToF) to cover the distance L between the target and the detector. In fact, final energy is obtained from $1/2m_n(L/\text{ToF})^2$;
- *spin-echo spectrometer* defines the final energy using the Larmor spin precession.

2.6.1 Time-of-flight spectrometer: IN5

IN5 is a high precision direct geometry Time-of-flight spectrometer. The neutron beam of IN5, as shown in Figure 2.6, travels in a cold guide line H16. The incoming neutrons flux, measured in the target position, is $\sim 6.83 \times 10^5 \text{ ns}^{-1} \text{ cm}^{-2}$ with selected wavelength of 5 \AA .

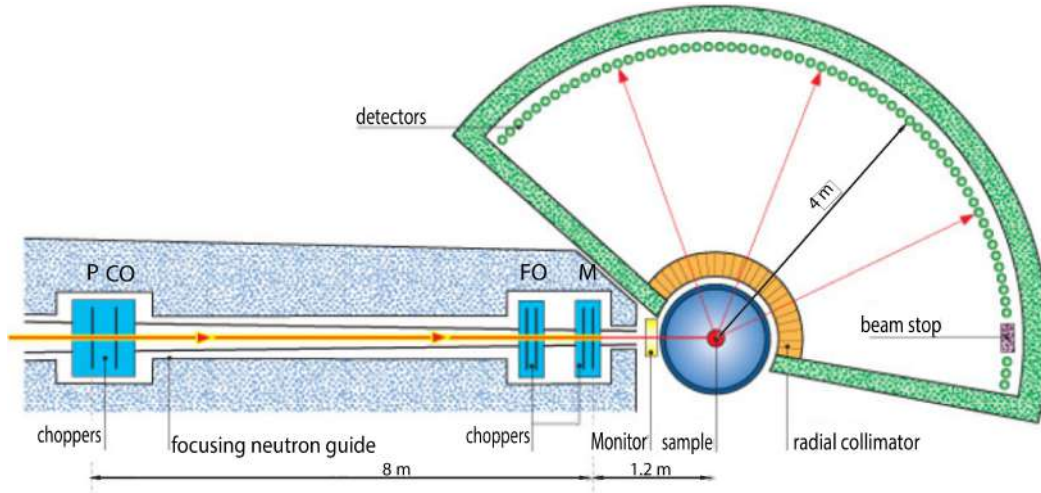


Figure 2.6: Schematic layout of the instrument IN5 at ILL.

This instrument defines the initial energy selecting the initial wavelength through six

rotating disk choppers orthogonal to the incoming neutron beam. Such system of choppers is the primary spectrometer and it works in the follow way:

- the incoming neutron beam, continuous and polychromatic with velocity Maxwell distributed, passes trough two *Pulsing Choppers (P)* that create polychromatic neutrons bursts;
- neutrons bursts pass trough *Contaminant Order Chopper (CO)* that removes those neutrons with wavelength of higher and lower harmonic orders;
- the rest of the neutrons bursts pass trough *frame overlap chopper (FO)* that avoids overlap of neutrons from successive bursts;
- finally, the remaining neutrons bursts pass trough the *Monochromator Choppers (M)*. The chopper (M) has a difference in phase with respect to chopper (P). Thus, it creates neutrons pulse with a single wavelength λ_i , therefore the initial state of reciprocal vector associated to these neutrons can be described by a monochromatic plane wave.

The obtained neutrons pulse, with a initial energy $E_i = h^2/(2m_n\lambda_i)$, passes trough the *monitor* that counts the initial neutrons flux. Finally, it arrives to the sample where the scattering event occurs. The scattered neutrons spread in a distance of 4 m in a given Time-of-Flight window before being collected by the detectors. The final energy is computed, knowing the spread distance and the Time-of-Flight, while the momentum transfer is obtained by displacing the detectors in a spherically curved 3 m high surface. The detectors are the secondary spectrometer made of twelve large units of pixelated PSD with a surface of 30 m² allocated in a vacuum Time-of-Flight chamber. The detectors contain ³He as those in IN13 instrument, see Appendix C.0.2. The characteristics of IN5 are [web1]:

- the incident neutrons flux at the sample is $\sim 6.83 \times 10^5 \text{ ns}^{-1} \text{ cm}^{-2}$ at $\lambda_i = 5 \text{ \AA}$;
- chopper velocity range [2000;17000] rpm;
- changing chopper velocity, λ_i range is $[1.8;20] \text{ \AA}^{-1}$;
- Q_{max} transfer due to $4\pi \sin(\theta/2)/\lambda_i = 11.48/\lambda_i$;
- the energy resolution range is $[1;1 \times 10^3] \text{ \mu eV}$.

2.6.2 Time-of-flight spectrometer: TOFTOF

TOFTOF instrument is a direct geometry disc-chopper time-of-flight spectrometer located in the Neutron Guide Hall West at FRM II. The moderated neutron beam travels

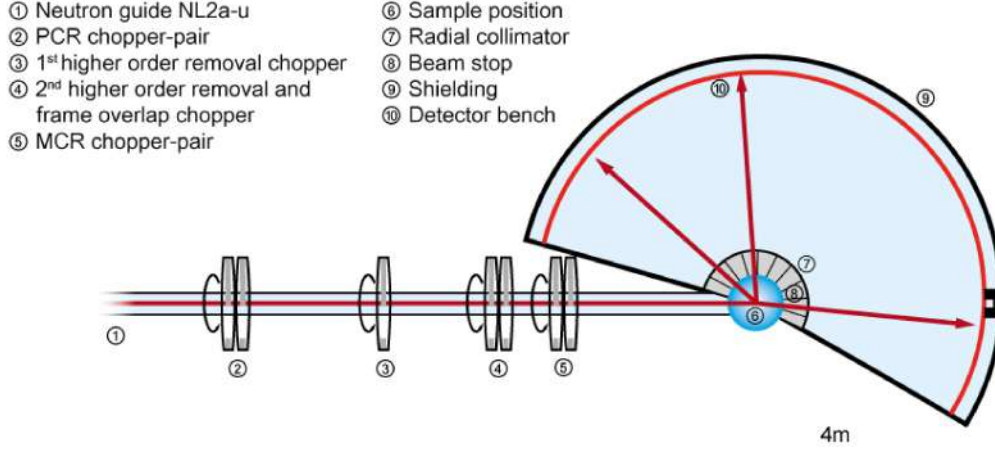


Figure 2.7: Schematic layout of the instrument TOFTOF at FRM II.

in the guide line NL2a-u. The choppers system consists in seven choppers; one more than IN5 instrument. The operating way is similar of that one of IN5 instrument.

The difference is in the frame overlap chopper. In fact, here there are two choppers (not only one) to avoid the overlap from successive neutrons burst. The remaining instrumental set up is similar to IN5, see Subsection 2.6.1. The detector filled with ^3He are mounted at a distance of 4 m and cover a surface of 12 m^2 against the 30 m^2 of IN5. The characteristics of TOFTOF are [web2]:

- the incident neutron flux with $\lambda_i = 5\text{ \AA}$ at the sample is $\sim 1.14 \times 10^5\text{ s}^{-1}\text{ cm}^{-2}$;
- chopper velocity range [400;22000] rpm;
- changing chopper velocity, λ_i range is $[1.4;16]\text{ \AA}^{-1}$;
- Q_{max} transfer is due to $4\pi \sin(\theta/2)/\lambda_i = 11.48/\lambda_i$;
- the energy resolution range is $[2;3 \times 10^3]\mu\text{eV}$.

2.6.3 Time-of-flight spectrometer: IN6

IN6 (actual IN6-sharp having changed from ILL to CRG ownership) is a time focussing Time-of-Flight spectrometer designed for quasi elastic and inelastic scattering for incident wavelengths in a range of between 4 to 6 \AA . The neutron beam of IN6, as shown in Figure 2.8, travels in the cold guide line H15. The incoming neutrons flux, measured at the target position, is $\sim 8.9 \times 10^4\text{ ns}^{-1}\text{ cm}^{-2}$ with selected wavelength of 4.1 \AA . An intense beam is extracted from the H15 guide by a vertically focussing monochromator array,

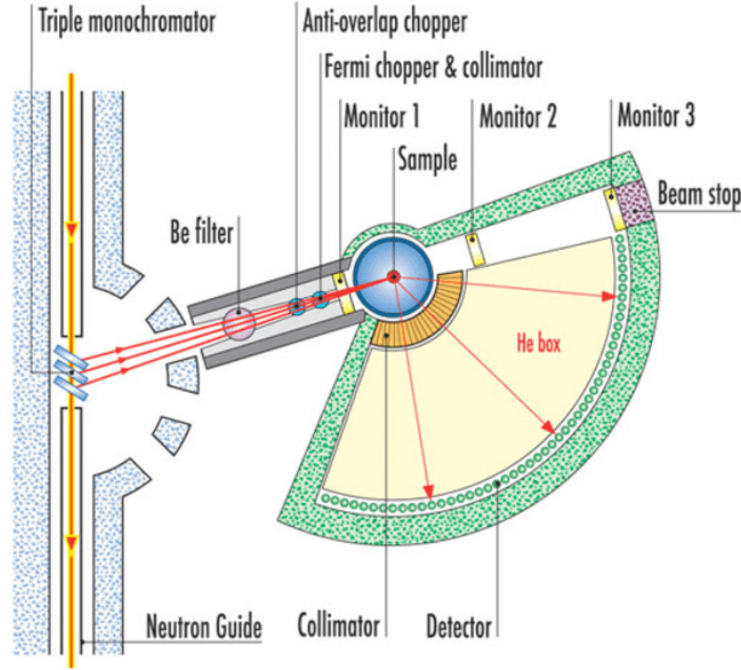


Figure 2.8: Schematic layout of the instrument TOFTOF at FRM II.

(*Triple monochromator*). It consists of three composite pyrolytic graphite monochromators using the full height (20 cm) of the guide and focussing the beam at the sample position. In order to minimize possible interferences due to the presence of the subsequent instruments the monochromator can deliver only four wavelengths: 4.1; 4.6; 5.1; and 5.9 Å. Before that the neutron beam arrives into the target, it passes through:

- the beryllium-filter (*Be filter*) cooled at liquid nitrogen temperature. It has the task to remove the second order reflection coming from the graphite monochromator;
- the *Anti overlap-chopper* that avoids overlap of neutrons from successive bursts;
- the *Fermi chopper & collimator* which has a small slot length to ensure a good transmission. It creates a pulsed beam achieving the time-focusing condition. The time focusing condition occurs when the flight time of neutrons in two different rays for a given distance (L) corresponds to delay Δt of the first-neutron burst with respect to the second one to pass through the Fermi chopper. The normal distance between the Fermi chopper and the target is 38 cm and it rotates at 7500 rpm to avoid frame overlap. On the other hand, the Anti overlap-chopper rotates in the same phase, but at lower speed.

Finally the pulsed beam arrives into the target. The distance between sample and detectors is 2.48 m. Before and after the target the *Monitor 1* and the *Monitor 2* are mounted in order to count incoming and outgoing pulsed beam. The secondary spectrometer consists first of an evacuated sample area. This allows instrumental scientists, if necessary, to remove the external wall of a cryostat or an oven. A helium filled box between the sample and the detectors minimises the background. The sample box is equipped with an oscillating collimator which prevents parasitic reflections (from the cryostat walls for example) reaching the detectors. The detectors are 337 elliptical ^3He detectors covering an angular range between 10° and 115° and, as the other ToF instruments, are mounted on a spherically curved surface.

The characteristics of IN6 are [web3]:

- the incident neutron flux with $\lambda_i = 4.1 \text{ \AA}$ at the sample is $\sim 8.9 \cdot 10^4 \text{ s}^{-1} \text{ cm}^{-2}$;
- Fermi chopper velocity range [3000;15000] rmp;
- four initial wavelengths λ_i : 4.1, 4.6, 5.1 and 5.9 \AA which correspond to the following energy resolutions 170, 120, 70, 50 \mu eV ;
- Q_{max} transfer of 2.6 \AA^{-1} .

Chapter 3

NS experiment and data analysis

3.1 Typical NS experiment

Before a NS experiment there is the sample preparation step discussed in the next chapters concerning the different kind of investigated samples. Once each samples are prepared they are allocated directly in the *sample holder* if the sample state is liquid or within an aluminium foil, if the sample state is solid/paste. The aluminium foil preserves the hydration of the sample after the experiment during weighting operation. The sample holder is made in aluminium and is a flat container with a surface of $3 \times 4 \text{ cm}^2$. It consists in two parts, a bottom part where is allocated the sample and a top part to close it. The bottom part contains a tread, as shown in panel (a) of Figure 3.1, where the indium is displaced in order to assure the hermetic closure of the sample holder in order to not lose sample during the experiment. The thickness of the top of the sample holder, as shown in panel (b) of Figure 3.1, defines the accessible volume for the sample ($1.2 \div 3.6 \text{ cm}^3$, i.e. $1.2 \div 3.6 \text{ mL}$).

Once the sample holder is filled of sample then it is closed by screws and bolts. The sample holder is covered with a cadmium mask, which has null incoherent cross section and a very high absorption cross section ¹. The mask presents a window corresponding to sample surface in order to focus the neutron beam only into the target and to absorb those neutrons that are out such window. After that, the sample holder is mounted on a long *stick*. In order to orientate the sample with respect a point of reference, the stick is furnished of laser point which is parallel or orthogonal to the top part of the sample holder. Finally, the sample fixed to the stick is mounted in the cryofurnace that permit to monitor the temperature of the sample. The presence of the cadmium mask creates a shadow visible in the scattering intensity. The best condition is to orientate the sample a 135° with respect to the incoming beam in order to have the signal affected by the shadow target only at high angle/Q-value, where the scattering intensity, which decay exponentially

¹ An atom of Cd has an absorption cross section of 3122 barns.

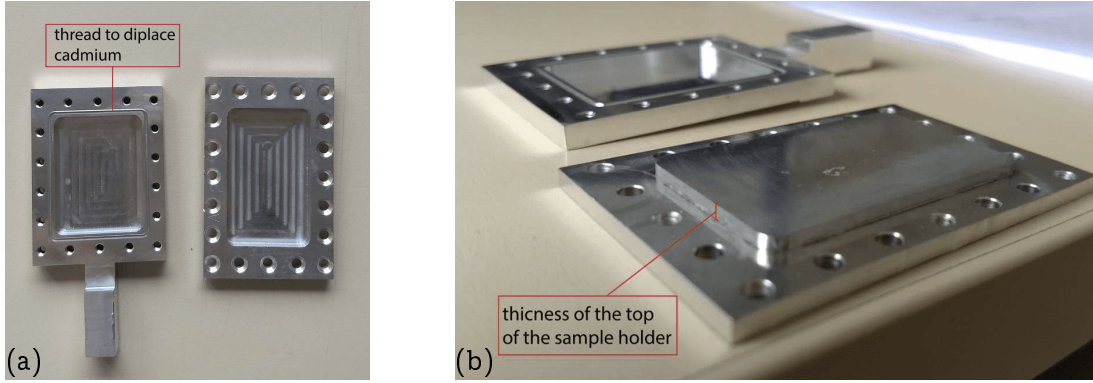


Figure 3.1: Flat sample holder pictures. Panel (a) shows top view picture of the sample holder. From left to right is shown the bottom and the top part of the sample holder. Panel (b) shows a picture in which the bottom part is reverse to show a typical geometry of such sample holder.

in Q^2 , is low. The sample T variation is guaranteed through exchange gas (helium) in the cryofurnace. When the sample is well mounted the neutron beam is opened. From the *instrument workstation*, the experiment is monitored using *Nomad* software, which allows to define the experimental conditions such as choppers speed, nominal wavelength, temperature range and acquisition time. The instrumental resolution $\mathcal{R}(Q, \omega')$ is measured using vanadium sample reference (for our experiments the size of which was of $3 \times 4 \times 0.15 \text{ cm}^3$). The vanadium is a suitable reference for quasi-elastic incoherent neutron scattering due to the fact that his coherent cross section is almost zero.

In our QENS investigation the temperature was kept at 300 K and we recorded QENS data at high energy resolution, i.e. $FH\text{MW} \sim 10 \text{ } \mu\text{eV}$ that corresponds a time window of 70 ps and at low energy resolution, i.e. $FH\text{MW} \sim 70 \text{ } \mu\text{eV}$ that corresponds a time window of 10 ps.

3.2 NS data treatment

Nomad collects the rawdata in different file extensions depending on the instrument. For instance, Nomad collects the rawdata on IN5 in NeXus format with extension *.nxs*. NeXus is a common data format for neutron, X-ray, and muon science. The data manipulations are obtained using Large Array Manipulation Program (LAMP) software developed by computing group at ILL [66] [67]. It is a software based on Interactive Data Language (IDL). If the raw data are NeXus format the first manipulation is to convert nexsus file into Hierarchical Data Format (HDF) in order to correctly visualise the data. HDF is a set of file formats (*.hdf*, *.h4*, *.hdf4*, *.he2*, *.h5*, *.hdf5*, *.he5*) developed to store and organize large amounts of data. Different specific macros are developed for data correction coming from the different instruments present at ILL and from some other facility (at about 46

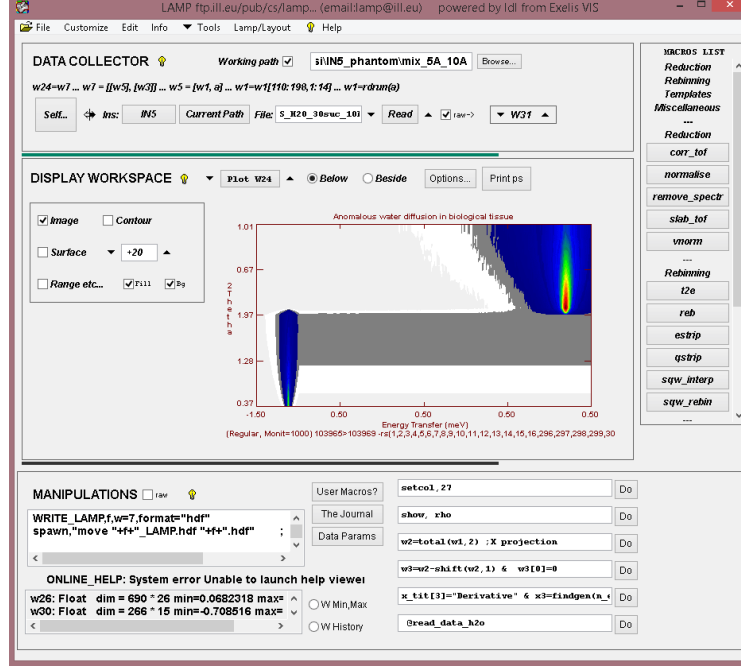


Figure 3.2: Large Array Manipulation Program (LAMP) screenshot. Software developed by computing group at ILL in order to manipulate big data from neutron scattering experiments.

instrument).

3.2.1 QENS data correction

The macro written to correct QENS rawdata consists mainly in:

- 1) to read the quasi elastic signal from sample, vanadium and empty cells normalized to the monitor 1, corrected to the absorption factor and the detector efficiency. The quasi elastic empty signal is removed from the vanadium and the sample signal. The latter is after normalized to the corrected vanadium, which is the reference sample having a coherent signal almost zero.
- 2) To transform and to bin the energy detector channels, placed in x -axis, in the energy transfer scale and to transform the angle detector channels grouped in 15 angle-values, placed in y -axis, in the momentum transfer scale using Equation 2.6.

The energy detector channels are 1024 and 1020 for IN5 and TOFTOF instrument, respectively. The angle detector channels are 729 and 890 for IN5 and TOFTOF instrument, respectively. In step 2) we assume that Eq. 2.6 is a still valid approximation to transform angle into momentum transfer in the investigated energy transfer.

In Figure 3.3a a typical scattering intensity as a function of the energy detector channels at 90° is shown. The sample, the vanadium and the empty cell are in blue, black and red lines points, respectively. In Figure 3.3b a zoom of Figure 3.3a between 620 and 650 energy detector channels is shown. Figure 3.3c shows a typical normalised scattering in-

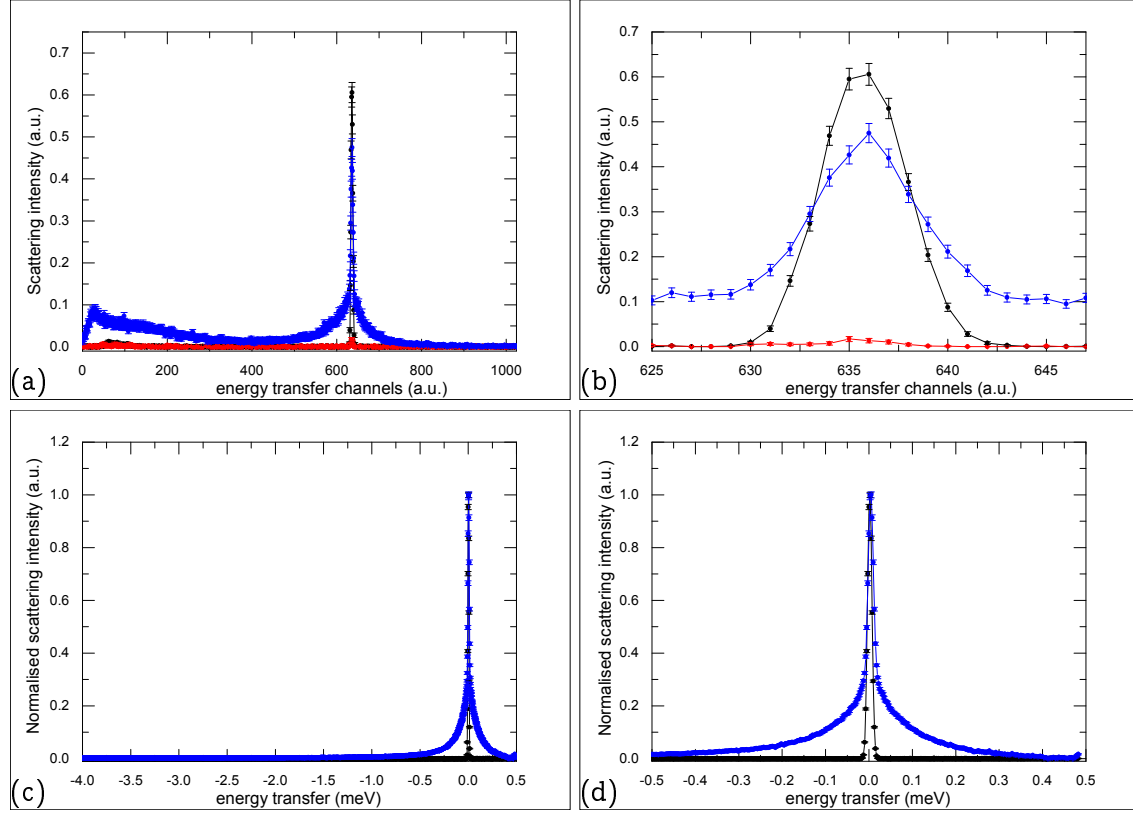


Figure 3.3: Typical data from IN5 instrument at $10 \mu\text{eV}$ energy resolution. Panel (a) shows a rawdata at 90° as a function of the 1024 energy detector channels. Panel (b) shows a zoom of panel (a). Panel (c) shows the normalised scattering intensity as a function of the energy transfer at the corresponding Q value $\sim 0.91 \text{ \AA}^{-1}$. Panel (d) shows a zoom of panel (b). Black line points ($-\bullet-$) are vanadium, blue line points ($-\bullet-$) are the sample and red line points ($-\bullet-$) are empty cell.

tensity as a function of the energy transfer at the corresponding Q value $\sim 0.91 \text{ \AA}^{-1}$. The sample and the vanadium are in blue and black line points, respectively. This spectrum is obtained after data correction. Figure 3.3d shows a zoom of Figure 3.3c between -0.5 and 0.5 meV . The shown spectrum example is obtained from IN5 data at $10 \mu\text{eV}$ energy resolution. For each energy resolution after data correction we obtain 15 spectra corresponding at 15 Q -values from 0.1 to 1.01 and from 0.2 and 2.02 \AA^{-1} with respect to high and low energy resolution. The obtained spectra at low and high energy resolution are saved into

two different workspaces. In order to implement the data analysis, such workspaces are merged in one using a specific macro. The data merging from two different resolutions is fundamental strategy towards the extraction of the physical results.

3.3 QENS data analysis

3.3.1 A theoretical model to analyse QENS data from biological samples

The QENS signal measured in our systems is essentially incoherent and arises essentially from the hydrogen atoms usually present in great abundance in biological samples. This is due to the incoherent cross section of hydrogen that is much larger than the coherent one and also much larger than the cross sections (both coherent and incoherent) of the other atoms present in the sample (see Table 2.1 at page 16). We also recall that, due to the instrumental resolution, the time window explored in our experiments is between 10 and 70 ps and that only motions in the above time scale can be observed. Therefore, in the QENS spectra measured in our complex systems, we can distinguish four contributions arising from four kinds of hydrogen motions:

- *fixed hydrogens*: these are hydrogens atoms whose dynamics is very slow with respect to the time/energy window resolution investigated and that, therefore appear as fixed and give rise to a purely elastic contribution. This elastic contribution is well described by a Dirac- δ function $\delta(\omega'(\vec{Q}))$ with a given population f .
- *slow hydrogens*: a quasi-elastic contribution arises from hydrogens of *slow water* the dynamics of which is one order of magnitude smaller with respect bulk water. As mentioned in the Subsection 2.4.1, a neutron scattering signal from molecules that translate and rotate at the same time are described by a scattering function, $S_{T,R}^{slow}(\vec{Q}, \omega'(Q))$, which is the convolution of two scattering functions, $S_T^{slow}(\vec{Q}, \omega'(Q))$ and $S_R^{slow}(Q, \omega'(Q))$. In this case, $S_T^{slow}(Q, \omega'(Q))$ and $S_R^{slow}(Q, \omega'(Q))$ describe translation and rotational motions of slow water component, respectively. Jump diffusion model and continuous rotational on a circle model are used to describe translational and rotational components, see page 18 and 19. The extracted physical parameters are translational diffusion coefficient D_T^{slow} expressed in $\text{cm}^2 \text{s}^{-1}$, the residence time τ_r^{slow} expressed in ps and rotational diffusion coefficient D_R^{slow} expressed in ps^{-1} . The contribution of slow water component to the total signal is given by the fraction p_1 .
- *fast hydrogens*: a quasi-elastic contribution arises from hydrogens of *fast water* the dynamics of which is similar to bulk water. Such neutron scattering function is described similarly to the slow one. The extracted physical parameters are translational diffusion coefficient D_T^{fast} , the residence time τ_r^{fast} and rotational diffusion coefficient

D_R^{fast} . The contribution of fast water component to the total signal is given by the fraction p_2 .

- *very fast hydrogens*: a quasi-elastic contribution arises from hydrogens of *methylene groups* (CH_2 groups) constituting macromolecules, proteins, membranes etc; which are exposed to interact with interfacial water molecules. Such CH_2 groups perform low-frequency librational motions at room temperature. These librational motions occur in times lower of 100 ps and are associated to torsional isomerization from *gauche*-to-*trans* conformations of the CH_2 groups as shown in [68, 69, 70], therefore are detectable. A simple Lorentzian function with Q -independent width Γ_{CH_2} expressed in meV can describe such jump rotational motions [48]. The contribution of CH_2 groups component to the total signal is given by the fraction $p_3 = 1 - (f + p_1 + p_2)$. The reason of that is to normalise the total signal to one.

In total the independent parameters in Q named *global parameters* are ten: three fraction populations f , p_1 and p_2 ; two translational diffusion coefficients D_T^{slow} and D_T^{fast} ; two residence times τ_r^{slow} and τ_r^{fast} ; two rotational diffusion coefficients D_R^{slow} and D_R^{fast} ; one lorentzian width Γ_{CH_2} . The center of such four scattering functions is the same for all of them and placed at $\omega'(Q) = \omega - \omega_0(Q)$. The four components are convoluted with the resolution $\mathcal{R}(\omega')$ and normalise with a factor $A(Q)$. A background $BK(Q)$ is added to take into account background still present after data correction due to inelastic signal. Such background could be flat, linear or quadratic, therefore it contains a number of parameters between one and three. The measured spectra are the scattered intensities from the sample as a function of energy transfer and the momentum transfer. In order to improve the signal-noise ratio and to properly perform the fitting procedure in the data correction step the signal was grouped in n_{binE} bins and n_{binQ} bins for $\hbar\omega$ and Q axes, respectively. In particular we will obtain a number of spectra in Q axis equal to $n_{binQ} + 1$, coherently to the binning procedure. The depending parameters in Q named, *local parameters*, are the center spectra $\omega'(Q)$, the normalise factor $A(Q)$ and the background $BK(Q)$. In order to obtain the total number of local parameters we have to multiply such parameters for $n_{binQ} + 1$ value.

Finally, the proposed theoretical model to analyse our data is the following [46]:

$$\begin{aligned}
 S_{inc}(Q, \omega') = A(Q) \mathcal{R}(Q, \omega') \otimes [& f \delta(\omega') + \\
 & + p_1 S_{T,R}^{slow}(Q, \omega') + \\
 & + p_2 S_{T,R}^{fast}(Q, \omega') + \\
 & + p_3 S_{CH_2}(Q, \omega')] + BK(Q)
 \end{aligned} \tag{3.1}$$

In the model we suppose that the Debye-Waller factor is included in the normalise factor $A(Q)$. In Figure 3.4 a typically spectrum at $Q = 0.36 \text{ \AA}^{-1}$ is shown with the fitted curve and the representation of the four contributions.

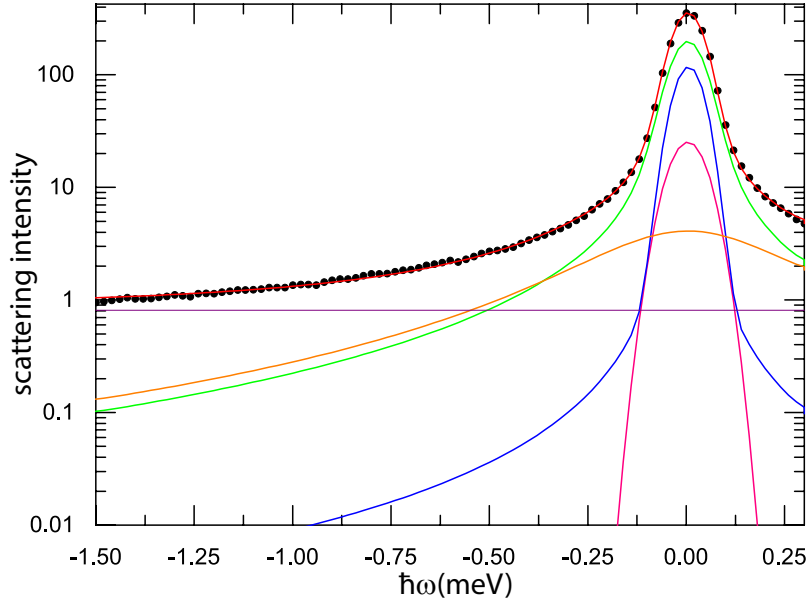


Figure 3.4: QENS spectrum of yeast cells taken at 0.36 \AA^{-1} at low energy resolution on IN5. Black points are the experimental data and the red line the total fit obtained using Equation 3.1. The various spectral contributions are represented by the lines in color. Fuchsia: elastic contribution arising from “fixed” hydrogens; green: roto-translation contribution arising from “fast” water population; blue: roto-translation component arising from “slow” water population; orange: CH_2 groups contribution; violet: background.

3.3.2 QENS data fitting procedure

30 spectra at high and low energy resolutions are obtained from data manipulation. Spectra with Q-value lower than 0.3 \AA^{-1} were not included as observed in diffraction patterns of myelin rich brain tissues (such as optic nerves) where bragg reflections were univocally attributed to characteristic thickness of myelin layers (data not shown). For a proper comparison of results from different systems only spectra with Q-values higher of 0.3 \AA^{-1} are analysed in experiments presented in the Chapter 4, 5 and 6. Figure 3.5 shows a typical QENS spectra at high and low energy resolution from IN5 experiment in 3D view ((a) and (c) panels) and their contour plot ((b) and (d) panels). In particular yeast sample is shown. The 25/26 spectra from TOFTOF/IN5 are fitted at the same time with the theoretical model expressed by Equation 3.1. In order to fit simultaneously data from two different energy resolutions we used STRfit tools in LAMP developed by the computing group of ILL which allows to implement the multi-fit. Two different minimization routines based on the Levenberg-Marquardt method [71] can be used: CoolFit and MpFit

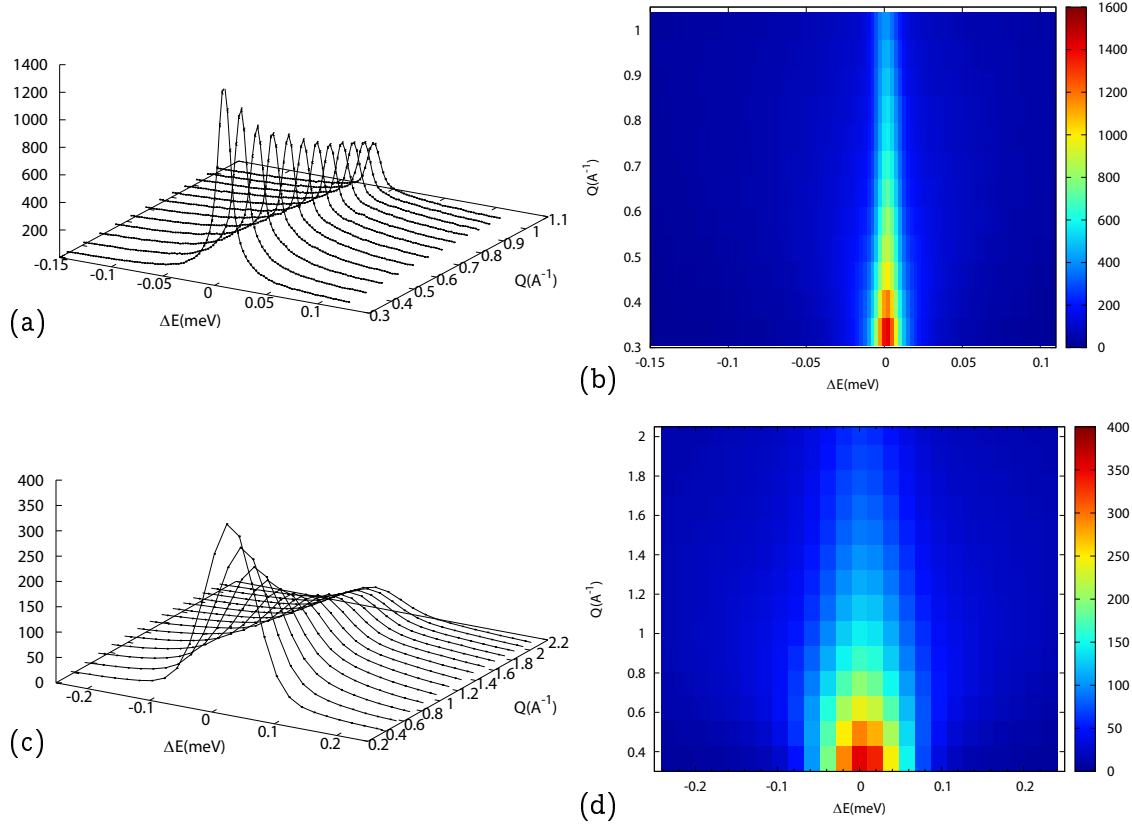


Figure 3.5: QENS spectra of yeast sample at low and high energy resolution from IN5 experiment in 3D view and contour plot. Panels (a) and (c) show 12 and 14 spectra as a function of energy transfer and momentum transfer at high and low energy resolutions, respectively. Panels (b) and (d) are the contour plots of panels (a) and (c).

engines [web4]. Such routines give the same results after fitting process, see Appendix B.2. The difference consists in how they rich the minimum χ^2 , to which corresponds the best set of parameters that describe the experimental data. Essentially such routines use different paths. In particular, MpFit seems faster than CoolFit engine. From *Model* menu one can enter his own model. In fact, a list of different theoretical models are implemented on STRfit. In figure 3.6 a screenshot of STRfit tools with *User defined fitting model* window is shown. Such window permits to monitor the initial parameters. The errors associated to the parameters are the diagonal covariance matrix values [72], nevertheless the *confidence limit* investigation is implemented to define the associated errors to our parameters.

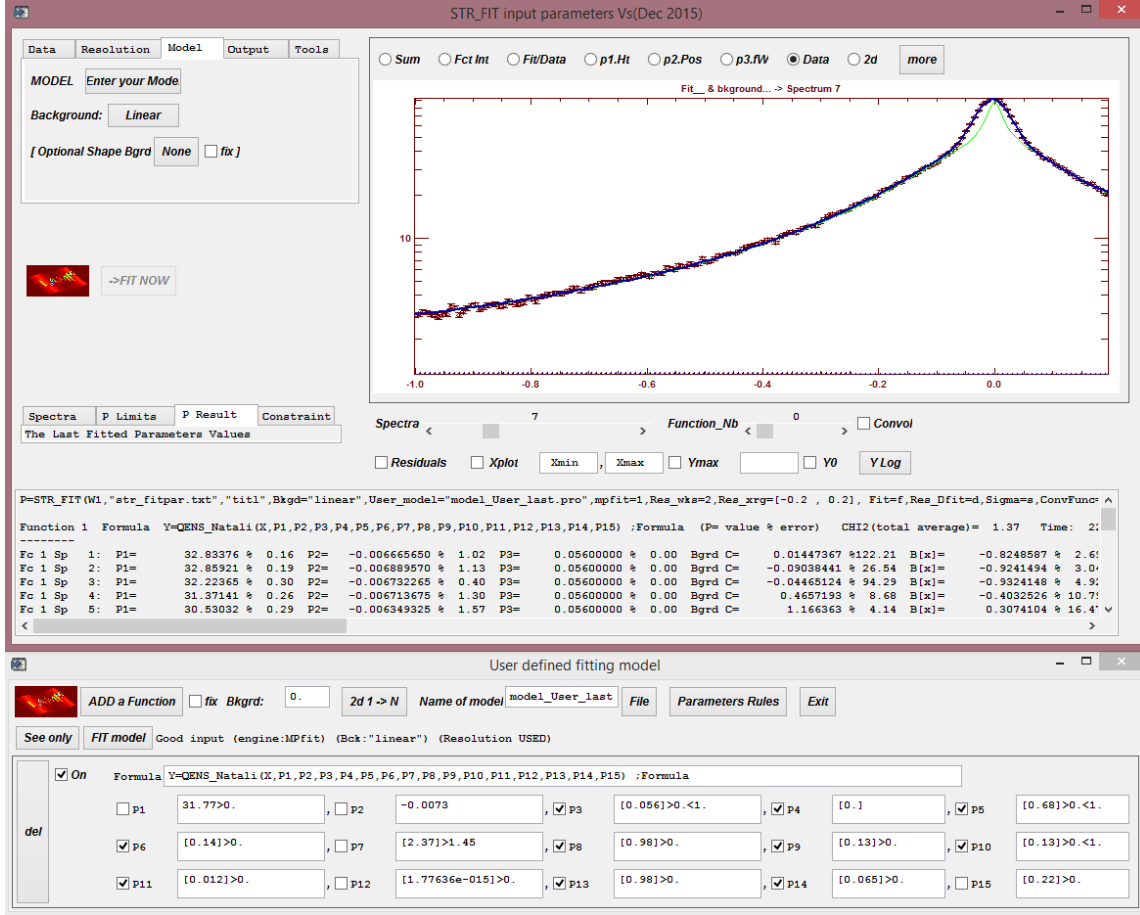


Figure 3.6: STRfit screenshot. Tool of LAMP to implement multi fit using different listed o user theoretical models.

3.3.3 Confidence limit investigation

Given N datapoints y_i with $i = 1, \dots, N$ and a theoretical model $y(x|\vec{a})$ with a non linear dependency of the parameters vector $\vec{a} = (a_1, \dots, a_M)$, the χ^2 function is defined as

$$\chi^2(\vec{a}) = \sum_{i=1}^N \left[\frac{y_i - y(x|\vec{a})}{\sigma_i} \right]^2, \quad (3.2)$$

where σ_i are the data points errors. A $\chi^2(\vec{a}) \sim N$ means that the fit procedure turns back a good set of parameters \vec{a} . The reduced $\chi^2_{red}(\vec{a})$ is defined as the ratio between the $\chi^2(\vec{a})$ and $N - M$. For $N \gg M \Rightarrow \chi^2_{red}(\vec{a}) \sim 1$, therefore a good fit turns back a $\chi^2_{red}(\vec{a}) \sim 1$. As mention at pag. 35, to quantitatively estimate the uncertainties of such M parameters we

propose in this work the confidence limit method [73]. Let us start with some assumptions:

- we assume that a true set of parameters \vec{a}_{true} minimizes the data set $\mathcal{D}_{(0)}$.
- we assume that after an experiment the true set of parameters \vec{a}_{true} is realized by $\vec{a}_{(0)}$ fitting the measured data set $\mathcal{D}_{(0)}$, where $\chi^2(a_{(0)}) = \chi^2_{min}$.
- A statistical errors is associated to the measured data set $\mathcal{D}_{(0)}$, which is therefore not unique. In fact, if the experiment is repeated in the same conditions several times; the measured data set $\mathcal{D}_{(1)}, \mathcal{D}_{(2)}, \dots$ will be obtained and it will be fitted with a set of parameters $\vec{a}_{(1)}, \vec{a}_{(2)}, \dots$. These true sets of parameters $\vec{a}_{(i)}$ occur with a certain probability distribution in the parameters space of dimension M.

The aim is to find the probability distribution of $\vec{a}_{(i)} - \vec{a}_{(true)}$ without knowing the ideal true set of parameters $\vec{a}_{(true)}$. One of the possible way is the *confidence limit method*. A confidence region/interval can be estimated in the parameters space, such that it is possible to define the probability to obtain a set of parameters within the confident region/interval repeating the experiment once again. $\chi^2(\vec{a})$ is a function defined in the M-dimensional parameters space with M degree of freedom.

$\nu \setminus \mathcal{P}$	1%	2.5%	5%	10%	90%	95%	97.5%	99%
1	—	0.001	0.004	0.016	2.706	3.841	5.024	6.635
2	0.02	0.051	0.103	0.211	4.605	5.991	7.378	9.210
3	0.115	0.216	0.352	0.584	6.251	7.815	9.348	11.345
4	0.297	0.484	0.711	1.064	7.779	9.488	11.143	13.277
5	0.554	0.831	1.145	1.610	9.236	11.071	12.833	15.086
6	0.872	1.237	1.635	2.204	10.645	12.592	14.449	16.812
7	1.239	1.690	2.167	2.833	12.017	14.067	16.013	18.475
8	1.646	2.180	2.733	3.490	13.362	15.507	17.353	20.090
9	2.088	2.700	3.325	4.168	14.684	16.919	19.023	21.666
10	2.558	3.247	3.940	4.865	15.987	18.307	20.483	23.209
11	3.053	3.816	4.575	5.578	17.275	19.675	21.920	24.725
12	3.571	4.404	5.226	6.304	18.549	21.206	23.337	26.217
13	4.107	5.009	5.892	7.042	19.812	22.362	24.736	27.688
14	4.660	5.629	6.571	7.790	21.064	23.685	26.119	29.141
15	5.229	6.262	7.261	8.547	22.307	24.996	27.488	30.578

Table 3.1: Confidence level of $\Delta\chi^2$ with ν degree of freedom in the M-dimensional space.

The confidence limit method explores $\chi^2(\vec{a})$ varying \vec{a} in a region around the best set of parameters $\vec{a}_{(0)}$ of the experimental data set $\mathcal{D}_{(0)}$ where χ^2 function assumes χ^2_{min} value. To an increment of $\Delta\vec{a} = \vec{a} - \vec{a}_{(0)}$ corresponds a positive increment of $\Delta\chi^2 = \chi^2(\vec{a}) - \chi^2_{min}$.

$\Delta\chi^2$ depends on the degrees of freedom and it defines the desired confidence region, see Table 3.1. For example for $M=1$ the 90% of confidence interval associated at a_0 parameters occurs when $\Delta\chi^2 = 2.706$.

Let us consider a particular case in which we have M parameters, but we want to focus the confidence limit investigation only in ν parameters, with $\nu < M$. Such ν parameters are held fixed, while the remaining parameters are varied to minimize χ^2 that is defined in a ν -dimensional subspace of the M -dimensional parameters space.

For example, in QENS experiment on IN5 we have 26 spectra: $12 \times 650 = 7800$ N_1 data points for high energy resolution and $14 \times 91 = 1274$ N_2 data points for low energy resolution, for a total of 9074 N data points. In case of a constant background there are $26 \times 3 = 78$ local parameters and 10 global parameters, as mentioned at page 33. Applying the confidence limit method, we have that in our case $M=88$ and $\nu = 10$, since we are interested in defining a confidence interval only for global parameters. We will study $\Delta\chi^2_{\nu=10}$ as a function of the global parameters; the local parameters are varied to minimize the $\Delta\chi^2_{\nu=10}$ function. Referring to Table 3.1, to obtain a confidence interval with 99% of confidence it is required a $\Delta\chi^2_{\nu=10}(a_i) = 23.209$ with $i=1,\dots,10$. It remind that the global parameters are the physical parameters in the theoretical model expressed by Equation 3.1. The choice to apply the fit to data from two energy resolutions reflects a big increment on the numbers of points to fit. As a consequence of this, the number of the set of solutions is drastically reduced giving stability and major readability to the best solution obtained at the best minimum of χ^2 function and hence giving major readability to the theoretical model.

Chapter 4

Water in phantom systems

4.1 Introduction

Sucrose ($C_{12}H_{22}O_{11}$) is a disaccharide molecule with molar mass of 342.30 g mol whose structure is highlighted in Figure 4.1.

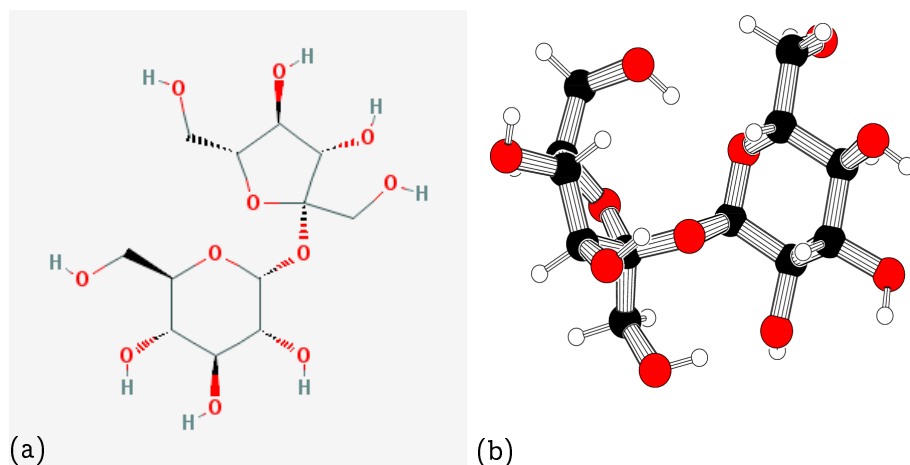


Figure 4.1: Panel (a) 2d view of sucrose representation. Panel (b) 3d view of sucrose representation.

In this chapter we use sucrose in aqueous solutions in order to study water dynamics in a simple model system where we expect to have two populations of water molecules: a “slow” one in the hydration shell of sucrose and whose dynamics is slowed down by the strong interaction with the solute, and a “fast” one composed of water molecules outside the hydration shell, not strongly interacting with solute and therefore similar to bulk water. Moreover, since one sucrose contains three CH_2 groups, we expect to detect a QENS signal related to their dynamics. QENS experiments are performed with the spectrometer IN6 at

300 K with sucrose concentrations of 10, 20 and 30% (mass percentage¹) corresponding to about 171, 77 and 44 water molecules per sugar molecule and results are compared with those relative to bulk water. For the sample we use the following abbreviations: $10SH_2O$, $20SH_2O$ and $30SH_2O$ for sucrose concentrations of 10, 20 and 30%, respectively.

Samples preparation was obtained using standard sucrose ($\alpha - D - Glc - (1 \rightarrow 2) - \beta - D - Fru$) in Milli-Q water ($18 M\Omega cm$ purity). The accessible volume for the sample was of 240 mL, due to thickness of 0.2 mm left free by the top of the chosen sample holder. Sucrose solutions in water solvent represent the easiest “phantom” systems in which hydrogens dynamics can be investigated using QENS techniques and the obtained QENS data can be fitted with the proposed theoretical model in Equation 3.1.

4.2 Results

4.2.1 Pure water

A QENS experiment on pure water was carried out using the spectrometer IN6. This measurement has been done in the 2011 during the experiment number *TEST*–2054, which results is cited in [46]. I thank the authors for allowing me to analyze their data using the approach described in Chapter 3, Section 3.2.1. QENS spectra were obtained with an energy resolution of $FWHM \sim 70 \mu eV$ (time observed 10 ps). High energy resolutions are not accessible with this instrument, see Subsection 2.6.3. After rawdata correction, which

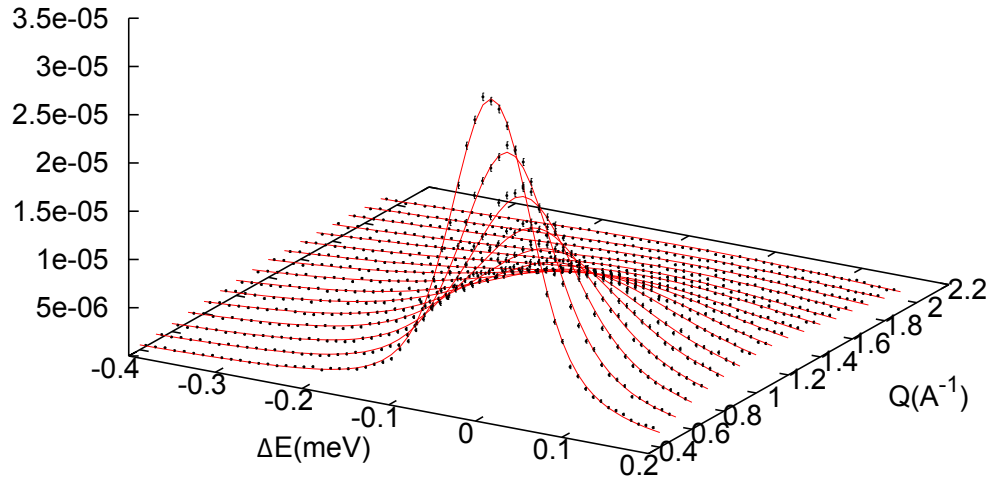


Figure 4.2: QENS spectra of H_2O taken at $90 \mu eV$ energy resolution on IN6. Black points (\bullet) are the experimental data and the red lines ($-$) the fitting curves.

¹Mass percentage is the percentage of mass fraction, i.e. $\frac{m_{solute}}{m_{solute} + m_{solvent}} \%$.

was similar to that implemented for IN5 rawdata (see Chapter 3), the selected Q-range for global fit procedure was between 0.4 and 1.9 \AA^{-1} . Spectra at 17 different Q-values were globally fitted in terms of Equation 3.1; the fitting, parameters f , p_1 and p_3 were imposed to be zero. Therefore, for bulk water Equation 3.1 assumes the following form, in which only translational and rotational diffusion of bulk water is considered.

$$S_{inc}(Q, \omega') = A(Q)\mathcal{R}(Q, \omega') \otimes S_{T,R}^{\text{bulk water}}(Q, \omega') + BK(Q) \quad (4.1)$$

In Figure 4.2 QENS spectra of pure water with relative fit curves are shown. The model well describes pure water spectra with a reduced χ^2 value of 1.32. Table 4.1 shows parameters

	Pure water	
	value	error
$D_T^{\text{bulk water}} [\text{cm}^2/\text{s}]$	2.60E-05	4E-07
$\tau_r^{\text{bulk water}} [\text{ps}]$	0.90	0.05
$D_R^{\text{bulk water}} [1/\text{ps}]$	0.20	0.02
χ_{red}^2	1.32	

Table 4.1: Parameters values obtained from the global fits for pure water measured on IN6.

for pure water dynamics at 300 K obtained on IN6, which are in agreement with those reported in literature listed in Table 1.1.

4.2.2 Water dynamics in aqueous solution of sucrose

QENS experiments on sucrose aqueous solutions at various concentrations were carried out using the spectrometer IN5. Those measurements were realized in the 2013 during the experiment number 8 – 05 – 416. My personal contribution to this work was to analyze the data. Spectra were acquired at low and high energy resolutions, $FWHM \sim 10 \text{ } \mu\text{eV}$ (corresponding to a time resolution $\sim 70 \text{ ps}$ and Q-range between 0.11 and 1.01 \AA^{-1}), and $FWHM \sim 70 \text{ } \mu\text{eV}$ (corresponding to a time resolution $\sim 10 \text{ ps}$ and Q-range between 0.22 and 2.02 \AA^{-1}). The transmission of the total signal was of 91%, 92% and 89% for $10SH_2O$, $20SH_2O$ and $30SH_2O$, respectively. This means that multiply scattering effect can be neglected during data correction [60]. We analyzed 26 spectra using global fittings strategy: 12 and 14 curves for high and low energy resolution configurations, respectively. A preliminary semi-quantitative analysis can be performed by looking at the QENS intensities summed over all Q-range investigated, and normalized. This is reported in figure 4.3 for the data at high (panel (a)) and low (panel (b)) energy resolutions. The expected behavior is observed in Figure 4.3, i.e., the width decreases with increasing sucrose concentration, indicating an overall slowing down of hydrogen dynamics in the samples. Detailed quantitative information is obtained with our global fittings strategy. Experimental data are

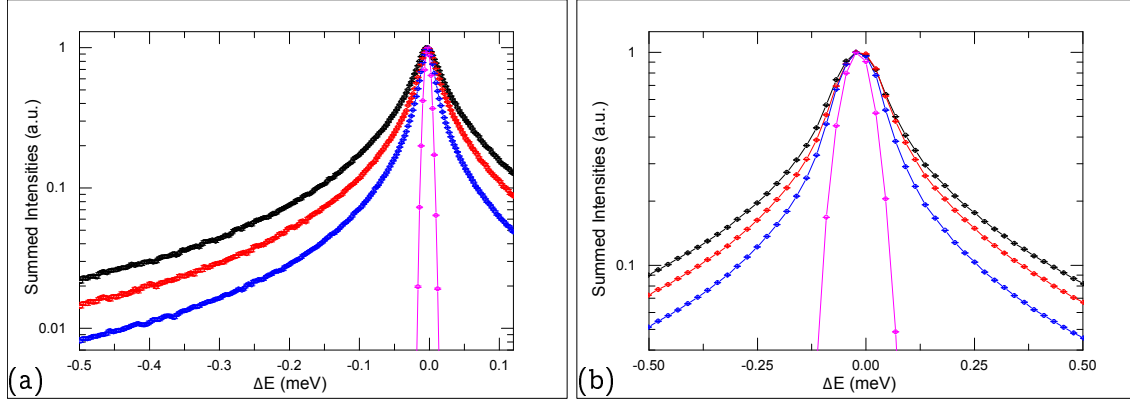


Figure 4.3: Panels (a) and (b): Summed intensities over all Q range of QENS spectra taken at 10 and 70 μeV energy resolutions, respectively. Black points ($-\bullet-$) are H_2O with 10% of sucrose, red point ($-\bullet-$) are H_2O with 20% of sucrose, blue points ($-\bullet-$) are H_2O with 30% of sucrose and fuchsia opened circle ($-\circ-$) is the vanadium. The percentage of sucrose is calculated over the total solution weigh.

reported in Figure 4.4, together with fittings in terms of Equation. 3.1. Excellent fittings are obtained and reduced χ^2_{red} values obtained are 0.88, 0.92 and 1.66 for 10 SH_2O , 20 SH_2O and 30 SH_2O , respectively.

Table 4.2 shows global physical parameters obtained from the fitting procedure. A few comments are in order:

- almost vanishing f values are obtained; this is expected since no “immobile” hydrogens are present in pure water or in water-sucrose solutions;
- two populations of water hydrogens - a “fast” one and “slow” one - are present in water-sucrose solutions; their dynamics properties will be discussed in the next paragraph;
- a population of hydrogens CH_2 groups is present in water-sucrose solutions. This is expected since sucrose contains three CH_2 groups; consistently, parameter p_3 (related to the fraction of hydrogens belonging to CH_2 groups) is of the order of a few percents and increases with increasing sucrose concentration. Interestingly, a lower value of parameter Γ_{CH_2} (i.e. the width of the CH_2 contribution) is observed at 30% sucrose concentration; this suggests a slowing down of CH_2 groups dynamics likely related to onset of water mediated solute-solute interactions.

Quantitative analysis of water dynamics in sucrose solutions What physical parameters extracted from the global fit tell us is that 10% of sucrose concentration in aqueous solution is enough to perturb water dynamics and to create two populations of water, a first one that has still dynamics properties of bulk water, the so-called “fast water” and a second

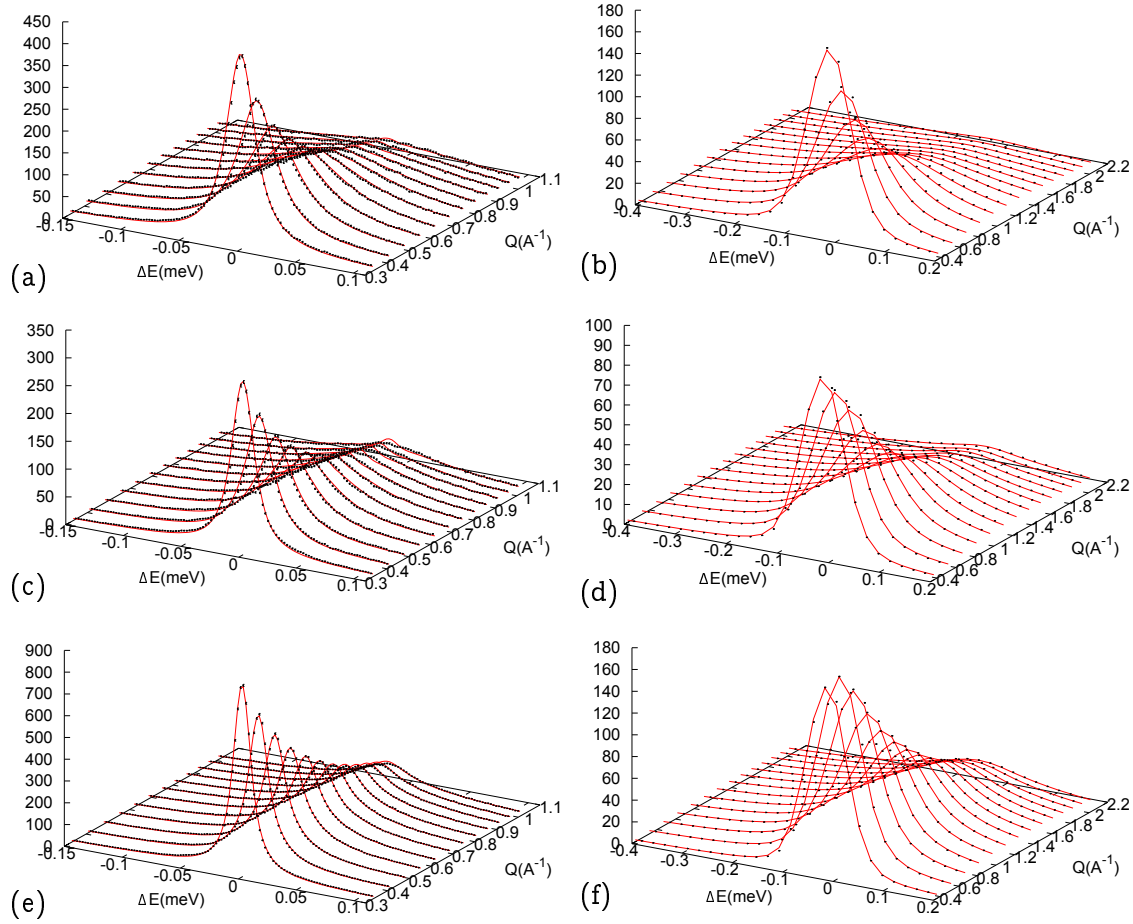


Figure 4.4: Left panels: QENS spectra taken 10 μeV energy resolution; (a): H_2O with 10% of sucrose, (c): H_2O with 20% of sucrose and (e): H_2O with 30% of sucrose. Right panels: QENS spectra taken 70 μeV energy resolution; (b): H_2O with 10% of sucrose, (d): H_2O with 20% of sucrose and (f): H_2O with 30% of sucrose. Black points (\bullet) are the experimental data and the red lines (—) the fitting curves.

one with restricted dynamics due to interaction with sucrose molecules, the so-called “slow water”. Population of slow water component increases with the concentration of sucrose molecules. In fact, p_1 is 0.09, 0.245 and 0.26 for 10 SH_2O , 20 SH_2O and 30 SH_2O , respectively. Correspondingly, fast water population decreases with increasing number of sucrose molecules. Figure 4.5 reports the dependence of the translational diffusion coefficient of the fast component (D_T^{fast}) upon the sugar concentration in comparison with analogous results obtained by Feick and von Meerwall [74] using pulsed gradient spin-echo NMR. As can be seen, D_T^{fast} decreases with increasing sugar concentration and the agreement

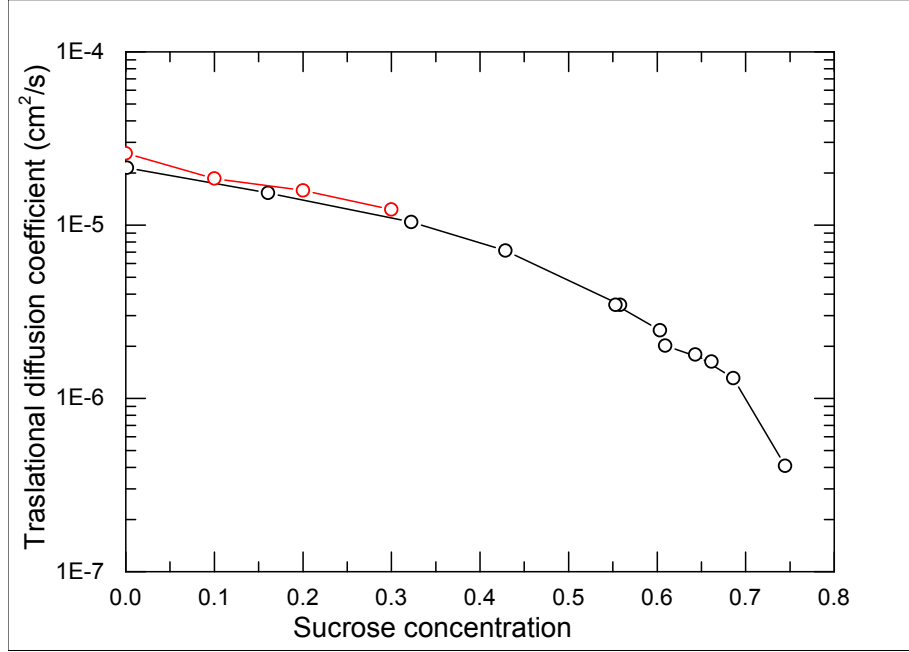


Figure 4.5: NMR [74] and our QENS measurements of the diffusion coefficients of water in sucrose solutions as a function of concentration. Black opened circle ($-\circ-$) are NMR measurements at 303 K and red opened circle ($-\circ-$) are our QENS measurements at 300 K.

between the two data set is very encouraging. Error bars of our data are inside the symbol size. Coherently, residence time of fast water component increases with increasing of sucrose percentage and it is higher than that of bulk water. Rotational diffusion coefficient is almost constant. Analogous results are obtained for the slow water component.

We define *fraction of fast water component* (F_{fast}):

$$F_{fast} = \frac{p_1}{p_2 + p_1}; \quad (4.2)$$

fraction of slow water component (F_{slow}):

$$F_{slow} = \frac{p_2}{p_2 + p_1}; \quad (4.3)$$

translational retardation factor (R_{trasl}):

$$R_{trasl} = \frac{D_T^{fast}}{D_T^{slow}}; \quad (4.4)$$

and *rotational retardation factor* (R_{rot}):

$$R_{rot} = \frac{D_R^{fast}}{D_R^{slow}}. \quad (4.5)$$

	Pure water		10SH ₂ O		20SH ₂ O		30SH ₂ O	
	value	error	value	error	value	error	value	error
f %			6E-2	7E-2	0.3	00.1	0.24	0.08
p_1 %			9.0	0.3	24.5	0.4	26.0	0.5
D_T^{slow} [cm ² /s]			5.0E-06	2E-07	5.9E-06	2E-07	3.8E-06	1E-07
τ_r^{slow} [ps]			2.4	0.6	6.14	0.40	8.7	0.5
D_R^{slow} [1/ps]			0.08	0.01	0.09	0.04	0.100	0.005
p_2 %			84.0	0.5	69	1	61.0	0.4
D_T^{fast} [cm ² /s]	2.60E-05	4E-07	2.00E-05	2E-07	1.94E-05	2E-07	1.59E-05	2E-07
τ_r^{fast} [ps]	0.90	0.05	1.34	0.04	3.10	0.07	3.9	0.1
D_R^{fast} [1/ps]	0.20	0.02	0.24	0.02	0.23	0.01	0.200	0.008
Γ_{CH_2} [meV]			0.30	0.03	0.32	0.03	0.175	0.006
p_3 %			7	1	7	1	13	1
χ_{red}^2	1.32		0.88		0.92		1.66	

Table 4.2: Parameters values obtained from the global fits for pure water measured IN6, H₂O with 10, 20 and 30% in weight of sucrose measured on IN5 at 300 K.

F_{fast} and F_{slow} defines the fraction of fast and slow water components over the total water, while R_{transl} and R_{rot} quantify the extent of retardation. This quantity is reported in Table 4.3. From Table 4.3 it is seen that F_{slow} increases with sugar concentration, while

SAMPLE [ref]	F_{fast} %	F_{slow} %	R_{transl}	R_{rot}	Exp. Technique
10SH ₂ O [this work]	90.3±0.3	9.7±0.3	4.0±0.2	3.1±0.2	QENS
20SH ₂ O [this work]	73.7±0.5	26.3±0.5	3.3±0.1	3±1	QENS
30SH ₂ O [this work]	70.1±0.5	39.9±0.5	4.2±0.1	2.0±0.2	QENS

Table 4.3: Percentage of fraction of “fast” and “slow” water populations together with translational and rotational retardation factors for 10SH₂O, 20SH₂O and 30SH₂O.

the retardation effect remains constant at about a factor of $3 \div 4$. Data in Table 4.3 imply that, on the average, a sucrose molecule is able to slow down the dynamics of about 18 ± 2 molecules in its hydration shell, a reasonable estimate given that hydration shell of sucrose is reported to be formed by between 7 and 38 water molecules, depending on the “hydration criterion” adopted [75]. It is clear, however, that the retardation effect extents belong the firmly hydrogen bonded water molecules reported to be $6 \div 7$ per sugar molecules.

In view of the great number of free parameters involved our global fits, a last point to be discussed concerns the reliability of our model determination, also in view of the possibility of minima in the χ^2 hypersurface. To this propose we perform a “confidence limits” analysis, as reported in Figures 4.6 and 4.7. In these figures we plot the quantity

of $\Delta\chi^2 = \chi_{p_i}^2 - \chi_{min}^2 + 1$ as a function of the value of parameters a_i . The constant black lines in the figures represent the 99% confidence interval. As can be seen, well pronounced not overlapping single minima are observed, highlighting the reliability of parameters determination and of the reported effect. Note also that in the case of the pure water - where only data at a single energy resolution were available - more noisy plots obtained and sometimes the minima are less defined. This highlights the importance of exploiting the availability of a great number of data at different energy resolutions to apply our global fit strategy.

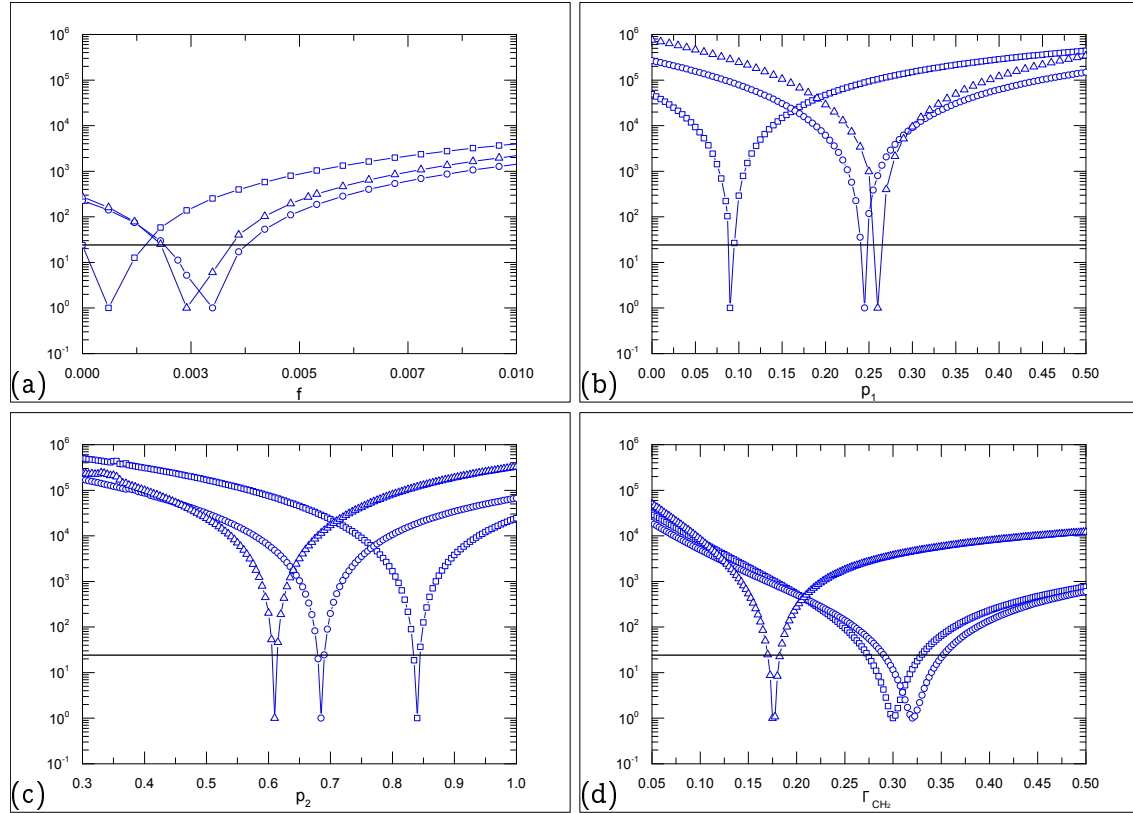


Figure 4.6: Confidence limits analysis: $\Delta\chi^2 = \chi_{p_i}^2 - \chi_{min}^2 + 1$ as a function of parameters; (a): f fraction, (b): p_1 fraction; (c): p_2 fraction; (d): Γ_{CH_2} fraction. Blue opened square (\square) are H_2O with 10% of sucrose, blue opened circle (\circ) are H_2O with 20% of sucrose, blue opened triangle (\triangle) are H_2O with 30% of sucrose. The horizontal black line cuts the plot at $\Delta\chi^2 = 24.2$ and determines the 99% confidence intervals.

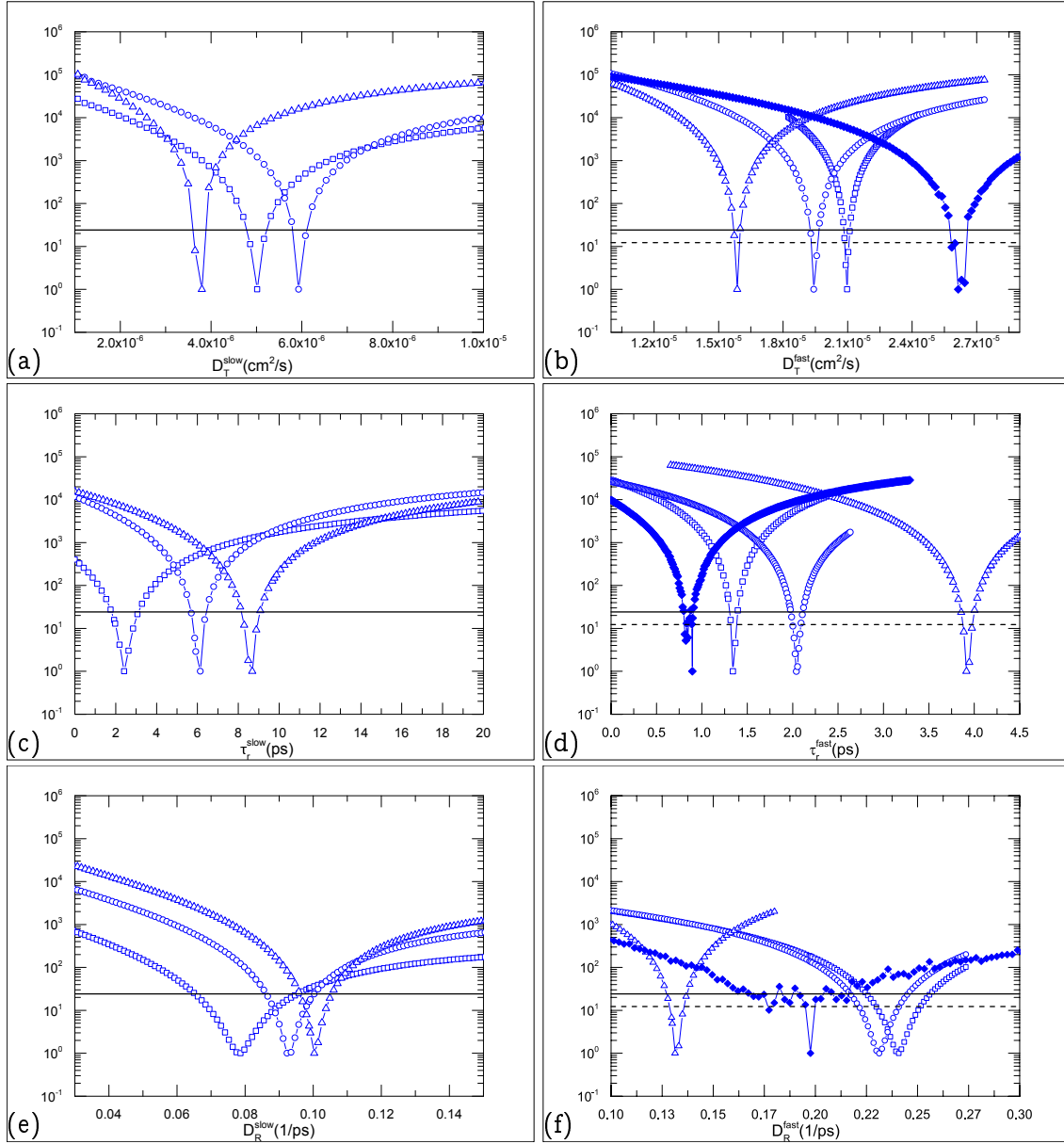


Figure 4.7: Confidence limits analysis: $\Delta\chi^2 = \chi_{p_i}^2 - \chi_{min}^2 + 1$ as a function of parameters; (a): D_T^{slow} , (b): τ_r^{slow} ; (c): D_R^{slow} ; (d): D_T^{fast} ; (e): τ_r^{fast} ; (f): D_R^{fast} . Blue opened square ($-\square-$) are 10SH₂O, blue opened circle ($-\circ-$) are 20SH₂O, blue opened triangle ($-\triangle-$) are 30SH₂O and blue filled diamond ($-\blacklozenge-$) are pure water. The horizontal black continuous/dashed line cuts the plot at 24.2 or at 12.3 to determine the 99% confidence intervals for sucrose solutions/pure water.

4.3 Conclusions

Study of “phantom” systems indicated that in the presence of solute biomolecules two water populations are observed: a fast one with dynamics property very similar to those of pure water and a slow one with the restricted dynamics. The dependence of the slow water population upon sugar concentration allowed to attribute this population to water molecules in the hydration shell of the solute biomolecules whose dynamics, both translational and rotational, is slowed down in dynamics by a factor of 3 with respected bulk water.

These results fully validate the physical model on which our data analysis approach is based and contribute to the basis for the analysis of more complex biological systems like cells and tissues.

Chapter 5

Water in cellular systems

5.1 Introduction

In this chapter we propose the QENS study of *in vivo* E. coli at three different temperatures: 300, 310 and 320 K in order first to evaluate the validity of the theoretical model chosen, that predicts two cited water populations and to give an apport to the literature. In addition, Glioma-9L (cancer cells injected in glia cells from mice) and Yeast cells (from fungus kingdom), at 300 K were also analyzed. Such samples are very different in shape, size and biological constituents. They allow to test if two water populations are a general property of cells.

5.2 Sample preparation

Cells used for the experiments were:

- Escherichia coli strain BL21(DE3)pLysS (Promega, Fitchburg, WI, USA). Bacteria colonies were grown on Luria-Bertani Agar medium plate at 37°C overnight. One colony was dissolved in 250 mL of Luria-Bertani medium and let grow overnight at 37°C under gentle stirring (250 rpm).
- Rat Glioma-9L cells, American Type Culture Collection, Manassas, VA; CRL-2200, were grown in Roswell Park Memorial Institute medium (RPMI) 1640 supplemented with 10% FBS and (100 units/ml) streptomycin (100 µg/ml). Cells were grown in tissue culture dishes in a humidified incubator (37°C, 5% CO₂) and were passaged when they were nearly confluent.
- Yeast Schizosaccharomyces pombe cells were grown with a standard procedures for vegetative in Edinburgh Minimal Medium [76].

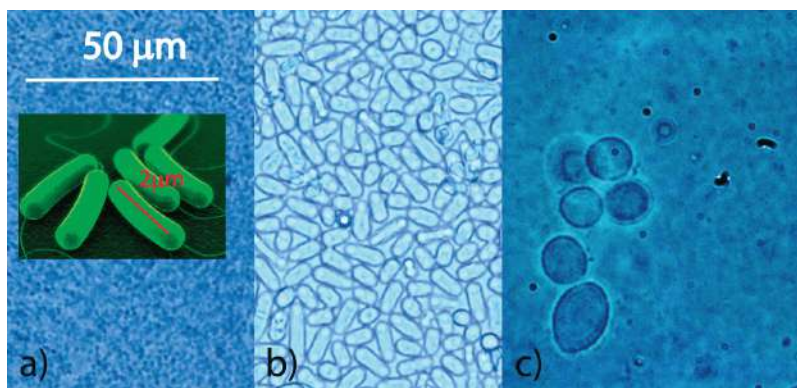


Figure 5.1: Sample image taken before the experiment with a fluorescence microscope. a) *E. coli* cells. b) Yeast *Schizosaccharomyces pombe* cells. c) Glioma-9L cells.

The cell cultures were kept at 4 °C in PBS buffer pH=7.4 to guarantee physiological conditions and to prevent cell death. Immediately before the experiments they were centrifuged for 7 min. at 7000 rpm; the supernatant was discarded and the remaining pellet used for experiments. Samples hydration was measured at the end of the neutron scattering experiments by drying and weighting. *E. coli*, yeast and Glioma-9L contained water at 64%, 69% and 50% by weight, respectively. In pellets of *E. coli* it has been reported that approximately 90% of the water present is intracellular and only less than 10% extracellular [16]. Although small variations, of the order of few percent, may be present for the other cell pellets, it can be safely assumed that in our samples most of the water is intracellular. Images of the samples were collected with optical zoom 100X, before and after the experiment, using a standard fluorescence microscope at EMBL (Grenoble, France), in order to check that the cells were still alive and without any degradation effect. Trypan blue exclusion tests, which allow distinguishing dead from alive cells, were also executed and guaranteed cells viability at the end of experiments. As can be seen from Fig. 5.1, *E. coli* are rod-shaped bacteria about 2.0 μm long and 0.25 μm in diameter, with a cell volume of 0.6 μm^3 ; yeast cells (eukaryotic microorganisms classified in the kingdom Fungi), are also roughly rod-shaped, typically measuring between 5 μm to 10 μm in length and between 1 μm to 2 μm in diameter; Glioma-9L are almost spherical (diameter about 10 μm) tumor cells obtained in vitro and very useful for *in vivo* studies to investigate the effects of various therapeutic agents on brain tumors.

5.3 Results

QENS experiments were performed on spectrometer IN5. These measurements were realized in the 2015 during the experiment number 8 – 04 – 470. QENS spectra of *E. coli* at three different temperatures, 300, 310 and 320 K, and Glioma-9L and yeast cells at 300 K

were taken at high and low energy resolution. We analyzed 26 spectra using global fittings strategy: 12 at high energy resolution and 14 at low energy resolution.

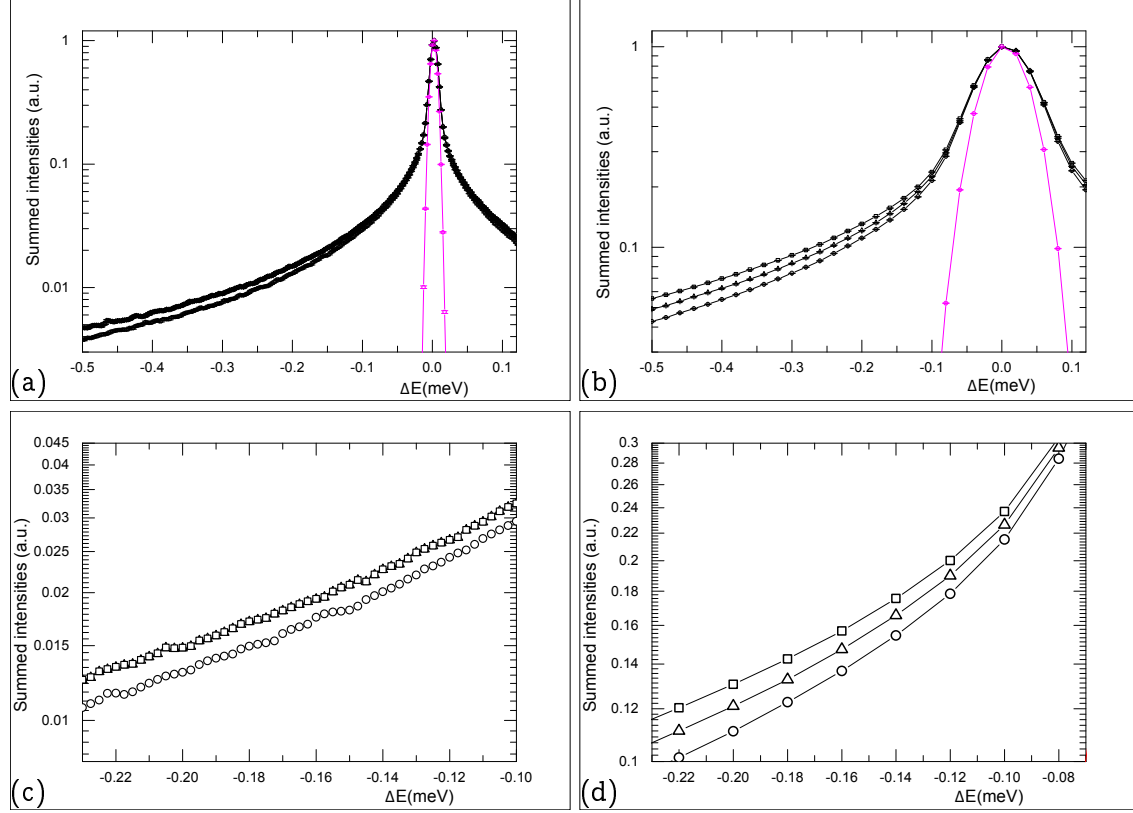


Figure 5.2: Panels (a) and (b): Summed intensities over all Q range of QENS spectra taken at 10 and 70 μeV energy resolutions, respectively. Panels (c) and (d) are a zoom view of panels (a) and (b), respectively. Black opened circle ($-\circ-$) are *E. coli* at 300 K, black opened triangle ($-\triangle-$) are *E. coli* at 310 K, black opened square ($-\square-$) are *E. coli* at 320 K and fuchsia opened circle ($-\circ-$) is the vanadium. The error bars in panels (c) and (d) are smaller than symbol size.

Figure 5.2 shows normalized QENS spectra, binned over the whole Q -range accessible, as a function of energy transfer at 10 (left panels) and 70 μeV (right panels) energy resolution for *E. coli* at 300, 310 and 320 K. Figure 5.4 shows the same curves for *E. coli*, Glioma-9L and yeast at 300 K. From a preliminary semi-quantitative analysis few comments are in order:

- looking at Figure 5.2, spectra of *E. coli* cells investigated at different temperatures show, as expected, an increment in dynamics with increasing temperature for both energy resolution. This is evident at low energy resolutions from panel (d). On the other hand, *E. coli* QENS spectra at high energy resolution present an increment in

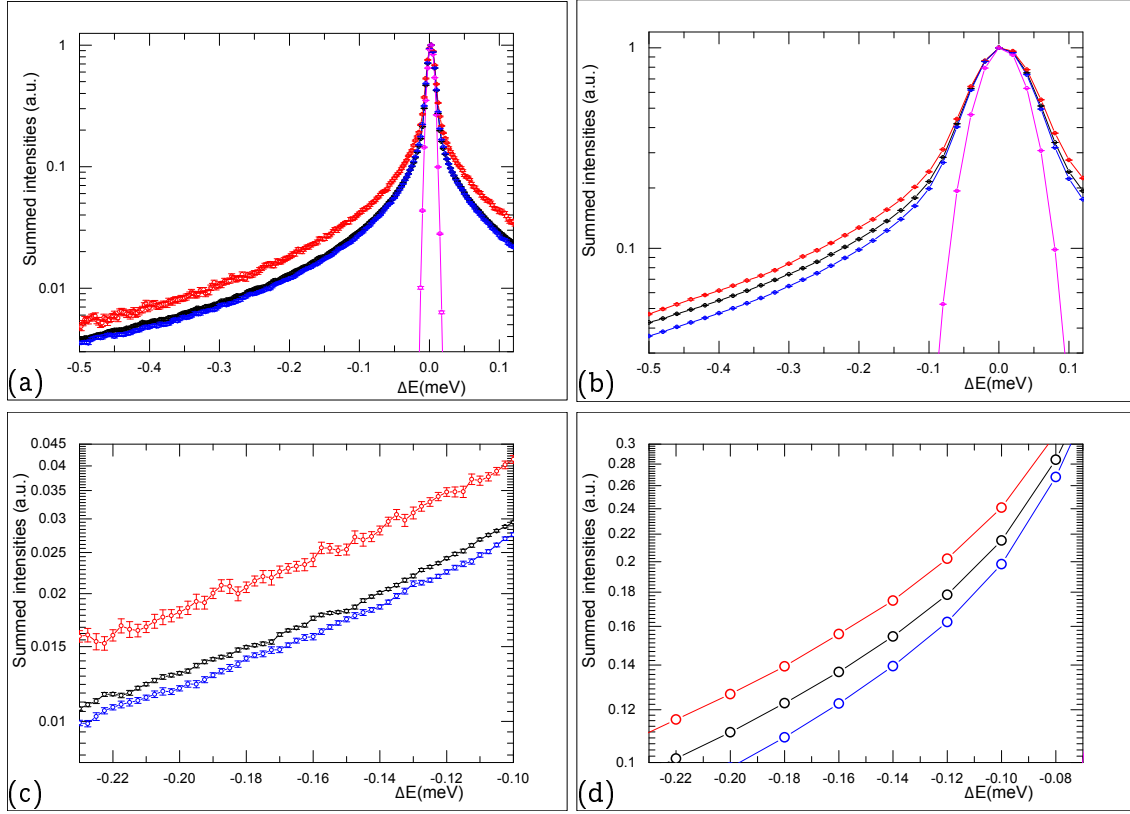


Figure 5.3: Panels (a) and (b): Summed intensities over all Q range of QENS spectra taken at 10 and 70 μeV energy resolutions, respectively. Panels (c) and (d) are a zoom view of panels (a) and (b), respectively. Black opened circle ($-\circ-$) are *E. coli* at 300 K, red opened circle ($-\circ-$) are Glioma-9L, blue opened circle ($-\circ-$) are Yeast at 300 K and fuchsia opened circle ($-\circ-$) is the vanadium. The error bars in panels (c) and (d) are smaller than symbol size.

dynamics between 300 and 310 K, while between 310 and 320 K there is no difference, as observed in panel (d).

- looking at Figure 5.3 Glioma-9L spectra exhibit at 300 K a faster dynamics compared to the other cells investigated. In particular, at high energy resolution the slow hydrogens are more detectable than fast ones. It means that the broadening of Glioma-9L QENS spectra at high energy resolution is probably due to an enhanced dynamics of slow water. A zoom of this effect is shown in panel (c). On the other hand, at low energy resolution, where, the time window is 10 ps, fast hydrogens are more detectable with respect to slow ones. Fast water component of Glioma-9L QENS spectra shows a faster dynamics compared with *E. coli* and yeast at 300 K, as it can be seen in panel (d) of Figure 5.3.

Moreover, Glioma-9L spectra show a faster Q-decay with respect the others cells spectra at the same temperature. It could be due to a larger Debye-Waller factor, i.e., of larger Mean Square Displacement.

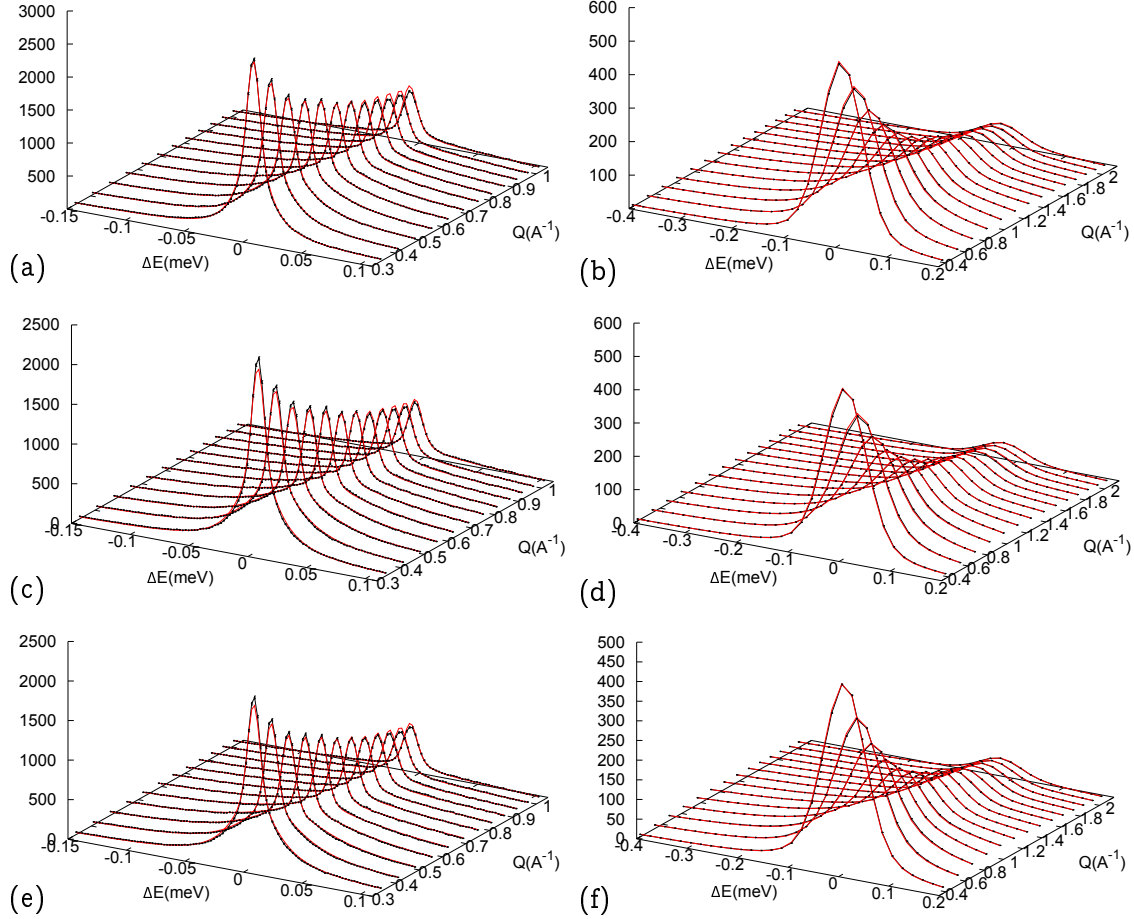


Figure 5.4: Left panels: QENS spectra taken 10 μeV energy resolution; (a): *E. coli* at 300 K, (c): *E. coli* at 310 K and (e): *E. coli* at 320 K. Right panels: QENS spectra taken 70 μeV energy resolution; (b): *E. coli* at 300 K, (d): *E. coli* at 310 K and (f): *E. coli* at 320 K. Black points (\bullet) are the experimental data and the red lines (—) the fitting curves.

These qualitative observations are fully confirmed by the parameters extracted using the global fit strategy, as evidenced in Table 5.1. In Figure 5.4 and in Figure 5.5 the fitted spectra of *E. coli* at 300, 310 and 320 K and Glioma-9L and yeast at 300 K are shown.

The broadening of Glioma-9L QENS spectra is also evident from the comparison with the others spectra at 300 K shown in Figure 5.4 and in Figure 5.5.

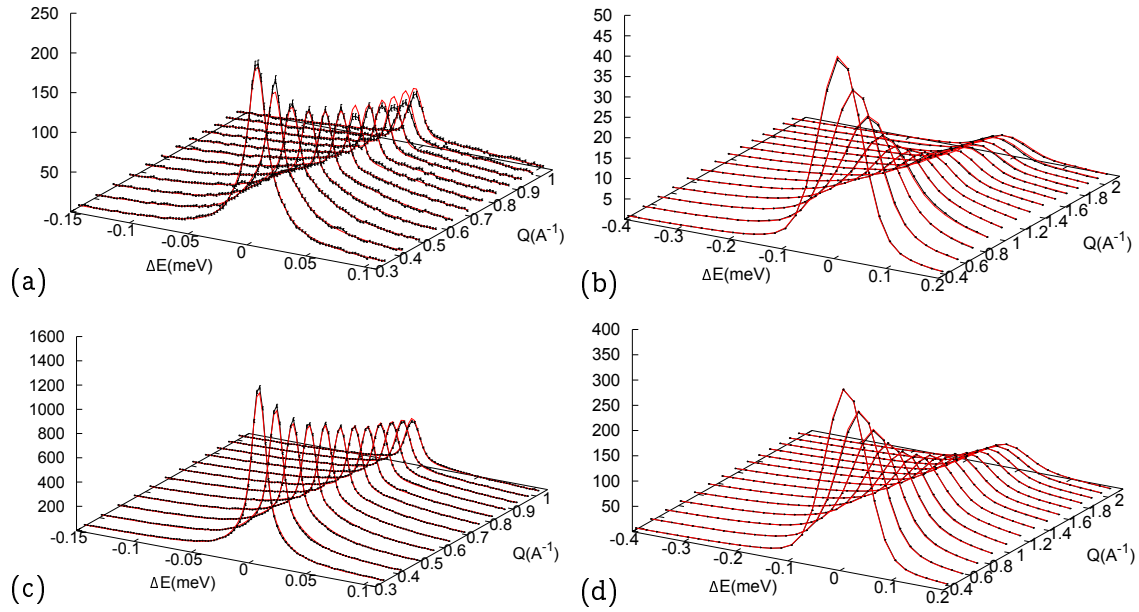


Figure 5.5: Left panels: QENS spectra taken 10 μeV energy resolution at 300 K; (a): Glioma-9L, (c): yeast. Right panels: QENS spectra taken 70 μeV energy resolution 300 K; (b): Glioma-9L, (d): yeast. Black points (\bullet) are the experimental data and the red lines (—) the fitting curves.

	E. coli/300 K		E. coli/310 K		E. coli/320 K		Glioma-9L/300 K		Yeast/300 K	
	value	error	value	error	value	error	value	error	value	error
f %	7.1	0.1	7.5	0.1	6.5	0.1	6.5	0.2	8.2	0.1
p_1 %	13.7	0.1	12.6	0.1	11.8	0.1	6.2	0.3	17.7	0.2
D_T^{slow} [cm^2/s]	2.1E-6	2E-7	2.7E-6	2E-7	2.1E-6	1E-7	3.9E-6	6E-7	2.2E-6	1E-7
τ_r^{slow} [ps]	34	2	17	1	13	1	53	12	33	2
D_R^{slow} [$1/\text{ps}$]	0.043	0.002	0.043	0.002	0.035	0.002	0.12	0.03	0.041	0.002
p_2 %	70.2	0.2	70.7	0.2	72.0	0.2	81.0	0.6	65.0	0.3
D_T^{fast} [cm^2/s]	2.13E-5	1E-7	2.65E-5	2E-7	3.13E-5	2E-7	2.16E-5	2E-7	2.04E-5	2E-7
τ_r^{fast} [ps]	1.28	0.02	1.18	0.02	0.96	0.02	0.84	0.06	1.65	0.04
D_R^{fast} [$1/\text{ps}$]	0.20	0.01	0.20	0.01	0.20	0.01	0.19	0.02	0.20	0.01
Γ_{CH_2} [meV]	0.170	0.01	0.435	0.003	0.549	0.004	0.118	0.002	0.273	0.003
p_3 %	9	0.2	9.2	0.2	9.7	0.2	6.3	1.2	9.1	0.6
χ_{red}^2	1.58		1.37		1.24		0.54		1.01	

Table 5.1: Parameters values obtained from the global fits for *E. coli* at 300, 310 and 320 K, Glioma-9L and yeast at 300 K.

SAMPLE [ref]	$F_{fast}\%$	$F_{slow}\%$	R_{transl}	R_{rot}	Exp. Technique
RBC [23]	90	10	40		QENS
D E. coli cells [14]	85	15		15	NMR
D E. coli cells [15]	100	0			QENS
Hmm cells [15]	24	76	250		QENS
Hmm cells [14]	85	15		15	NMR
D E. coli cells (300 K)[this work]	85	15	10	5	QENS
D E. coli cells (310 K)[this work]	85	15	10	5	QENS
D E. coli cells (320 K)[this work]	86	14	15	6	QENS
Yeast cells [this work]	79	21	9	5	QENS
Glioma-9L cells [this work]	93	7	6	1.6	QENS
RCH of bovine [46]	82	18	10	2.7	QENS

Table 5.2: Fractions of “fast” and “slow” water populations together with translational and rotational retardation factors for various biological samples. RBC: Red Blood Cells; Hmm: *Haloarcula marismortui*.

Quantitative analysis of water dynamics in cells The quantitative information were summarized in Table 5.1. The physical parameters obtained are, as mentioned, in agreement with the qualitative observations. The agreement between the theoretical model and the experimental data suggests that the chosen theoretical model is able to describe such complex systems.

E. coli cells was investigated at different temperatures as references. In fact, many works investigating this topic are present in literature. Some of them are cited in the introduction at page 2. Looking at Table 5.1, combining data from two time windows (10 and 70 ps) we found two water populations in E. coli cells. In such sense, we are in agreement with Persson et al. [14] that, as mentioned, in the Introduction (Chapter 1) found two water populations in *Haloarcula marismortui*. The fraction of two water populations seems, as expected, to be affected by the increasing of the temperature. Fast component of E. coli shows an increment in translational diffusion increasing the temperature with the expected decrement of the residence time, while rotational diffusion coefficient seems not depending from the temperature, at least in the investigated range. In the slow water component the residence time decreases with the increasing of the temperature, which seems reasonable, while keeping unchanged (or almost) translational diffusion coefficients. To conclude, Γ_{CH_2} increases, as expected, while keeping almost constant its fraction population. The most important result is the existence of two water populations as a general property in living cells. Table 5.2, show fast and slow water fraction components calculated over the total amount of water ($F_{slow} = p_1/(p_1 + p_2)$ and $F_{fast} = p_2/(p_1 + p_2)$) for comparison with results available in the literature. The majority percentage of water (p_1 between 65% and 81% or in other words, F_{fast} between 79% and 85%) shows property similar to bulk water.

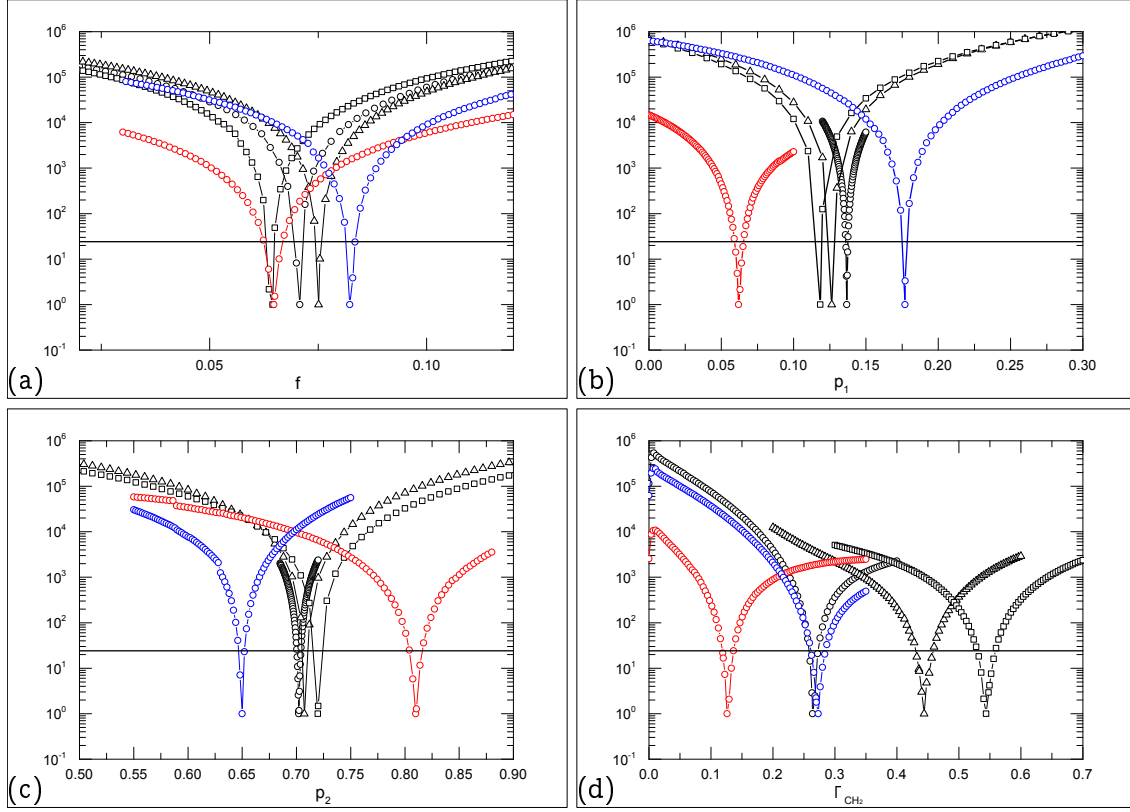


Figure 5.6: Confidence limits analysis: $\Delta\chi^2 = \chi_{p_i}^2 - \chi_{min}^2 + 1$ as a function of parameters; (a): f fraction, (b): p_1 fraction; (c): p_2 fraction; (d): Γ_{CH_2} fraction. Black opened circle ($-\circ-$) are *E. coli* at 300 K, black opened triangle ($-\triangle-$) are *E. coli* at 310 K, black opened square ($-\square-$) are *E. coli* at 320 K, red opened circle ($-\circ-$) are Glioma-9L and blue opened circle ($-\circ-$) are Yeast at 300 K. The horizontal black line cuts the plot at $\Delta\chi^2 = 24.2$ and determines the 99% confidence intervals.

Fast water component in our living cells at 300 K is characterized as follows: D_{cells} assumes value between 2.02 and $2.18 \times 10^{-5} \text{ cm}^2 \text{ s}^{-1}$, $\tau_{r,cells}$ assumes values between 0.78 and 1.69 ps (since is not free water) and $D_{R,cells}$ assumes value between 0.17 and 0.21 ps^{-1} . The results are very close to those of bulk water. Due to the evident results, in such sense, we agree with the statement by Jasnin et al. [16] that intracellular water is not substantially “tamed” by confinement, and we are far to think that the water is gel-like as was assumed by Pollack [8].

Slow water component in our living cells at 300 K, with reduced dynamics, is characterized as follows: D_{cells} assumes value between 1.9 and $4.5 \times 10^{-6} \text{ cm}^2 \text{ s}^{-1}$, $\tau_{r,cells}$ assumes values between 31 and 65 ps and $D_{R,cells}$ assumes value between 0.039 and 0.15 ps^{-1} . Excluding Glioma-9L, that show faster dynamics properties in slow water component, trans-

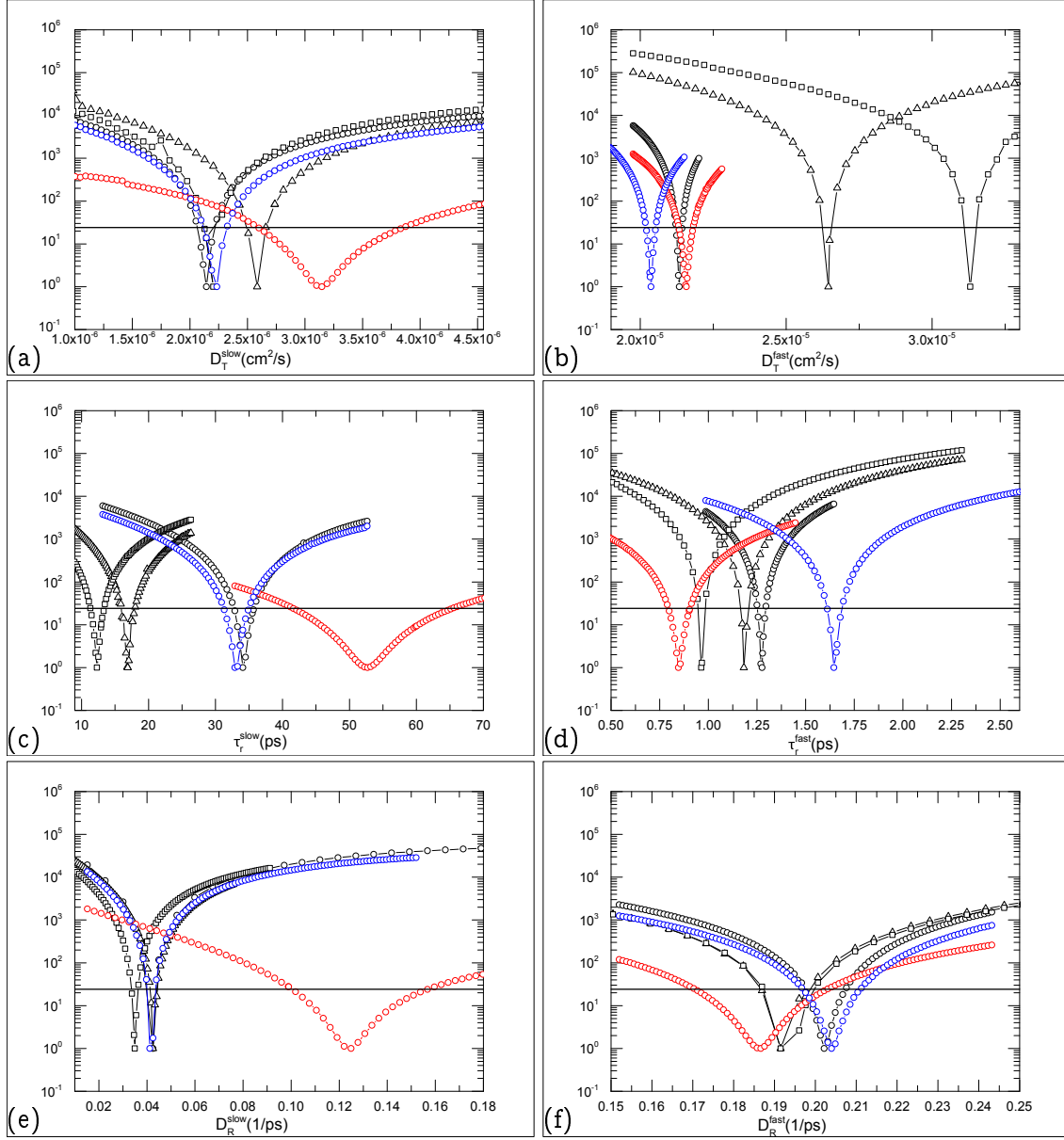


Figure 5.7: Confidence limits analysis: $\Delta\chi^2 = \chi_{p_i}^2 - \chi_{min}^2 + 1$ as a function of parameters; (a): D_T^{slow} , (b): τ_r^{slow} ; (c): D_R^{slow} ; (d): D_T^{fast} ; (e): τ_r^{fast} ; (f): D_R^{fast} . Black opened circle ($-\circ-$) are *E. coli* at 300 K, black opened triangle ($-\triangle-$) are *E. coli* at 310 K, black opened square ($-\square-$) are *E. coli* at 320 K, red opened circle ($-\circ-$) are Glioma-9L and blue opened circle ($-\circ-$) are yeast at 300 K. The horizontal black line cuts the plot at $\Delta\chi^2 = 24.2$ giving a confidence of 99%.

lational and rotational diffusion coefficients show a slowing down in dynamics of one order of magnitude. Speaking in terms of translational and rotational retardation factors, ($R_{transl} = D_T^{fast}/D_T^{slow}$ and $R_{rot} = D_R^{fast}/D_R^{slow}$), defined to make comparison with existing results in literature (see Table 5.2) we obtain a translational retardation factor between 6 and 15, and a rotational retardation factor between 5 and 6 (excluding 1.6 of Glioma-9L). The confidence limit investigation shown in Figure 5.6 and Figure 5.7 gives a graphical representation of parameters obtained (see Table 5.1) using the global fit strategy. The explored hypersurface of the $\Delta\chi^2 = \chi^2 - \chi_{min}^2$ proofs that the parameters are well defined thanks to the strategy of implementing a global fit on QENS spectra using two different resolutions.

5.4 Conclusions

In this chapter QENS spectra of three different types of cells were presented: *E. coli*, as reference, yeast and Glioma-9L. All of them were investigated at 300 K. Moreover, *E. coli* spectra were measured also at 310 and 320 K. We assumed that the majority of the water present in the sample was the one that lies in the IntraCellular Space. This point clarifies that the two water populations found in our work do not correspond with intra and extra water populations found in NMR results, but are fast and slow components of intracellular water. The main results obtained can be summarized as follows:

- *E. coli* cells studied as a function of temperature gives expected results. An increment in dynamics in both slow and fast components of translational motions upon increasing temperature with a retardation factor between 10 and 15 was observed. On the other hand, rotational motions of fast component does not depend on the temperature. The retardation factor assumes values between 5 and 6.
- The presence of two populations of intracellular water, a majority one with bulk-like dynamics and a minority one with slower dynamics, seems to be a general property of living cells, despite cellular biodiversity.
- Glioma-9L cells exhibits a decrement of slow water component, 6.5% against 13.7% for *E. coli* and 17.7% for Yeast. To that corresponds an increment of the fast water contribution. A faster diffusion for translational and rotational water motions of slow water component was observed. This result is encouraging being in agreement with those obtained by Callisto et al. [77]. In fact, they studied four brains affected by different kinds of tumors using MR imaging, DW-MRI and proton MR spectroscopy. They found that Glioma tumors show higher value in Apparent Diffusion Coefficient (ADC). This ensure that such results from DW-MRI and QENS techniques are reasonable. A possible explanation for such increasing of slow water diffusion is not easy and further investigations are needed and planned to clarify the origin of such experimental observation.

Looking at CH_2 groups component we observed a narrower width of 0.118 meV with respect to E. coli and Yeast that show widths CH_2 of 0.17 and 0.273 meV, respectively. The translational and rotational retardation factors summarize this effect assuming smaller values: 6 and 1.6, respectively.

Chapter 6

Water in bovine brain tissues

6.1 Introduction

In this Chapter we propose our contribution on bovine brain tissues investigation studying water diffusion in Right Cerebral Hemisphere (RCH), Left Cerebral Hemisphere (LCH), Right Cerebellum (RC) and Left Cerebellum (LC) using neutron scattering techniques.

First, we will compare the results obtained for right cerebral hemispheres and right cerebellum hemispheres in order to point out the main difference between cerebrum hemispheres and cerebellum, avoiding the effect of a possible right-left asymmetry. Then results from left and right cerebral hemispheres and from left and right cerebellum will be discussed in order to evaluate the existence of some possible asymmetry left/right in water dynamics. Since our model was able to describe water dynamics of sucrose in aqueous solutions and in cellular systems different in shape and size, we expect that such model resolves two water dynamics populations also for the most complex systems presented in this thesis.

6.2 Brain

Due to complexity architecture of the brain, in this Section in order to have an idea of our investigated samples we present a brief introduction on anatomy of the mammalian brain. Bovine has a mammalian brain that is classified as a vertebrates brain. The weight of a bovine brain is between 450 and 500 g and it is the $\sim 0.1\%$ of the bovine body weight. In Figure 6.1 a dorsal section (panel (a)) and lateral section view (panel (b)) of bovine brain is shown. The cerebral and cerebellar hemisphere are labeled in Figure 6.1.

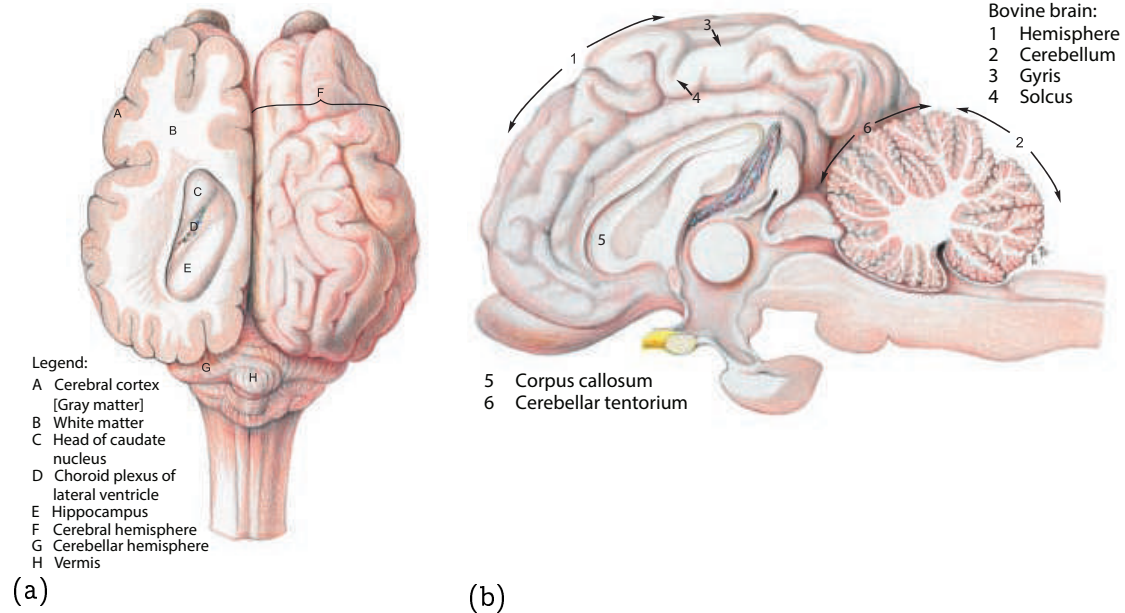


Figure 6.1: Figure 6.1a shows section of bovine cerebrum (dorsal view). Figure 6.1b shows median section of the bovine brain [78].

6.2.1 Cerebrum

The cerebrum is the largest part of the brain which contains the *cerebral cortex* and the two *cerebral hemispheres*. The cerebral cortex, existing only in mammalian brain, is the outer layer of the cerebral hemispheres. The cerebral cortex is made of *grey matter (GM)* and its surface folds in *gyri* and *sulci* which increase its area. Right and left cerebral hemispheres are joined in the centre by a band of nerve fibres, the *corpus callosum*, allowing communication. The inner part of the cerebral hemispheres is made by white matter (WM) because of the presence of the myelinated axons, which conduct signals more quickly than that unmyelinated ones.

GM and WM are different in their constituents. In fact, GM contains a large number of nerve body cells and relatively few myelinated axons, viceversa for WM that, having a large amount of myelin, appears white. The axon where the electrical impulse travels can be some millimeter or even up one meter.

6.2.2 Cerebellum

The cerebellum means “little brain” and it is more evolved in mammals specie. The cerebellum is separated from the rest of the brain above by a tough fibrous sheet, the *cerebellar tentorium*. The bovine cerebellum is much more complex and irregular than the

human one. The cerebellum consists of *cerebellar cortex* and in a deep white matter core. As the cerebrum we can distinguish in right and left side called *cerebellar hemispheres*. The cerebellar cortex is a convoluted sheet of GM consisting of three layers. From the outer to the inner the three layers are: (1) molecular layer with thickness between 300 and 400 μm , (2) ganglionic or Purkinje cell body layer and (3) the granular layer [79]. It is found that small body cells, *granular cells*, are allocated in the granular layer with thickness at about 100 μm . The cerebral cortex contains more neurons with respect to the total neurons from the rest of the brain due to such granular cells. In the core of the cerebellum there are the *deep nuclei* where clusters of GM are found within the WM. The major part of the cerebellum core is made by WM.

6.2.3 Lateralization

We give a very brief overview of the scientific interest about brain asymmetry. Left and right sides of the brain seem to have different tasks. The origin of that might have a biophysical explanation. For example, some of the functions as language, calculus and logic are dominant or strongly lateralized in left hemisphere, while prosody and visual-spatial process are typically associated to the right hemisphere [80].

Thus, many works in literature are focused on giving a topological characterization of human brain using stereological methods, fMRI, mapping brain from microscope images, dMRI and DW-MRI techniques. Some of those studies [81, 82, 83, 84, 85, 86, 87] show that myelinated and unmyelinated axons could have an important role in lateralization function because the signal propagation is more efficient in the first case. However, there are controversial results and disagreement concerning the hemispheric asymmetry, probably due to the fact that the asymmetry can be different from species to species and even from one individual to the other. Some differences could also be found in the genre and in the aging process.

Left-right asymmetry in the brain can reflect different diffusion properties of water. DW-MRI techniques was used to investigate water diffusion spatial asymmetry as consequence of the brain intrinsic asymmetrical structure. The water apparent diffusion coefficient was extracted using this techniques. Some of the results are reported in [83, 87].

6.3 Sample preparation

The samples for the QENS experiments were brain tissues from left and right cerebral hemispheres (LCH and RCH, respectively) and from left and right cerebellum (LC and RC, respectively). Fresh post-mortem bovine brains were obtained from the slaughter-house in Padova (Italy). Brain tissues were extracted at the Department of Animal Medicine, Production and Health of the University of Padova (Italy). The brains were removed and dissected in two parts: the cerebellum, and the cerebrum, then separated at the junction

of the pons and the cerebral peduncle. Sections (0.5 cm x 1 cm) of RCH and LCH were extracted from the cerebrum and frozen at -160°C in liquid nitrogen vapour.

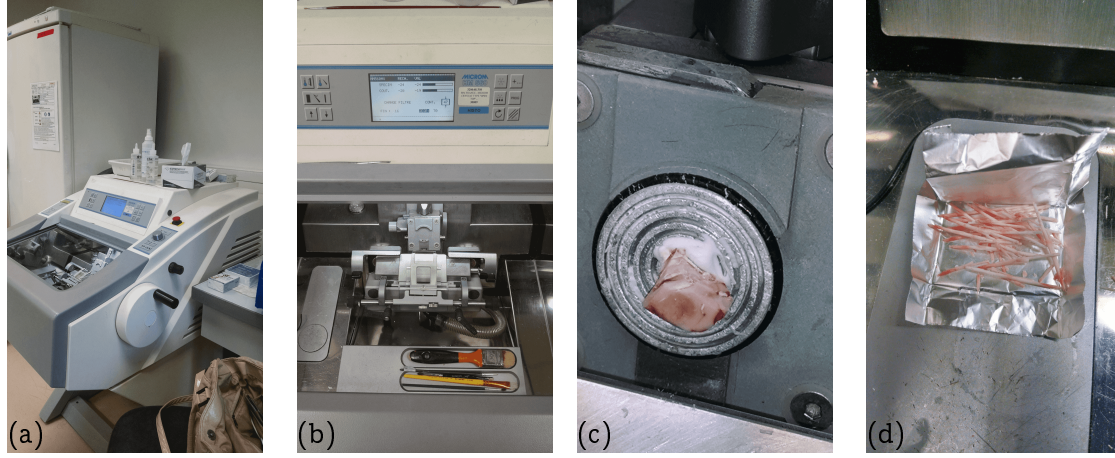


Figure 6.2: Panel (a) shows a picture of cryotome Thermo Scientific Microm HM 560 Cryostat-Series at neuroscience department in Grenoble - France. Panel (b) shows a frontal view of such cryotome. Panel (c) shows the metal disc with the glued specimen allocated in vertical position in order to cut the specimen in slices. Panel (d) shows slices of brain tissues in the aluminium foil before to be closed within the sample holder.

To perform neutron scattering experiment, RCH, LCH, LC and RC samples were cut in slices with a thickness of $50\text{ }\mu\text{m}$ using cryotome Thermo Scientific Microm HM 560 Cryostat-Series at neuroscience department in Grenoble - France. A picture of the used cryotome is shown in Figure 6.2(a) and 6.2(b). The specimen was glued on a *metal disc* trough a gel like medium called O.C.T. which consists in a compound of poly ethylene glycol and polyvinyl alcohol. The metal disc with the fixed specimen was displaced in vertical position as shown in Figure 6.2(c). During cutting process the temperature was kept at -20°C to preserve the tissues and to make easier the cutting process. The thickness of the tissue slices was chosen in order to limit neutron absorption from water (H_2O), thus minimizing multiple scattering events. In Figure 6.2(d) slices of brain bovine tissue are stored in the aluminium foil. Thus, the sample is ready to be closed within the flat aluminium sample holder.

6.4 Results

QENS experiments were carried out on the spectrometer TOFTOF. This measurement was realized in 2015 during the experiment number 8683. The experiment was performed at high and at low energy resolution, $FHFW \sim 10$ and $70 \mu\text{eV}$ (70 and 10 ps), respectively. Explored Q-range was between 0.33 and 0.96 \AA^{-1} for high energy resolution data and 0.33 and 1.8 \AA^{-1} for low energy resolution data. After data manipulation of QENS rawdata we obtained 11 and 14 curves from high and low energy resolutions, respectively. Therefore, we analyse 25 curves using the procedure explained in the Chapter 3.

QENS spectra relative to RCH and LCH are reported in Figure 6.3, together with global fits. The good agreement between data fit curves is confirmed by the χ^2_{red} values of 1.49 and 1.17 and 0.93 and 1.02 for RCH, LCH, RC and LC, respectively. Parameters are reported in Table 6.1 for RCH and RC, in Table 6.2 for RCH and LCH and Table 6.2 for RC and LC. Before proceeding to detailed comparison between various samples, some general comments are in order:

- in analogy with results from cells, non zero values of parameters of f and Γ_{CH_2} are found: there are hydrogens that appear as immobile during the time scale investigated, and hydrogens belonging to CH_2 groups, essentially located in the lipids part of the samples membranes, myelin, white matter, etc.
- also for bovine brain tissues we are able to identify two water populations: a “fast” one with dynamics properties similar to bulk water and a “slow” one with restricted dynamics. Based on the results obtained on “phantoms” systems and with cellular systems we attribute the slow component to water molecules interacting macro-molecular surface inside the tissues (i.e. biomolecules hydration water) and the fast component to water molecules not strongly interacting with other biomolecules and therefore able to roto-translate almost freely.

6.4.1 Results from right side of cerebral hemisphere and cerebellum

In this Subsection we focus our attention on right cerebral hemisphere and on the right cerebellum. Our aim is to put in evidence the differences between cerebral hemisphere and cerebellum, avoiding possible effect arising from left-right asymmetry. Parameter value are reported in Table 6.1. From Table 6.1 it is evident that cerebral hemisphere has a larger populations of immobile hydrogens and slow water component and of hydrogens belonging to CH_2 groups (higher values of parameters f , p_1 and CH_2) and, consistently lower population of fast water component (lower value of the parameter p_2). Effects on translational and rotational diffusion coefficients, on residence times and on width on the CH_2 component are, if any, hardly detectable. This suggest a locally more compact structure with a larger amount of CH_2 groups for the cerebral hemisphere with respect to the cerebellum and it consistent with the common belief that cerebellum contains a

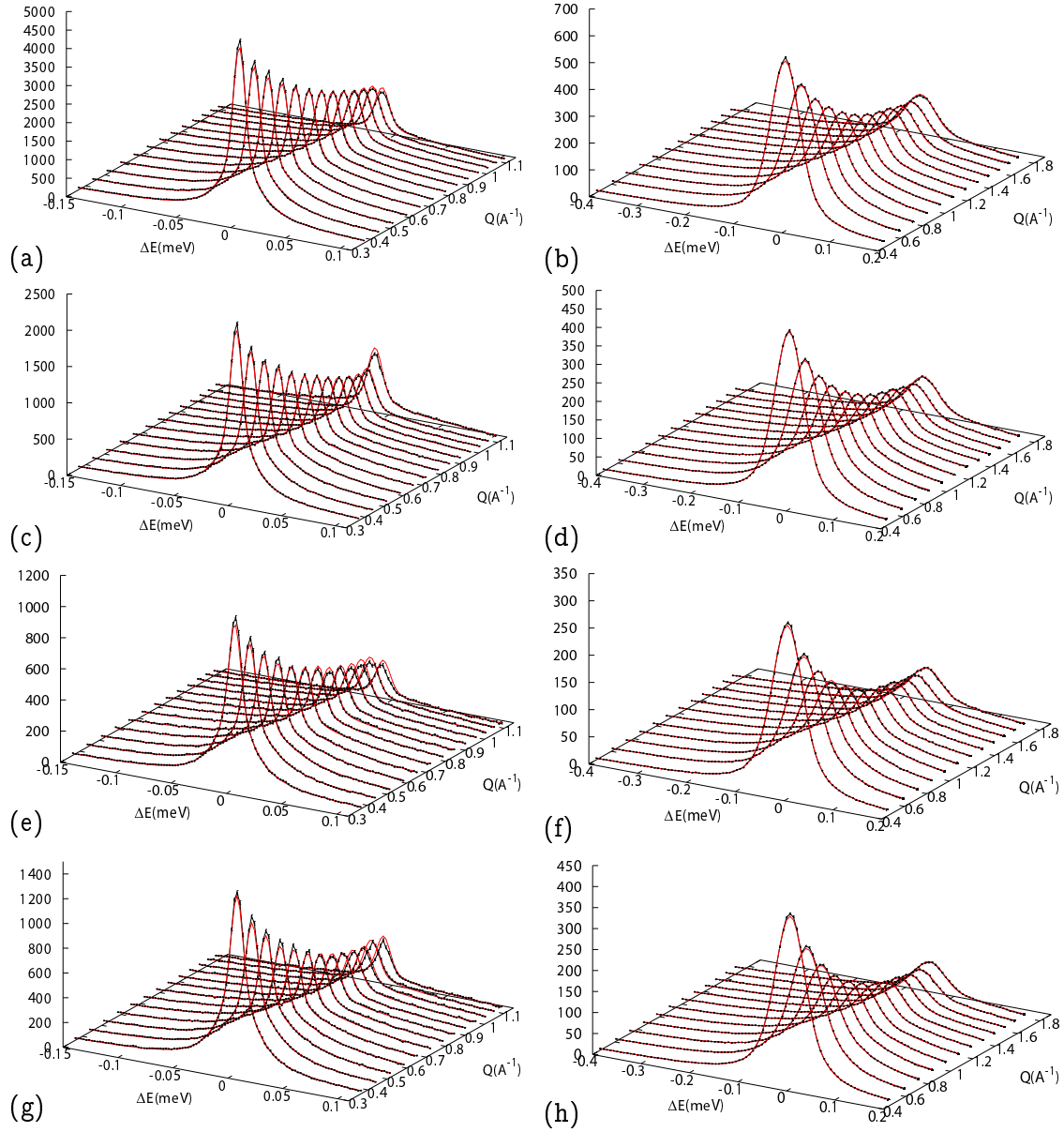


Figure 6.3: Left panels: QENS spectra taken 10 μeV energy resolution; (a): RCH, (c): LCH, (e): RC and (g): LC. Right panels: QENS spectra taken 70 μeV energy resolution; (b): RCH, (d): LCH, (f): RC, (h): LC. Black points (\bullet) are the experimental data and the red lines ($-$) the fitting curves.

large amount of grey matter (neurons). We note also that our results on RCH are in

general good agreement with those reported by Natali et al. [46], and attribute the small differences between the two data sets to the improvement of current data quality, achieved by combining two complementary energy resolutions which allows, in particular, to better determine residence times etc.

	RCH		RC	
	value	error	value	error
f %	9.8	0.1	7.3	0.1
p_1 %	15	1	12.0	0.4
D_T^{slow} [cm ² /s]	2.3E-06	1E-07	2.0E-06	1E-07
τ_r^{slow} [ps]	5	1	6	4
D_R^{slow} [1/ps]	0.11	0.01	0.07	0.01
p_2 %	62	1	73	0.6
D_T^{fast} [cm ² /s]	2.50E-05	2E-07	2.3E-05	2E-07
τ_r^{fast} [ps]	2.67	0.05	2.04	0.06
D_R^{fast} [1/ps]	0.16	0.01	0.16	0.01
Γ_{CH_2} [meV]	0.252	0.001	0.27	0.03
p_3 %	14	1	8	1
χ_{red}^2	1.49		0.93	

Table 6.1: Parameters values obtained from the global fits for RCH and RC.

6.4.2 Left-Right asymmetry in cerebral hemispheres and cerebellum

Parameters relative to RCH and LCH are reported in Table 6.2. To main observations we can make:

- no left-right asymmetry is present for the various populations. In fact, parameters f , p_1 , p_2 and p_3 are almost identical for RCH and LCH. This suggest that the overall composition and morphology of our right and left cerebral hemispheres specimens is equal.
- Concerning the dynamical parameters (translational and rotational diffusion coefficients, residence times and width of the CH_2 groups) the general observation can be made is that the left hemisphere is characterized by slower dynamics with respect to the right one, both for water dynamics and for CH_2 groups dynamics. The effect is almost evident for the rotational diffusion coefficient of the “slow” water component that in the LCH is a factor of 2.4 smaller than in RCH and in the width of the CH_2 component which is reduced by about of 60%. One might speculate that the slower dynamics involves essentially the myelin rich white matter of LCH and its hydration shell.

	RCH		LCH	
	value	error	value	error
f %	9.8	0.1	8	0.2
p_1 %	15	1	16.7	0.5
D_T^{slow} [cm ² /s]	2.3E-06	1E-07	2.0E-06	1E-07
τ_r^{slow} [ps]	5	1	7	2
D_R^{slow} [1/ps]	0.11	0.01	0.046	0.006
p_2 %	62	1	64	1
D_T^{fast} [cm ² /s]	2.50E-05	2E-07	2.35E-05	3E-07
τ_r^{fast} [ps]	2.67	0.05	1.97	0.09
D_R^{fast} [1/ps]	0.16	0.01	0.13	0.01
Γ_{CH_2} [meV]	0.252	0.001	0.149	0.007
p_3 %	14	1	11	2
χ_{red}^2	1.49		1.17	

Table 6.2: Parameters values obtained from the global fits for RCH, LCH.

Parameters relative to RC and LC are reported in Table 6.3. From this Table it is evident that for the cerebrum effects of left-right asymmetry are, if any, much less evident than for cerebral hemispheres. In order to focus on the dynamics of water in brain tissues, we report in Table 6.4 the fractions of fast and slow water and the translational and rotational retardation factors - as defined in Chapter 4 - for the present bovine brain samples, together analogous quantity relative to rat and human brain. Samples obtained by others authors with dMRI or QENS techniques. Both techniques are able to detect in the sample investigated two water populations: a majority one with fast dynamics and a minority one with slower dynamics. However, the extent of retardation is quite different: about factor of 5 as detected with dMRI and about a factor of 10 as detected by QENS. A possible origin of this difference may be traced to the different time/lenght scale investigated by the two techniques: microsecond/microns (at best) for dMRI, picosecond/nanometers for QENS. Therefore, one might think that the origin of the retardation effect detected by dMRI is the interaction of a micrometric water flow with micron-sized structures in the sample; at difference for QENS the origin of the retardation measured is the interaction of hydration water with macromolecular (proteins, lipids, etc) surfaces. Finally also for the present results we checked the reliability of our parameter determination by performing the “confidence limits” analysis, as reported in Figure 6.4 and 6.5.

6.5 Conclusions

Aim of the QENS experiments reported in this Chapter was to extend our studies on the dynamical properties of water in biological systems to really complex systems like

	RC		LC	
	value	error	value	error
f %	7.3	0.1	7	0.1
p_1 %	12.0	0.4	13.0	0.4
D_T^{slow} [cm ² /s]	2.0E-06	1E-07	2.7E-06	1E-07
τ_r^{slow} [ps]	6	4	2	2
D_R^{slow} [1/ps]	0.07	0.01	0.06	0.01
p_2 %	73.0	0.6	73.0	0.5
D_T^{fast} [cm ² /s]	2.30E-05	2E-07	2.27E-05	2E-07
τ_r^{fast} [ps]	2.04	0.06	1.71	0.04
D_R^{fast} [1/ps]	0.16	0.01	0.18	0.01
Γ_{CH_2} [meV]	0.270	0.004	0.207	0.003
p_3 %	8	1	7	1
χ_{red}^2	0.93		1.02	

Table 6.3: Parameters values obtained from the global fits for RC and LC.

SAMPLE [ref]	F_{FAST} %	F_{SLOW} %	R_{TRASL}	R_{ROT}	Exp. Technique
Whole rat brain - in vivo [88]	80	20	4.9		dMRI
Whole rat brain - post-mortem [88]	90	10	5.6		dMRI
Whole human brain [89]	80	20	4.2		dMRI
Right-left human brain [33]	80	20	8		dMRI
Whole rat cortex [45]	80	20	3.2÷4.3		dMRI
RCH of bovine [46]	82	18	10	2.7	QENS
RCH of bovine [this work]	81±1	19±1	11.0±0.6	1.5±0.2	QENS
LCH of bovine [this work]	79.3±0.7	20.7±0.7	11.9±0.8	2.9±0.6	QENS
RC of bovine [this work]	85.9±0.5	14.1±0.5	11.6±0.7	2.4±0.4	QENS
LC of bovine [this work]	84.9±0.5	15.1±0.5	8.3±0.4	2.9±0.6	QENS

Table 6.4: Percentage of “fast” and “slow” water populations together with translational and rotational retardation factors for RCH, LCH, RC and LC.

bovine tissues and to try to get evidence on the possible existence of left-right asymmetry in the brain, at the molecular level. The main results obtained can be summarized as follows:

- the existence of two water populations - a “fast” one with dynamics properties similar to bulk water, and a “slow” one with slower dynamics - has been detected also, confirming previous suggestions coming from dMRI experiments. However, retardation factor detected by QENS are a factor of two larger than those detected by dMRI. The origin of this difference has been traced to the different time/lenght

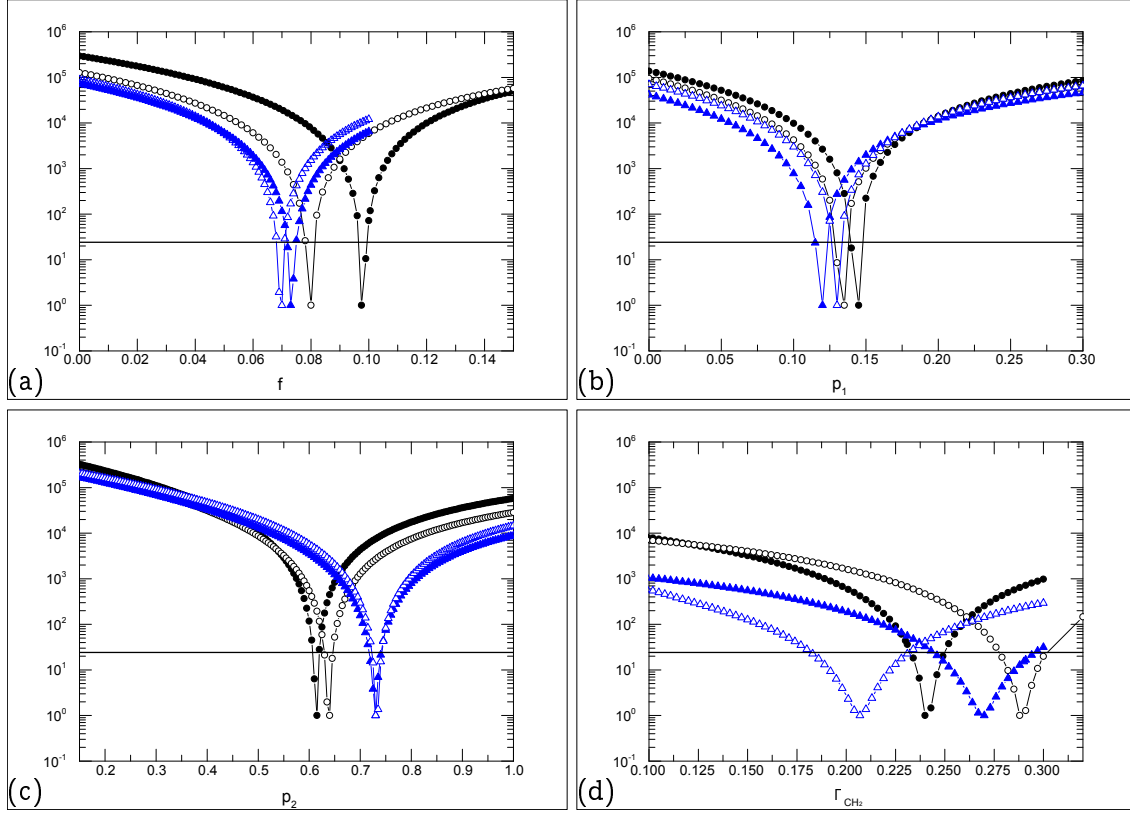


Figure 6.4: Confidence limits analysis: $\Delta\chi^2 = \chi^2_{p_i} - \chi^2_{min} + 1$ as a function of parameters; (a): f fraction, (b): p_1 fraction; (c): p_2 fraction; (d): Γ_{CH_2} fraction. Black filled circle ($-\bullet-$) are RCH; black opened circle ($-\circ-$) are LCH; blue filled triangle ($-\blacktriangle-$) are RC; blue opened triangle ($-\triangle-$) are LC. The horizontal black line cuts the plot at $\Delta\chi^2 = 24.2$ and determines the 99% confidence intervals.

scales investigated by the two techniques.

- The QENS techniques is able to detect subtle composition differences between brain tissues. In particular samples taken from cerebral hemispheres appear to have greater quantity of CH_2 groups and more rigid (less dynamic) water than tissues taken from cerebellum. This has been attributed to a greater amount of myelin present in our samples from cerebral hemispheres.
- Concerning the left-right asymmetry, this has been detected at a molecular level mainly in the rotational properties of slow water in the cerebral hemispheres, but not in the cerebellum. Detection of left-right asymmetry in the cerebral hemispheres could be functionally relevant, since the two hemispheres are known to have different functions: the left hemisphere has a leading role for highly demanding specific pro-

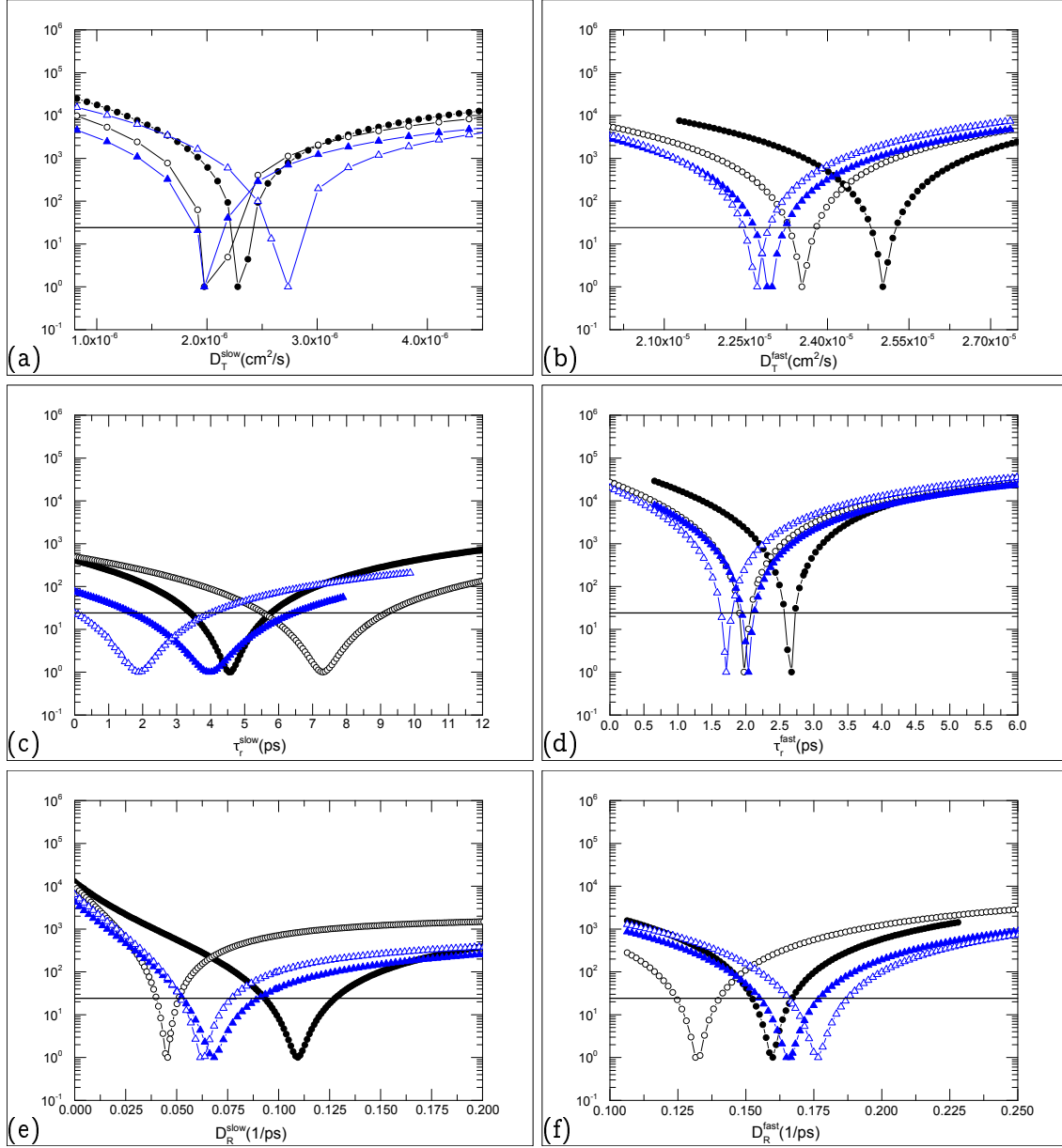


Figure 6.5: Confidence limits analysis: $\Delta\chi^2 = \chi_{p_i}^2 - \chi_{min}^2 + 1$ as a function of parameters; (a): D_T^{slow} , (b): τ_r^{slow} ; (c): D_R^{slow} ; (d): D_T^{fast} ; (e): τ_r^{fast} ; (f): D_R^{fast} . Black filled circle (—●—) are RCH; black opened circle (—○—) are LCH; blue filled triangle (—▲—) are RC; blue opened triangle (—△—) are LC. The horizontal black line cuts the plot at $\Delta\chi^2 = 24.2$ and determines the 99% confidence intervals.

cess, such as language and motor actions, which may require specialized networks, whereas the right hemisphere has a leading role for more general processes, such as integration tasks, which may require a more general level of interconnection.

Chapter 7

Conclusions

The aim of this PhD project was to give a contribution in clarifying water dynamics in complex systems, as cells and tissues, due to the controversial results reported in literature concerning such topic. In particular, there are two lines of thinking on water molecules in cells. The first one suggests that, due to macromolecular crowding, the cell interior is something like a gel-like system where diffusion of water molecules is substantially hampered. On the other hand, the second line of thinking proposes that water inside cells is substantially bulk water although with somewhat more structured properties. In contrast of these interpretations, a new recent approach suggest that two kinds of water components coexist in such complex systems. A majority percentage conserves bulk water properties, while the minority one is the one with reduced dynamics properties. The latter water component has restricted dynamics due to the interactions with macromolecules, lipid in membranes and others constituents. Furthermore, water dynamics is extensively studied as probe of brain tissues from humans, rats, bovines, monkeys, etc using different kinds of techniques based on Nuclear Magnetic Resonance. Also in this topic no consensus has been reached. In fact, the different techniques and the many models to describe the data lead a controversial results where in some works only one water component has been seen and in others two water components have been distinguished with a not clear physical interpretation. Therefore, the debate is still open.

In this landscape, we support the thesis that two water populations are present in cells and tissues and, moreover, this is a general property of systems where water is the solvent of macromolecules, cells and tissues. The techniques used to investigate such systems was mainly the Quasi Elastic Neutron Scattering which has access to atomic scale and looks at picosecond/nanosecond diffusive processes. In particular, such technique is particularly sensible to the incoherent scattering signal coming from hydrogens atoms during scattering experiment. Thus, we propose a theoretical model where four hydrogens motions can be distinguished: (1) “fixed hydrogens” coming from hydrogens motion not resolved by instrumental resolution, (2) “slow hydrogens” coming from hydrogens belonging to “slow

water” component, (3) “fast hydrogens” coming from hydrogens belonging to “fast water” component and (4) “very fast hydrogens” coming from hydrogens belonging to methylene groups (CH_2 groups) component, as discussed in Chapter 3. The “fast water” component is characterized by dynamics properties similar to bulk water, and the “slow water” one by slower dynamics. The strategy used to validate the theoretical model consisted in (1) to check the model first on phantom systems made of sucrose aqueous solutions, the easiest systems where water does not anymore freely diffuse and then on complex systems such as cells and brain tissues; (2) to perform QENS experiments using two data set from two energy resolutions with an observed time window of 10 and 70 ps to properly detect slow and fast water components, respectively; (3) to apply the confidence limit investigation on the global parameters related to the theoretical model in order to check their reliability. The experiments give us encouraging results that can be summarized as follows:

- the study of “phantom” systems highlights that in the presence of sucrose biomolecules two water populations are observed: a fast one with dynamics property very similar to those of pure water and a slow one with the restricted dynamics. The water populations show a dependence upon sucrose concentration allowing to understand that the slow water component is the water present in the hydration shell of the solute biomolecules and its dynamics is slowed down by a factor of three with respect to the fast one.
- The presence of these two water populations is a general properties of biological systems. The results on phantom systems, different kinds of cells in size and shape, and on bovine brain tissues fully validate the physical model approached.
- The temperature dependence of E. coli QENS spectra gives expected and meaningful results. In fact, an increment in dynamics in both slow and fast components of translational motions with a retardation factor between 10 and 15 is observed by increasing the temperature. On the other hand, rotational motions of fast component does not depend on the temperature. The retardation factor assumes values between 5 and 6.
- Glioma-9L cells exhibit a decrement of slow water component, 6.5% against 13.7% for E.coli and 17.7% for yeast, with a corresponding increment of the fast water contribution. A faster diffusion for translational and rotational water motions of slow water component was observed.
- The tissues samples investigated were right and left sides from cerebral hemispheres and cerebellum. From the QENS results it emerges that samples taken from cerebral hemispheres seem to have greater quantity of CH_2 groups and their water in general is less dynamic than that present in tissues taken from cerebellum. Moreover, the results show a left-right asymmetry coming from slow water component only in cerebral hemispheres, where left side seems have more restricted dynamics

than right one. Results may be interpreted in the view of hemisphere dependent cellular composition (number of neurons and cell distribution) as well as specificity of neurological functions.

The encouraging results reported in this thesis have prompted further experiments. Indeed, during my PhD project we have carried out QENS experiments also on tissues from other bovine brain regions as optic nerve, hypophysis and pineal and left and right cerebral hemisphere from healthy rat and right cerebral hemisphere from ill rat (tumor affected); analysis of the data obtained is still in progress. Particular importance will be given to the tumor affected sample to detect if any anomalous water diffusion could be connected with the disease.

Concerning cells systems, preliminary ENS experiment suggests to perform further investigations to better understand the change in slope highlighted in summed intensities at about 300 K for Glioma-9L (but not for the other investigated cells). Moreover, experiments on IN16B instrument, which works with energy resolution of 0.8 μeV (observed time window of ~ 800 ps), have already been performed and data analysis is in progress.

Appendix A

Mathematical and physical tools

A.1 Maxwell distribution

In the ideal gas done with N identical particles, the Hamiltonian is

$$H = \sum_{i=1}^N \frac{p_i^2}{2m}$$

under the ergodic hypothesis the partition function of N particles $Z(\vec{q}, \vec{p}, N)$ is noted if it is noted the partition function of one particle $Z(\vec{q}, \vec{p}, 1)$, where \vec{q} and \vec{p} are the coordinate and momentum respectively. The probability density to find any particle in the one-particle phase space is:

$$\rho(\vec{q}, \vec{p}) = \frac{V}{\lambda^3} \exp\left(-\frac{1}{2} \frac{mv^2}{k_B T}\right)$$

The velocity distribution for the ideal gas is expressed as

$$f(v) = \left(\frac{m}{2\pi k_B T}\right)^{3/2} \exp\left(-\frac{mv^2}{2k_B T}\right)$$

The probability to find a particle with coordinate between \vec{q} and $\vec{q}+d\vec{q}$ and with momentum \vec{p} and $\vec{p}+d\vec{p}$ is

$$\rho(\vec{q}, \vec{p}) d\vec{q}^3 d\vec{p}^3$$

in terms of velocity distribution may be written as

$$F(v) = f(v) dv^3 = \left(\frac{m}{2\pi k_B T}\right)^{3/2} \exp\left(-\frac{mv^2}{2k_B T}\right) 4\pi v^2 dv$$

$F(v)$ is the Maxwell distribution that assumes the maximum value in $\frac{dF}{dv}|_{v_{max}} = 0$

$$v_{max} = \sqrt{\frac{2k_B T}{m}}$$

the kinetic energy and the de Broglie wavelength associated to v_{max} is $E_k = k_B T$ and $\lambda = \frac{h}{\sqrt{2m_n k_B T}}$.

A.2 Density of state in the scattering event

The density of state for a neutron to be scattered with a k-vector between \vec{k}_f and $\vec{k}_f + d\vec{k}_f$ is the probability for a neutron to be scattered with a index n between \vec{n}_f and $\vec{n}_f + d\vec{n}_f$ that respect the bond condition of N particle in a box with side L and volume $V = L^3$. In the boundary condition $k = \frac{2\pi}{L}n$ in any direction.

$$\begin{aligned}
 d\vec{n}_f &= \frac{V}{(2\pi)^3} d\vec{k}_f \\
 &= \frac{V}{(2\pi)^3} k_f^2 dk_f \sin(\theta) d\theta d\psi \\
 &= \frac{V}{(2\pi)^3} k_f^2 dk_f d\Omega \\
 &= \frac{V}{(2\pi)^3} \frac{k_f}{2} (2k_f dk_f) d\Omega \\
 &= \frac{V}{(2\pi)^3} \frac{k_f}{2} \frac{2m_n}{\hbar^2} dE_f d\Omega \\
 &= \frac{V}{(2\pi)^3} \frac{m_n k_f}{\hbar^2} dE_f d\Omega.
 \end{aligned}$$

Finally,

$$\frac{\partial^2 n}{\Omega dE_f} = \frac{V}{(2\pi)^3} \frac{m_n k_f}{\hbar^2}.$$

A.3 Pair correlation function

$$\begin{aligned}
G_{\text{self correlation}}(\vec{r}, t) &= \frac{1}{(2\pi)^3} \int_{-\infty}^{\infty} d\vec{Q} e^{-i\vec{Q}\vec{r}} \sum_l \langle e^{-i\vec{Q}\cdot\vec{r}'_l(0)} e^{i\vec{Q}\cdot\vec{r}'_l(t)} \rangle \\
&= \frac{1}{(2\pi)^3} \int_{-\infty}^{\infty} d\vec{Q} e^{-i\vec{Q}\vec{r}} \sum_l \langle e^{-i\vec{Q}\cdot\vec{r}'_l(0)} \int d\vec{R} \delta(\vec{R} - \vec{r}'_l(t)) e^{i\vec{Q}\cdot\vec{R}} \rangle \\
&= \frac{1}{(2\pi)^3} \int_{-\infty}^{\infty} d\vec{Q} e^{-i\vec{Q}\vec{r}} \sum_l \int d\vec{R} \langle e^{-i\vec{Q}\cdot\vec{r}'_l(0)} \delta(\vec{R} - \vec{r}'_l(t)) e^{i\vec{Q}\cdot\vec{R}} \rangle \\
&= \frac{1}{(2\pi)^3} \int_{-\infty}^{\infty} d\vec{Q} e^{-i\vec{Q}\vec{r}} \sum_l \int d\vec{R} \langle e^{i\vec{Q}\cdot(\vec{R}-\vec{r}'_l(0))} \delta(\vec{R} - \vec{r}'_l(t)) \rangle \\
&= \sum_l \int d\vec{R} \langle \left(\frac{1}{(2\pi)^3} \int_{-\infty}^{\infty} d\vec{Q} e^{-i\vec{Q}\vec{r}} e^{i\vec{Q}\cdot(\vec{R}-\vec{r}'_l(0))} \right) \delta(\vec{R} - \vec{r}'_l(t)) \rangle \\
&= \sum_l \int d\vec{R} \langle \left(\frac{1}{(2\pi)^3} \int_{-\infty}^{\infty} d\vec{Q} e^{i\vec{Q}\vec{R}} e^{-i\vec{Q}\cdot(\vec{r}+\vec{r}'_l(0))} \right) \delta(\vec{R} - \vec{r}'_l(t)) \rangle \\
&= \sum_l \int d\vec{R} \langle \delta(\vec{R} - \vec{r} - \vec{r}'_l(0)) \delta(\vec{R} - \vec{r}'_l(t)) \rangle \\
&= \int d\vec{R} \sum_l \langle \delta(\vec{R} - \vec{r} - \vec{r}'_l(0)) \delta(\vec{R} - \vec{r}'_l(t)) \rangle \\
&= \int d\vec{R} \sum_l \langle \rho(\vec{R} - \vec{r}, 0) \rho(\vec{R}, t) \rangle
\end{aligned}$$

where from δ -Dirac definition

$$e^{i\vec{Q}\cdot\vec{r}'_l(t)} = \int d\vec{R} \delta(\vec{R} - \vec{r}'_l(t)) e^{i\vec{Q}\cdot\vec{R}}.$$

and Dirac- δ Fourier transform

$$\delta(\vec{R} - (\vec{r} + \vec{r}'_l(0))) = \frac{1}{(2\pi)^3} \int_{-\infty}^{\infty} d\vec{Q} e^{i\vec{Q}\vec{R}} e^{-i\vec{Q}\cdot(\vec{r}+\vec{r}'_l(0))}$$

A.4 Fourier Transform

Given the function $f(x)$ as

$$f(x) = \int_{-\infty}^{\infty} dk e^{ikx} g(k)$$

where x is the real space and k is the reciprocal space to fix the idea. $g(k)$ is the space-Fourier Transform of $f(x)$:

$$g(k) = \frac{1}{2\pi} \int_{-\infty}^{\infty} dx e^{-ikx} f(x)$$

The domain of $f(x)$ is the real space, we can pass in the reciprocal space operating the Fourier transform.

A.4.1 Summary of relation between $S(\vec{Q}, \omega)$, $I(\vec{Q}, t)$ and $G(\vec{r}, t)$

$S(\vec{Q}, \omega)$ is the Fourier transform of $I(\vec{Q}, t)$ in time:

$$S(\vec{Q}, \omega) = \frac{1}{2\pi\hbar} \int_{-\infty}^{\infty} dt e^{-i\omega t} I(\vec{Q}, t).$$

$S(\vec{Q}, \omega)$ is the Fourier transform of $G(\vec{r}, t)$ in time and real space:

$$S(\vec{Q}, \omega) = \frac{1}{(2\pi)^3 \hbar} \int_{-\infty}^{\infty} dt \int_{\text{all R-space}} d\vec{R} e^{i(\vec{Q} \cdot \vec{R} - \omega t)} G(\vec{r}, t).$$

$G(\vec{R}, t)$ is the Fourier transform of $I(\vec{Q}, t)$ in reciprocal space:

$$G(\vec{R}, t) = \frac{1}{(2\pi)^3} \int_{\text{all k-space}} d\vec{Q} e^{-i\vec{Q} \cdot \vec{R}} I(\vec{Q}, t).$$

$G(\vec{R}, t)$ is the inverse Fourier transform of $S(\vec{Q}, \omega)$ in energy and reciprocal space:

$$G(\vec{R}, t) = \int_{-\infty}^{\infty} \int_{\text{all k-space}} d\vec{Q} d(\hbar\omega) e^{-i(\vec{Q} \cdot \vec{R} - \omega t)} S(\vec{Q}, \omega).$$

$I(\vec{Q}, t)$ is the inverse Fourier transform of $S(\vec{Q}, \omega)$ in energy:

$$I(\vec{Q}, t) = \int_{-\infty}^{\infty} d(\hbar\omega) e^{i\omega t} S(\vec{Q}, \omega).$$

$I(\vec{Q}, t)$ is the inverse Fourier transform of $G(\vec{R}, t)$ in real space:

$$I(\vec{Q}, t) = \int_{\text{all R-space}} d\vec{R} e^{i\vec{Q} \cdot \vec{R}} G(\vec{R}, t).$$

A.5 Convolution theorem

Let the Fourier transform operator \mathcal{F} that return the Fourier transform of a given function, the Fourier transform function $\mathcal{F}(f)$ and $\mathcal{F}(g)$

$$\mathcal{F}(f \otimes g) = \mathcal{F}(f) \cdot \mathcal{F}(g)$$

A.6 Instrumental resolution in backscattering geometry

The definition of the instrumental resolution is given from the following equation:

$$\frac{\Delta E}{E}.$$

The kinetic energy is defined by:

$$\begin{aligned} E(k(\lambda)) &= \frac{\hbar^2 k^2}{2m_n} \\ &= \frac{h^2}{2m_n} \frac{1}{\lambda^2}. \end{aligned}$$

where $k = 2\pi/\lambda$ and $\hbar = 2\pi h$. From the Bragg's law:

$$\lambda = 2d \sin(\theta).$$

Therefore, the kinetic energy becomes

$$E(d, \theta) = \frac{h^2}{8m_n} \frac{1}{d^2 \sin^2(\theta)}.$$

The variation ΔE is defined as follows

$$\Delta E = \left| \frac{\partial E}{\partial d} \right| \Delta d + \left| \frac{\partial E}{\partial \theta} \right| \Delta \theta.$$

The differential partial of E respect with d variable is

$$\frac{\partial E}{\partial d} = -\frac{h^2}{4m_n} \frac{1}{\sin^2(\theta)} \frac{1}{d^3}.$$

The differential partial of E respect with θ variable is

$$\frac{\partial E}{\partial \theta} = -\frac{h^2}{4m_n} \frac{1}{d^2} \frac{\cot(\theta)}{\sin^2(\theta)}.$$

Therefore,

$$\begin{aligned} \frac{\Delta E}{E} &= \frac{\frac{h^2}{4m_n} \frac{1}{\sin^2(\theta)} \left[\frac{1}{d^3} \Delta d + \frac{1}{d^2} \cot(\theta) \Delta \theta \right]}{\frac{h^2}{8m_n} \frac{1}{d^2 \sin^2(\theta)}} \\ &= 2 \left[\frac{\Delta d}{d} + \cot(\theta) \Delta \theta \right]. \end{aligned}$$

Appendix B

Analysis method tools

B.1 Unit conversions

In Table B.1 are shown some useful conversion from the dimensional unit used in the STRfit tool to which one typically associated concerning translational/rotational diffusion coefficient and residence time.

Physical quantity	Unit used in the software	Conversion factor	Physical unit
D_T	[meV Å ²]	1.52E-4	[cm ² s ⁻¹]
D_R	[meV]	1.52	[ps ⁻¹]
τ_r	[meV ⁻¹]	0.658	[ps]

Table B.1: List of conversion from unit used in SRTfit to physical unit.

B.2 Mpfit versus Coolfit engine

In Figure B.1 shows confident limit investigation using mpfit and coolfit engine. Such two routines give similar trend, proving that they based on the same algorithm, but they use different paths. In particular, mpfit is more noisy than coolfit routine.

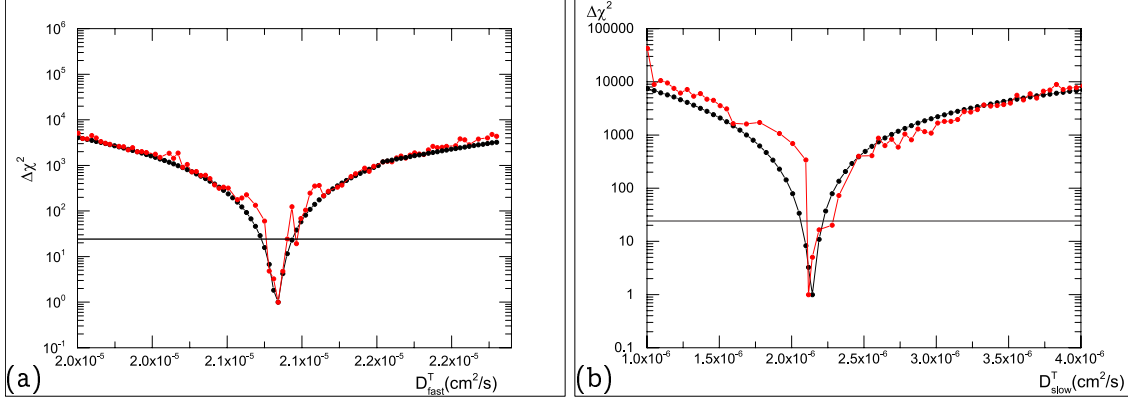


Figure B.1: Confidence limits analysis: $\Delta\chi^2 = \chi_{p_i}^2 - \chi_{min}^2 + 1$ as a function of parameter D_T^{fast} (panel (a)) and D_T^{slow} (panel (b)) for the data relative to *E. coli* cells. Red and black dots refer to results obtained with two different minimization routines developed at ILL. The horizontal black line cuts the plot at $\Delta\chi^2 = 24.2$ and determines the 99% confidence intervals.

For this reason the confidence limit investigation is made using coolfit routine in this thesis.

Appendix C

Elastic neutron scattering technique

C.0.1 Elastic Neutron Scattering model

Under Gaussian approximation [90], the atoms vibrate with small fluctuations around their equilibrium positions without preferential directions. Thus, the elastic incoherent scattering function, $S_{inc}(\vec{Q}, \omega = 0)$, may be written in the following way

$$S_{inc}(\vec{Q}, \omega = 0) \sim \frac{\sigma_{inc}}{N} \frac{1}{2\pi\hbar} \exp\left(-\frac{1}{6}\langle\vec{u}^2\rangle Q^2\right), \quad (\text{C.1})$$

where $\langle\vec{u}^2\rangle$ is the atomic Mean Square Displacement (MSD) and \vec{u} is defined as

$$\vec{u} = \vec{r}(t) - \vec{r}(0). \quad (\text{C.2})$$

From equation C.1 it is possible to extract the following expression of the MSDs:

$$\langle\vec{u}^2\rangle = -6 \frac{\partial \ln(S_{inc}(\vec{Q}, \omega = 0))}{\partial Q^2}. \quad (\text{C.3})$$

Due to the instrumental energy resolution, which assume a finite value, ω is not strictly equal to zero as in the ideal case. The energy resolution $\Delta E = \hbar\Delta\omega$ is related to the accessible time window Δt by Heisenberg's uncertainty principle.

C.0.2 Backscattering spectrometer: IN13

IN13 is an high resolution spectrometer in a backscattering configuration placed in the guide hall. The neutron beam of IN13, as shown in Figure 2.5 of Chapter 2, travels in the thermal guide line H24 which has a width of 3.5 cm and a height of 12.5 cm. The incoming neutrons flux, measured on the target position, is $\sim 2 \times 10^4 \text{ ns}^{-1} \text{ cm}^{-2}$. The thermal guide facing IN13 delivers neutrons with energy of 16.45 meV (corresponding to a wavelength of 2.23 Å). A monochromator, made of CaF_2 crystals at (422) orientation,

selects the incoming neutron energy varying the lattice d-spacing through temperature regulation (the monochromator is inserted in a cryofurnace). On the other hand, the final neutron energy is fixed and it is defined by the analysers crystals (CaF_2) kept at room temperature. The relation between the energy and the neutron wavelength is defined by

$$E = \frac{h^2}{2m_n\lambda_i^2}; \quad (\text{C.4})$$

where the wavelength λ_i is also related to the crystal by Bragg's law in first order:

$$\lambda_i = 2d \sin \theta_B. \quad (\text{C.5})$$

d is the interatomic lattice distance and θ_B is the scattering Bragg angle. The instrumental energy resolution is (Appendix A.6):

$$\frac{\Delta E}{E} = \frac{2\Delta d}{d} + 2 \cot \theta_B \Delta \theta_B, \quad (\text{C.6})$$

The best resolution is achieved in backscattering configuration, since $\theta_B = 90^\circ \Rightarrow \cot \theta_B = 0$, therefore instrumental energy resolution, $\Delta E/E = 2\Delta d/d$, depends only from the quality of the monochromator crystal. The characteristics of IN13 are [web5]:

- the neutron flux at the sample is $\sim 2 \times 10^4 \text{ ns}^{-1} \text{ cm}^{-2}$;
- the energy resolution is $8 \text{ } \mu\text{eV}$ ($\Delta t \sim 100 \text{ ps}$);
- the accessible energy-range is $[-125; 150] \mu\text{eV}$;
- the Q-resolution is $< 0.1 \text{ } \text{\AA}^{-1}$;
- the accessible Q-range is $[0.19; 4.9] \text{ } \text{\AA}^{-1}$;

As we can see in Figure C.1, to reproduce the backscattering condition the neutron beam is diffracted by monochromator CaF_2 crystals, primary spectrometer, with a small angle of 1.8° since the zero angle brings back the neutron beam into the guide. Thus, a *graphite deflector* re-orientates the neutron beam by $\sim 90^\circ$, in order to be focused onto the target. The deflector is composed of pyrolytic graphite crystals. The neutron beam before hitting the sample passes through the *chopper* (6756 rpm) and the *monitor*. The chopper avoids to count those neutrons coming from higher orders of reflection of the monochromator crystals CaF_2 and those neutrons scattered directly from the sample into the detectors, thus without being selected in energy by the analysers. The monitor counts the incoming neutrons flux. Finally, the neutron beam arrives to the target. The neutrons can:

- cross the sample without that the scattering event takes place. Such neutrons will be absorbed by the *beam stop*.

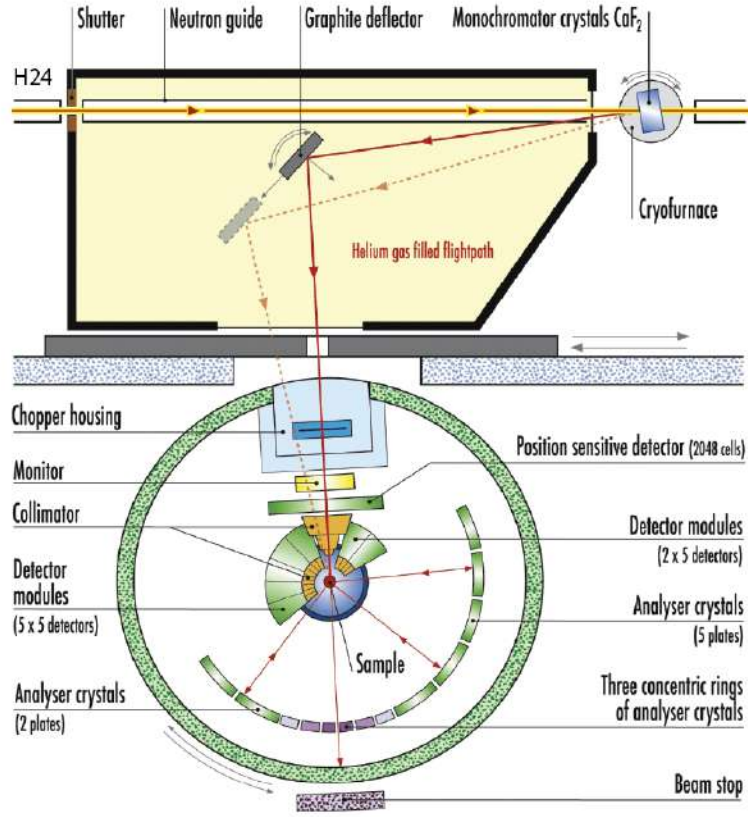


Figure C.1: Schematic layout of the instrument IN13.

- be scattered by the sample directly to the detectors. The chopper works to remove them.
- be scattered by the sample to the *analyser crystals*, that represent the secondary spectrometer operating under backscattering condition. The CaF₂ crystals, in direction (422), are displaced in a spherically curved surface. In such geometry, the final energy and the final k-vector are well defined. Finally, analysed neutrons go back, pass a second time through the sample, supposing that a second scattering event does not occur, to be finally collected and counted by the detectors.

The *detector modules* consist of seven independent units with five tubes each. The PSD are cylindric and they count scattered neutrons at small angle. The neutron detectors consist of tubes containing ³He gas. The neutrons can ionize the ³He gas in ²He, producing electrons. Thus an electric current is measured through an electric potential difference. A CCD camera is installed in the deflector box to control the sample alignment with respect to the neutron beam before the measurement.

C.0.3 ENS data correction

The macro written to correct ENS rawdata consists in the follows steps:

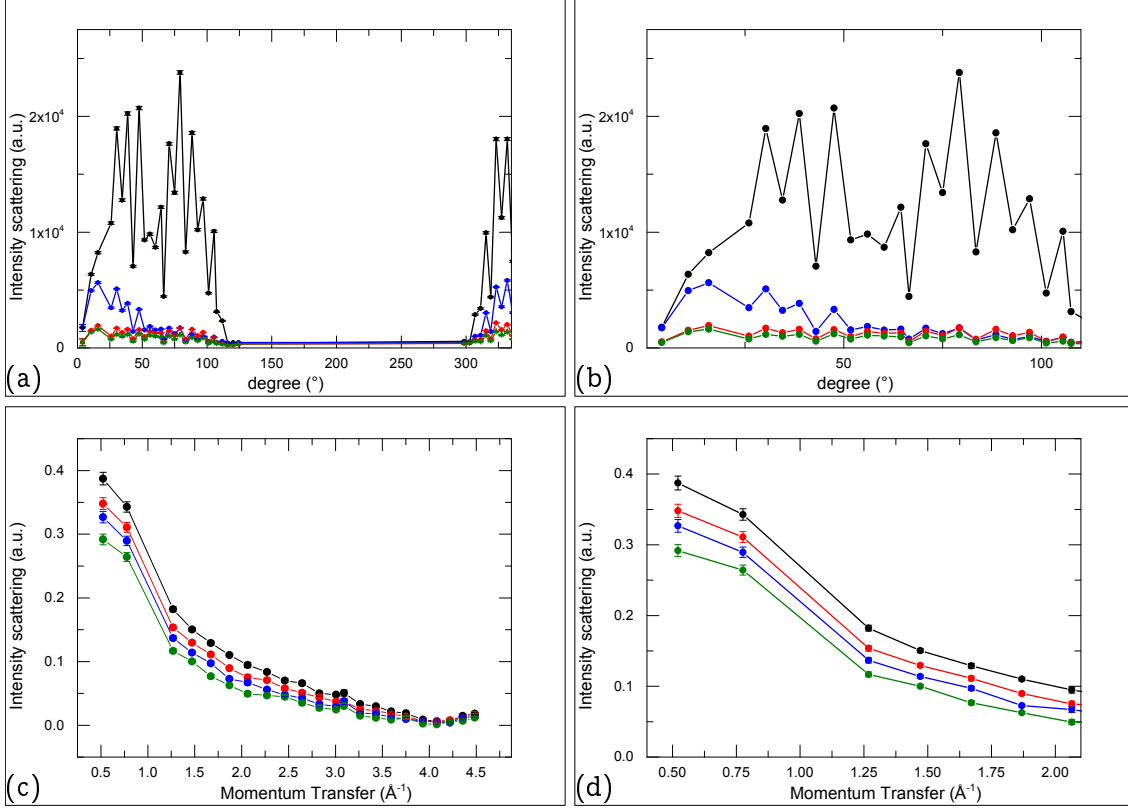


Figure C.2: Typical data from IN13 instrument with energy resolution of $8\mu\text{eV}$ for *E. coli*. Panel (a) shows a rawdata at 300 K as a function of the angle in degree. Black line points ($-\bullet-$) are vanadium, blue line points ($-\bullet-$) are the sample, red line points ($-\bullet-$) are empty cell and green line points ($-\bullet-$) are empty cell with aluminium foil. Panel (b) shows a zoom of panels (a). Panel (c) shows the elastic scattering intensity as a function of the momentum transfer at different temperatures. Panel (d) shows a zoom of panels (b). Black line points ($-\bullet-$), red line points ($-\bullet-$), blue line points ($-\bullet-$) and green line points ($-\bullet-$) are scattering intensity at 280, 290, 300 and 310 K, respectively.

- 1) to read the elastic signal for sample, vanadium empty cells, and empty cell with Aluminium foil normalized to the monitor 1, corrected to the absorption factor. The elastic signal of empty cell foil is removed from the vanadium elastic signal. The elastic empty cell with aluminium signal is removed from the elastic sample signal, which is after normalized to the corrected vanadium.

- 2) To group the elastic signal in a given temperature step, to transform the angle detector channels in the momentum transfer scale in order to obtain the elastic intensity as a function of the momentum transfer.

The angle detector channels are 38 for IN13 instrument. Figure C.2a shows typical elastic neutron scattering intensity as a function of the scattering angle for *E. coli* sample at 300 K. The sample, the vanadium, the empty cell and empty cell with aluminium foil are in blue, black red and olive green lines points, respectively. In Figure C.2b a zoom of Figure C.2a between 4 and 110° (scattering angle) is shown. While, Figure C.2c shows a typical elastic scattering intensity as a function of the momentum transfer in the wide range between 0.2 and 4.9 Å⁻¹ after data treatment for different temperatures. Elastic scattering signal for *E. coli* sample for 280, 290, 300 and 310 K are in black, blue, red and olive green lines points, respectively. The elastic scattering signal shows a slowing down with increasing of the temperature due to the increasing of the nuclei vibrations that do not appear as “fix”. Figure C.2d shows a zoom of Figure C.2c between 0.2 and 2 Å⁻¹. From data manipulation MSD can be extracted fitting them with theoretical model expressed in Equation C.1.

C.1 Elastic Neutron Scattering experiment on cellular systems

During the PhD project, Elastic Neutron Scattering experiment was carry out in the experiment number 8 – 04 – 740 on IN13 for *E. coli*, Glioma-9L and yeast in order to obtain complementary information. The experiment was performed between 280 and 315 K, around the physiological temperature. IN13 has an energy resolution of 8 µeV that means an explored time of 80 ps.

Due to the large amount of water present in the sample, its thickness had to be minimized for multiple scattering neglection purpose reducing drastically the elastic scattering signal arising from the H atoms (not belonging to water molecules). Unfortunately, statistic of elastic signal from the samples was not enough to properly extract Mean Square Displacements.

To overcome the statistic issues summed intensities in the Q -range between 0.1 and 2 Å⁻¹ were obtained as shown in Figure C.3. The sum of scattered intensities defined by

$$S_{inc}^{sum}(Q_{max}, \omega = 0) = \frac{\sigma_{inc}}{N} \frac{1}{2\pi\hbar} \sum_{Q=0}^{Q_{max}} \exp(-\frac{1}{6} \langle \vec{u}^2 \rangle Q^2). \quad (C.7)$$

The sum is done on finite ΔQ intervals. If we take the limit for $\Delta Q \rightarrow 0$, we obtain the

integral which is proportional to the inverse of the root of the MSD function:

$$\lim_{\Delta Q \rightarrow 0} \left[\frac{\sigma_{inc}}{N} \frac{1}{2\pi\hbar} \sum_{Q=0}^{Q_{max}} \exp\left(-\frac{1}{6} \langle \vec{u}^2 \rangle Q^2\right) \right] = \int_0^{Q_{max}} dQ \exp\left(-\frac{1}{6} \langle \vec{u}^2 \rangle Q^2\right) \propto \frac{1}{\sqrt{\langle \vec{u}^2 \rangle}}, \quad (\text{C.8})$$

therefore

$$S_{inc}^{sum}(Q_{max}, \omega = 0) \propto \frac{1}{\sqrt{\langle \vec{u}^2 \rangle}}. \quad (\text{C.9})$$

The advantage of this different way to present the data is that the behavior obtained is independent from the Gaussian approximation, i.e. it is a direct result.

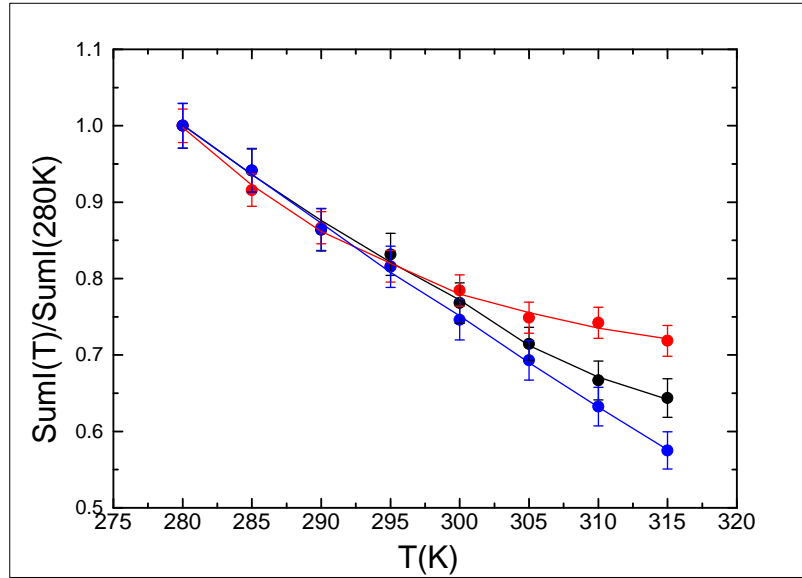


Figure C.3: Summed intensities normalized over summed intensities at 280 K. Black circle (—●—) are *E. coli*, red circle (—●—) are Glioma-9L and blue circle (—●—) are yeast.

Summed intensities for *E. coli* and yeast shows a linear trend with negative slope, as expected. In fact, it means that increasing the temperature the Mean Square Displacements increase, therefore the thermal vibrations increase with increasing of the temperature.

Concerning, Glioma-9L, although shows a decreasing with the temperature, exhibits a change in slope of the linear trend at about 300 K. In fact, though the normalization of summed intensities at 280 K is evident that for temperature lower than 300 K, summed intensities of Glioma-9L are overlapped to the ones of *E. coli* and yeast. While, this does

not occurs for temperature higher than 300 K. What it occurs is that summed intensities of Gliom-9L decreasing linearly, but with a rate smaller of a factor of 2.7. Further investigations are needed to better inquire the reasons of such preliminar experimental finding.

List of Figures

2.1	Left side: schematic representation of the scattering event between an incoming neutron beam with a target. Right side: Schematic illustration of a neutron scattering spectrum, containing elastic, inelastic, and quasielastic components [54].	9
2.2	Schematic representation of the differential solid angle.	11
2.3	Broadening of the quasi elastic peak for a system where Fick's law is satisfied (continuous line) and for a system with jump diffusion (dashed line) [63]. .	20
2.4	Typical neutron velocity distribution [65].	22
2.5	Scheme of the High Flux Reactor at ILL. The nuclear reactor produces hot neutrons (fuchsia guide lines), thermal neutrons (green guide lines) and cold neutrons (blue guide lines). The neutrons travel in these guide lines reaching each instruments.	22
2.6	Schematic layout of the instrument IN5 at ILL.	23
2.7	Schematic layout of the instrument TOFTOF at FRM II.	25
2.8	Schematic layout of the instrument TOFTOF at FRM II.	26
3.1	Flat sample holder pictures. Panel (a) shows top view picture of the sample holder. From left to right is shown the bottom and the top part of the sample holder. Panel (b) shows a picture in which the bottom part is reverse to show a typical geometry of such sample holder.	29
3.2	Large Array Manipulation Program (LAMP) screenshot. Software developed by computing group at ILL in order to manipulate big data from neutron scattering experiments.	30
3.3	Typical data from IN5 instrument at 10 μeV energy resolution. Panel (a) shows a rawdata at 90° as a function of the 1024 energy detector channels. Panel (b) shows a zoom of panel (a). Panel (c) shows the normalised scattering intensity as a function of the energy transfer at the corresponding Q value $\sim 0.91 \text{ \AA}^{-1}$. Panel (d) shows a zoom of panel (b). Black line points ($-\bullet-$) are vanadium, blue line points ($-\bullet-$) are the sample and red line points ($-\bullet-$) are empty cell	31

3.4	QENS spectrum of yeast cells taken at 0.36 \AA^{-1} at low energy resolution on IN5. Black points are the experimental data and the red line the total fit obtained using Equation 3.1. The various spectral contributions are represented by the lines in color. Fuchsia: elastic contribution arising from “fixed” hydrogens; green: roto-translation contribution arising from “fast” water population; blue: roto-translation component arising from “slow” water population; orange: CH_2 groups contribution; violet: background.	34
3.5	QENS spectra of yeast sample at low and high energy resolution from IN5 experiment in 3D view and contour plot. Panels (a) and (c) show 12 and 14 spectra as a function of energy transfer and momentum transfer at high and low energy resolutions, respectively. Panels (b) and (d) are the contour plots of panels (a) and (c).	35
3.6	STRfit screenshot. Tool of LAMP to implement multi fit using different listed o user theoretical models.	36
4.1	Panel (a) 2d view of sucrose representation. Panel (b) 3d view of sucrose representation.	39
4.2	QENS spectra of H_2O taken at $90 \mu\text{eV}$ energy resolution on IN6. Black points (\bullet) are the experimental data and the red lines ($-$) the fitting curves.	40
4.3	Panels (a) and (b): Summed intensities over all Q range of QENS spectra taken at 10 and $70 \mu\text{eV}$ energy resolutions, respectively. Black points ($- \bullet -$) are H_2O with 10% of sucrose, red point ($- \bullet -$) are H_2O with 20% of sucrose, blue points ($- \bullet -$) are H_2O with 30% of sucrose and fuchsia opened circle ($- \circ -$) is the vanadium. The percentage of sucrose is calculated over the total solution weigh.	42
4.4	Left panels: QENS spectra taken $10 \mu\text{eV}$ energy resolution; (a): H_2O with 10% of sucrose, (c): H_2O with 20% of sucrose and (e): H_2O with 30% of sucrose. Right panels: QENS spectra taken $70 \mu\text{eV}$ energy resolution; (b): H_2O with 10% of sucrose, (d): H_2O with 20% of sucrose and (f): H_2O with 30% of sucrose. Black points (\bullet) are the experimental data and the red lines ($-$) the fitting curves.	43
4.5	NMR [74] and our QENS measurements of the diffusion coefficients of water in sucrose solutions as a function of concentration. Black opened circle ($- \circ -$) are NMR measurements at 303 K and red opened circle ($- \circ -$) are our QENS measurements at 300 K.	44
4.6	Confidence limits analysis: $\Delta\chi^2 = \chi_{p_i}^2 - \chi_{min}^2 + 1$ as a function of parameters; (a): f fraction, (b): p_1 fraction; (c): p_2 fraction; (d): Γ_{CH_2} fraction. Blue opened square ($- \square -$) are H_2O with 10% of sucrose, blue opened circle ($- \circ -$) are H_2O with 20% of sucrose, blue opened triangle ($- \triangle -$) are H_2O with 30% of sucrose. The horizontal black line cuts the plot at $\Delta\chi^2 = 24.2$ and determines the 99% confidence intervals.	46

4.7	Confidence limits analysis: $\Delta\chi^2 = \chi_{p_i}^2 - \chi_{min}^2 + 1$ as a function of parameters; (a): D_T^{slow} , (b): τ_r^{slow} ; (c): D_R^{slow} ; (d): D_T^{fast} ; (e): τ_r^{fast} ; (f): D_R^{fast} . Blue opened square ($-\square-$) are $10SH_2O$, blue opened circle ($-\circ-$) are $20SH_2O$, blue opened triangle ($-\triangle-$) are $30SH_2O$ and blue filled diamond ($-\blacklozenge-$) are pure water. The horizontal black continuous/dashed line cuts the plot at 24.2 or at 12.3 to determine the 99% confidence intervals for sucrose solutions/pure water.	47
5.1	Sample image taken before the experiment with a fluorescence microscope. a) E. coli cells. b) Yeast <i>Schizosaccharomyces pombe</i> cells. c) Glioma-9L cells.	50
5.2	Panels (a) and (b): Summed intensities over all Q range of QENS spectra taken at 10 and 70 μeV energy resolutions, respectively. Panels (c) and (d) are a zoom view of panels (a) and (b), respectively. Black opened circle ($-\circ-$) are E. coli at 300 K, black opened triangle ($-\triangle-$) are E. coli at 310 K, black opened square ($-\square-$) are E. coli at 320 K and fuchsia opened circle ($-\circ-$) is the vanadium. The error bars in panels (c) and (d) are smaller than symbol size.	51
5.3	Panels (a) and (b): Summed intensities over all Q range of QENS spectra taken at 10 and 70 μeV energy resolutions, respectively. Panels (c) and (d) are a zoom view of panels (a) and (b), respectively. Black opened circle ($-\circ-$) are E. coli at 300 K, red opened circle ($-\circ-$) are Glioma-9L, blue opened circle ($-\circ-$) are Yeast at 300 K and fuchsia opened circle ($-\circ-$) is the vanadium. The error bars in panels (c) and (d) are smaller than symbol size.	52
5.4	Left panels: QENS spectra taken 10 μeV energy resolution; (a): E. coli at 300 K, (c): E. coli at 310 K and (e): E. coli at 320 K. Right panels: QENS spectra taken 70 μeV energy resolution; (b): E. coli at 300 K, (d): E. coli at 310 K and (f): E. coli at 320 K. Black points (\bullet) are the experimental data and the red lines ($-$) the fitting curves.	53
5.5	Left panels: QENS spectra taken 10 μeV energy resolution at 300 K; (a): Glioma-9L, (c): yeast. Right panels: QENS spectra taken 70 μeV energy resolution 300 K; (b): Glioma-9L, (d): yeast. Black points (\bullet) are the experimental data and the red lines ($-$) the fitting curves.	54
5.6	Confidence limits analysis: $\Delta\chi^2 = \chi_{p_i}^2 - \chi_{min}^2 + 1$ as a function of parameters; (a): f fraction, (b): p_1 fraction; (c): p_2 fraction; (d): Γ_{CH_2} fraction. Black opened circle ($-\circ-$) are E. coli at 300 K, black opened triangle ($-\triangle-$) are E. coli at 310 K, black opened square ($-\square-$) are E. coli at 320 K, red opened circle ($-\circ-$) are Glioma-9L and blue opened circle ($-\circ-$) are Yeast at 300 K. The horizontal black line cuts the plot at $\Delta\chi^2 = 24.2$ and determines the 99% confidence intervals.	56

5.7	Confidence limits analysis: $\Delta\chi^2 = \chi_{p_i}^2 - \chi_{min}^2 + 1$ as a function of parameters; (a): D_T^{slow} , (b): τ_r^{slow} , (c): D_R^{slow} , (d): D_T^{fast} , (e): τ_r^{fast} , (f): D_R^{fast} . Black opened circle ($-\circ-$) are E. coli at 300 K, black opened triangle ($-\triangle-$) are E. coli at 310 K, black opened square ($-\square-$) are E. coli at 320 K, red opened circle ($-\circ-$) are Glioma-9L and blue opened circle ($-\circ-$) are yeast at 300 K. The horizontal black line cuts the plot at $\Delta\chi^2 = 24.2$ giving a confidence of 99%.	57
6.1	Figure 6.1a shows section of bovine cerebrum (dorsal view). Figure 6.1b shows median section of the bovine brain [78].	61
6.2	Panel (a) shows a picture of cryotome Thermo Scientific Microm HM 560 Cryostat-Series at neuroscience department in Grenoble - France. Panel (b) shows a frontal view of such cryotome. Panel (c) shows the metal disc with the glued specimen allocated in vertical position in order to cut the specimen in slices. Panel (d) shows slices of brain tissues in the aluminium foil before to be closed within the sample holder.	63
6.3	Left panels: QENS spectra taken 10 μ eV energy resolution; (a): RCH, (c): LCH, (e): RC and (h): LC. Right panels: QENS spectra taken 70 μ eV energy resolution; (b): RCH, (d): LCH, (f): RC, (g): LC. Black points (\bullet) are the experimental data and the red lines ($-$) the fitting curves.	65
6.4	Confidence limits analysis: $\Delta\chi^2 = \chi_{p_i}^2 - \chi_{min}^2 + 1$ as a function of parameters; (a): f fraction, (b): p_1 fraction; (c): p_2 fraction; (d): Γ_{CH_2} fraction. Black fulfilled circle ($-\bullet-$) are RCH; black opened circle ($-\circ-$) are LCH; blue fulfilled triangle ($-\blacktriangle-$) are RC; blue opened triangle ($-\triangle-$) are LC. The horizontal black line cuts the plot at $\Delta\chi^2 = 24.2$ and determines the 99% confidence intervals.	69
6.5	Confidence limits analysis: $\Delta\chi^2 = \chi_{p_i}^2 - \chi_{min}^2 + 1$ as a function of parameters; (a): D_T^{slow} , (b): τ_r^{slow} , (c): D_R^{slow} , (d): D_T^{fast} , (e): τ_r^{fast} , (f): D_R^{fast} . Black fulfilled circle ($-\bullet-$) are RCH; black opened circle ($-\circ-$) are LCH; blue fulfilled triangle ($-\blacktriangle-$) are RC; blue opened triangle ($-\triangle-$) are LC. The horizontal black line cuts the plot at $\Delta\chi^2 = 24.2$ and determines the 99% confidence intervals.	70
B.1	Confidence limits analysis: $\Delta\chi^2 = \chi_{p_i}^2 - \chi_{min}^2 + 1$ as a function of parameter D_T^{fast} (panel (a)) and D_T^{slow} (panel (b)) for the data relative to E. coli cells. Red and black dots refer to results obtained with two different minimization routines developed at ILL. The horizontal black line cuts the plot at $\Delta\chi^2 = 24.2$ and determines the 99% confidence intervals.	81
C.1	Schematic layout of the instrument IN13.	84

C.2	Typical data from IN13 instrument with energy resolution of 8 μeV for <i>E. coli</i> . Panel (a) shows a rawdata at 300 K as a function of the angle in degree. Black line points (—●—) are vanadium, blue line points (—●—) are the sample, red line points (—●—) are empty cell and green line points (—●—) are empty cell with aluminium foil. Panel (b) shows a zoom of panels (a). Panel (c) shows the elastic scattering intensity as a function of the momentum transfer at different temperatures. Panel (d) shows a zoom of panels (b). Black line points (—●—), red line points (—●—), blue line points (—●—) and green line points (—●—) are scattering intensity at 280, 290, 300 and 310 K, respectively.	85
C.3	Summed intensities normalized over summed intensities at 280 K. Black circle (—●—) are <i>E. coli</i> , red circle (—●—) are Glioma-9L and blue circle (—●—) are yeast.	87

List of Tables

1.1	Translational and rotational parameters of bulk water in pure state, in cells pellet, in concentrated solutions collected in literature. D E. Coli is deuterated E. Coli cells, Red Blood Cells (RBC), IntraCellular Space (ICS), Haloarcula marismortui (Hmm) and Molecular Dynamics (MD) by simulations.	3
2.1	Incoherent and coherent cross section value of some elements. The cross section is given in units of barns, $1 \text{ b} = 10^{-24} \text{ cm}^2$	16
2.2	Main physical quantities of the three types of neutrons in the HFR of ILL.	21
3.1	Confidence level of $\Delta\chi^2$ with ν degree of freedom in the M-dimensional space.	37
4.1	Parameters values obtained from the global fits for pure water measured on IN6.	41
4.2	Parameters values obtained from the global fits for pure water measured IN6, H_2O with 10, 20 and 30% in weight of sucrose measured on IN5 at 300 K.	45
4.3	Percentage of fraction of “fast” and “slow” water populations together with translational and rotational retardation factors for $10SH_2O$, $20SH_2O$ and $30SH_2O$	45
5.1	Parameters values obtained from the global fits for E. coli at 300, 310 and 320 K, Glioma-9L and yeast at 300 K.	54
5.2	Fractions of “fast” and “slow” water populations together with translational and rotational retardation factors for various biological samples. RBC: Red Blood Cells; Hmm: Haloarcula marismortui.	55
6.1	Parameters values obtained from the global fits for RCH and RC.	66
6.2	Parameters values obtained from the global fits for RCH, LCH.	67
6.3	Parameters values obtained from the global fits for RC and LC.	68
6.4	Percentage of “fast” and “slow” water populations together with translational and rotational retardation factors for RCH, LCH, RC and LC.	68

B.1 List of conversion from unit used in SRTfit to physical unit.	80
---	----

Bibliography

- [1] J Jacobi et al. *Selected writings*, volume 28. Princeton University Press, 1951.
- [2] J S Clegg. Metabolism and the intracellular environment: the vicinal-water network model. *Cell-associated water*, pages 363–413, 1979.
- [3] A Fick. Ueber diffusion. *Ann. Phys. (Berl.)*, 170(1):59–86, 1855.
- [4] R J Ellis and A P Minton. Cell biology: join the crowd. *Nature*, 425(6953):27–28, 2003.
- [5] P Ball. Water as an active constituent in cell biology. *Chem. Rev.*, 108(1):74–108, 2008.
- [6] P Ball. Water as a biomolecule. *Chem. Phys. Phys. Chem.*, 9(18):2677–2685, 2008.
- [7] T Tsukahara, A Hibara, Y Ikeda, and T Kitamori. Nmr study of water molecules confined in extended nanospaces. *Angew. Chem. Int. Ed. Eng.*, 46(7):1180–1183, 2007.
- [8] G Pollack. *Cells, gels and the engines of life*. Ebner and Sons Publishers, 2001.
- [9] P Mentré. Water in the orchestration of the cell machinery. some misunderstandings: a short review. *J. Biol. Phys.*, 38(1):13–26, 2012.
- [10] V A Shepherd. The cytomatrix as a cooperative system of macromolecular and water networks. *Curr. Top. Dev. Biol.*, 75:171–223, 2006.
- [11] M Chaplin. Do we underestimate the importance of water in cell biology? *Nat. Rev. Mol. Cell. Biol.*, 7(11):861–866, 2006.
- [12] J C Dore and J Teixeira. *Hydrogen-bonded liquids*, volume 329. Springer Science & Business Media, 2012.
- [13] AH Narten and HA Levy. Water: A comprehensive treatise vol 1, ed f franks, 1972.

- [14] E Persson and B Halle. Cell water dynamics on multiple time scales. *Proc. Natl. Acad. Sci. U.S.A.*, 105(17):6266–6271, 2008.
- [15] M Tehei, B Franzetti, K Wood, F Gabel, E Fabiani, M Jasnin, M Zamponi, D Oesterhelt, G Zaccai, M Ginzburg, et al. Neutron scattering reveals extremely slow cell water in a dead sea organism. *Proc. Natl. Acad. Sci. U.S.A.*, 104(3):766–771, 2007.
- [16] M Jasnin, M Moulin, M Haertlein, G Zaccai, and M Tehei. Down to atomic-scale intracellular water dynamics. *EMBO reports*, 9(6):543–547, 2008.
- [17] J Teixeira, M-C Bellissent-Funel, S-H Chen, and A-J Dianoux. Experimental determination of the nature of diffusive motions of water molecules at low temperatures. *Phys. Rev. A*, 31(3):1913, 1985.
- [18] S Hsin Chen, M-C Bellissent-Funel, and J-M Zanotti. Slow dynamics of water molecules on the surface of a globular protein. *Faraday Discuss.*, 103:281–294, 1996.
- [19] J H Wang. Self-diffusion coefficients of water. *J. Phys. Chem.*, 69(12):4412–4412, 1965.
- [20] J H Wang. Theory of the self-diffusion of water in protein solutions. a new method for studying the hydration and shape of protein molecules. *JACS*, 76(19):4755–4763, 1954.
- [21] A Frölich, F Gabel, M Jasnin, U Lehnert, D Oesterhelt, AM Stadler, M Tehei, M Weik, K Wood, and G Zaccai. From shell to cell: neutron scattering studies of biological water dynamics and coupling to activity. *Faraday discuss.*, 141:117–130, 2009.
- [22] G Sposito. Single-particle motions in liquid water. ii. the hydrodynamic model. *J. Chem. Phys.*, 74(12):6943–6949, 1981.
- [23] A M Stadler, J P Embs, I Digel, G M Artmann, T Unruh, G Buřıldt, and G Zaccai. Cytoplasmic water and hydration layer dynamics in human red blood cells. *JACS*, 130(50):16852–16853, 2008.
- [24] S-H Chen, J Teixeira, and R Nicklow. Incoherent quasielastic neutron scattering from water in supercooled regime. *Phys. Rev. A*, 26(6):3477, 1982.
- [25] R Mills. Self-diffusion in normal and heavy water in the range 1-45. deg. *J. Phys. Chem.*, 77(5):685–688, 1973.
- [26] M-C Bellissent-Funel, S-H Chen, and J-M Zanotti. Single-particle dynamics of water molecules in confined space. *Phys. Rev. E*, 51(5):4558, 1995.
- [27] J Teixeira and A Luzar. In hydration processes in biology. *NATO Asi Series: A*, page 35, 1999.

- [28] A B Farimani, Y Wu, and N R Aluru. Rotational motion of a single water molecule in a buckyball. *Phys. Chem. Chem. Phys.*, 15(41):17993–18000, 2013.
- [29] K Takemura and A Kitao. Water model tuning for improved reproduction of rotational diffusion and nmr spectral density. *J. Phys. Chem. B*, 116(22):6279–6287, 2012.
- [30] D A Yablonskiy and A L Sukstanskii. Theoretical models of the diffusion weighted mr signal. *NMR Biomed.*, 23(7):661–681, 2010.
- [31] S E Maier and R V Mulkern. Biexponential analysis of diffusion-related signal decay in normal human cortical and deep gray matter. *MRI*, 26(7):897–904, 2008.
- [32] L Minati, D Aquino, S Rampoldi, S Papa, M Grisoli, M G Bruzzone, and E Maccagnano. Biexponential and diffusional kurtosis imaging, and generalised diffusion-tensor imaging (gdti) with rank-4 tensors: a study in a group of healthy subjects. *MAGMA*, 20(5):241–253, 2007.
- [33] C A Clark and D Le Bihan. Water diffusion compartmentation and anisotropy at high b values in the human brain. *Magn. Reson. Med.*, 44(6):852–859, 2000.
- [34] M M Cheung, E S Hui, K C Chan, J A Helpert, L Qi, and E X Wu. Does diffusion kurtosis imaging lead to better neural tissue characterization? a rodent brain maturation study. *Neuroimage*, 45(2):386–392, 2009.
- [35] J H Jensen and J A Helpert. Mri quantification of non-gaussian water diffusion by kurtosis analysis. *NMR in Biomedicine*, 23(7):698–710, 2010.
- [36] E X Wu and M M Cheung. Mr diffusion kurtosis imaging for neural tissue characterization. *NMR Biomed.*, 23(7):836–848, 2010.
- [37] J H Jensen, J A Helpert, A Ramani, H Lu, and K Kaczynski. Diffusional kurtosis imaging: The quantification of non-gaussian water diffusion by means of magnetic resonance imaging. *Magn. Reson. Med.*, 53(6):1432–1440, 2005.
- [38] A J Fabiano, M A Horsfield, and R Bakshi. Interhemispheric asymmetry of brain diffusivity in normal individuals: a diffusion-weighted mr imaging study. *Am. J. Neuroradio*, 26(5):1089–1094, 2005.
- [39] E Syková and C Nicholson. Diffusion in brain extracellular space. *Physiol. Rev.*, 88(4):1277–1340, 2008.
- [40] N Ohno, N Terada, S Saitoh, and S Ohno. Extracellular space in mouse cerebellar cortex revealed by in vivo cryotechnique. *J. Comp. Neurol.*, 505(3):292–301, 2007.

- [41] V A Levin, J D Fenstermacher, and C S Patlak. Sucrose and inulin space measurements of cerebral cortex in four mammalian species. *AJP-Legacy Content*, 219(5):1528–1533, 1970.
- [42] J V Sehy, J J H Ackerman, and J J Neil. Evidence that both fast and slow water adc components arise from intracellular space. *Magn. Reson. Med.*, 48(5):765–770, 2002.
- [43] I Ronen, S Moeller, K Ugurbil, and D-S Kim. Investigation of multicomponent diffusion in cat brain using a combined mtc-dwi approach. *MRI*, 24(4):425–431, 2006.
- [44] R V Mulkern, S Vajapeyam, S J Haker, and S E Maier. Magnetization transfer studies of the fast and slow tissue water diffusion components in the human brain. *NMR Biomed.*, 18(3):186–194, 2005.
- [45] N Pyatigorskaya, D Bihan, O Reynaud, and L Ciobanu. Relationship between the diffusion time and the diffusion mri signal observed at 17.2 tesla in the healthy rat brain cortex. *Magn. Reson. Med.*, 72(2):492–500, 2014.
- [46] F Natali, Y Gerelli, C Stelletta, and J Peters. Anomalous proton dynamics of water molecules in neural tissue as seen by quasi-elastic neutron scattering. impact on medical imaging techniques. In *AIP Conference Proceedings*, volume 1518(1), pages 551–557. AIP, 2013.
- [47] F Natali, C Dolce, J Peters, Y Gerelli, C Stelletta, and G Leduc. Water dynamics in neural tissue. *J. Phys. Soc. Jpn.*, 82(Suppl. A):SA017, 2013.
- [48] Y Gerelli, V G Sakai, J Ollivier, and A Deriu. Conformational and segmental dynamics in lipid-based vesicles. *Soft Matter*, 7(8):3929–3935, 2011.
- [49] N Martinez, F Natali, and J Peters. mqfit, a new program for analyzing quasi-elastic neutron scattering data. In *EPJ Web of Conferences*, volume 83, page 03010. EDP Sciences, 2015.
- [50] Irina Piazza, Antonio Cupane, Emmanuel L Barbier, Claire Rome, Nora Collomb, Jacques Ollivier, Miguel A Gonzalez, and Francesca Natali. Dynamical properties of water in living cells. *Front. Phys.*, 13(1):138301, 2018.
- [51] J Chadwick. The existence of a neutron. In *Proc. R. Soc., Lond., Ser. A*, volume 136(830), pages 692–708. The Royal Society, 1932.
- [52] J Chadwick. Possible existence of a neutron. *Nature*, 129(3252):312, 1932.
- [53] F Reif. *Fundamentals of Statistical and Thermal Physics*. Waveland, Springel V., 2005.

- [54] M Karlsson. Proton dynamics in oxides: insight into the mechanics of proton conduction from quasielastic neutron scattering. *Phys. Chem. Chem. Phys.*, 17(1):26–38, 2015.
- [55] J Dupuy. *Microscopic structure and dynamics of liquids*, volume 33. Springer Science & Business Media, 2012.
- [56] E Fermi. Sul moto dei neutroni nelle sostanze idrogenate. *Ricerca scientifica*, 7(2):13–52, 1936.
- [57] H Schober. An introduction to the theory of nuclear neutron scattering in condensed matter. *J. Neutr. Res.*, 17(3-4):109–357, 2014.
- [58] L Van Hove. Correlations in space and time and born approximation scattering in systems of interacting particles. *Phys. Rev.*, 95(1):249, 1954.
- [59] C Cohen-Tannoudji, B Diu, and F Laloe. *Quantum mechanics*, volume 2. Wiley, 1992.
- [60] M Bee. *Quasielastic neutron scattering: principles and applications in solid state chemistry*. Biology and Materials Science, Adam Hilger, Bristol, 1988.
- [61] R Taylor and R Krishna. *Multicomponent mass transfer*, volume 2. John Wiley & Sons, 1993.
- [62] Kundan S Singwi and A. Sjölander. Resonance absorption of nuclear gamma rays and the dynamics of atomic motions. *Phys. Rev.*, 120:1093–1102, Nov 1960.
- [63] J I M Damian, J R Granada, F Cantargi, and D Roubtsov. New evaluation of thermal neutron scattering libraries for light and heavy water. In *EPJ Web of Conferences*, volume 146, page 13001. EDP Sciences, 2017.
- [64] V F Sears. Theory of cold neutron scattering by homonuclear diatomic liquids: Ii. hindered rotation. *Can. J. Phys.*, 44(6):1299–1311, 1966.
- [65] I Altarev, M Daum, A Frei, E Gutmiedl, G Hampel, FJ Hartmann, W Heil, A Knecht, JV Kratz, T Lauer, et al. Neutron velocity distribution from a superthermal solid 2 h 2 ultracold neutron source. *EPJ A*, 37(1):9–14, 2008.
- [66] D Richard, M Ferrand, and GJ Kearley. Lamp, the large array manipulation program. *J. Neutr. Res.*, 4:33–39, 1996.
- [67] D Richard, M Ferrand, and GJ Kearley. Large array manipulation program (lamp). *ILL*, 2006.

- [68] D P Tieleman, S-J Marrink, and H JC Berendsen. A computer perspective of membranes: molecular dynamics studies of lipid bilayer systems. *Biochim. Biophys. Acta*, 1331(3):235–270, 1997.
- [69] R W Pastor, R M Venable, and S E Feller. Lipid bilayers, nmr relaxation, and computer simulations. *Acc. Chem. Res.*, 35(6):438–446, 2002.
- [70] M C Pitman, F Suits, K Gawrisch, and S E Feller. Molecular dynamics investigation of dynamical properties of phosphatidylethanolamine lipid bilayers. *J. chem. phys.*, 122(24):244715, 2005.
- [71] D W Marquardt. An algorithm for least-squares estimation of nonlinear parameters. *J. Soc. Ind. Appl. Math.*, 11(2):431–441, 1963.
- [72] P R Bevington, D K Robinson, J M Blair, A J Mallinckrodt, S McKay, et al. Data reduction and error analysis for the physical sciences. *Comp. Phys.*, 7(4):415–416, 1993.
- [73] W H Press. *Numerical recipes 3rd edition: The art of scientific computing*. Cambridge university press, 2007.
- [74] N Ekdawi-Sever, J J de Pablo, E Feick, and E von Meerwall. Diffusion of sucrose and α , α -trehalose in aqueous solutions. *J. Phys. Chem. A*, 107(6):936–943, 2003.
- [75] S Engelsen and S Pérez. The hydration of sucrose. *Carbohydr. Res.*, 292:21–38, 1996.
- [76] S Moreno, A Klar, and P Nurse. [56] molecular genetic analysis of fission yeast *schizosaccharomyces pombe*. *Methods Enzymol.*, 194:795–823, 1991.
- [77] M Castillo, J K Smith, L Kwock, and K Wilber. Apparent diffusion coefficients in the evaluation of high-grade cerebral gliomas. *Am. J. neuroradio.*, 22(1):60–64, 2001.
- [78] B Klaus-Dieter, H Robert E., W Anita, B Silke, J Gisela, R Renate, and S Diemut. *Bovine Anatomy - An Illustrated Text*. Schlütersche, 2003.
- [79] J C Eccles. *The cerebellum as a neuronal machine*. Springer Science & Business Media, 2013.
- [80] A W Toga and P M Thompson. Mapping brain asymmetry. *Nat. Rev. Neurosci.*, 4(1):37–48, 2003.
- [81] G Partadiredja, R Miller, and D E Oorschot. The number, size, and type of axons in rat subcortical white matter on left and right sides: a stereological, ultrastructural study. *J. Neurocytol.*, 32(9):1165–1179, 2003.

- [82] D W Zaidel, M M Esiri, and P J Harrison. Size, shape, and orientation of neurons in the left and right hippocampus: investigation of normal asymmetries and alterations in schizophrenia. *Am. J. Psychiatry*, 154(6):812, 1997.
- [83] K E Watkins, T Paus, J P Lerch, A Zijdenbos, DL Collins, P Neelin, J Taylor, K J Worsley, and A C Evans. Structural asymmetries in the human brain: a voxel-based statistical analysis of 142 mri scans. *Cereb. cortex*, 11(9):868–877, 2001.
- [84] A K H Miller, R L Alston, and J A N Corsellis. Variation with age in the volumes of grey and white matter in the cerebral hemispheres of man: measurements with an image analyser. *Neuropathol. Appl. Neurobiol.*, 6(2):119–132, 1980.
- [85] S M Blinkov and I Glezer. *The human brain in figures and tables: a quantitative handbook*. Basic Books, 1968.
- [86] G Brante. *Studies on lipids in the nervous system: with special reference to quantitative chemical determination and topical distribution*. Blackwell Scientific Publ., 1949.
- [87] Y Iturria-Medina, A Pérez Fernández, D M Morris, E J Canales-Rodríguez, H A Haroon, L García Pentón, M Augath, L Galán García, N Logothetis, G JM Parker, et al. Brain hemispheric structural efficiency and interconnectivity rightward asymmetry in human and nonhuman primates. *Cereb. cortex*, 21(1):56–67, 2010.
- [88] T Niendorf, R M Dijkhuizen, D G Norris, M van Lookeren Campagne, and K Nicolay. Biexponential diffusion attenuation in various states of brain tissue: Implications for diffusion-weighted imaging. *Magn. Reson. Med.*, 36(6):847–857, 1996.
- [89] B A Inglis, E L Bossart, D L Buckley, E D Wirth, and T H Mareci. Visualization of neural tissue water compartments using biexponential diffusion tensor mri. *Magn. Reson. Med.*, 45(4):580–587, 2001.
- [90] AZMS Rahman, KS Singwi, and A Sjölander. Theory of slow neutron scattering by liquids. i. *Phys. Rev.*, 126(3):986, 1962.

Web page consulted

- [web1] ILL IN5 instrument official web site. <http://www.ill.eu/instruments-support/instruments-groups/instruments/in5/characteristics/>.
- [web2] FRMII official web site. <http://www.mlz-garching.de/toftof>.
- [web3] IN6-SHARP official web site. <https://www.ill.eu/instruments-support/instruments-groups/instruments/in6-sharp/characteristics/>.
- [web4] MPFIT official web site. <https://www.physics.wisc.edu/~craigm/idl/fitting.html>.
- [web5] ILL IN13 instrument official web site. <http://www.ill.eu/en/instruments-support/instruments-groups/instruments/in13/characteristics/>.



UNIVERSITÀ DEGLI STUDI DI PALERMO

CICLO XXX

ANNO CONSEGUIMENTO TITOLO 2018

